12-2014

Photosystem I-Based Applications for the Photo-catalyzed Production of Hydrogen and Electricity

Rosemary Khuu Le
University of Tennessee - Knoxville, rle1@vols.utk.edu

To the Graduate Council:

I am submitting herewith a dissertation written by Rosemary Khuu Le entitled "Photosystem I-Based Applications for the Photo-catalyzed Production of Hydrogen and Electricity." I have examined the final electronic copy of this dissertation for form and content and recommend that it be accepted in partial fulfillment of the requirements for the degree of Doctor of Philosophy, with a major in Chemical Engineering.

Paul D. Frymier, Major Professor

We have read this dissertation and recommend its acceptance:

Eric T. Boder, Barry D. Bruce, Hugh M. O'Neill

Accepted for the Council:

Carolyn R. Hodges

Vice Provost and Dean of the Graduate School

(Original signatures are on file with official student records.)

Photosystem I-Based Applications for the Photo-catalyzed Production of Hydrogen and Electricity

A Dissertation Presented for the

Doctor of Philosophy

Degree

The University of Tennessee, Knoxville

Rosemary Khuu Le

December 2014

DEDICATION

This dissertation is dedicated to: my parents and brothers for their love, support, and fostering an environment for passion for science and discovery, my teachers and mentors who inspired and encouraged me to pursue science, and to the smart and strong women in my life – "Who run the world? Girls!"

ACKNOWLEDGEMENTS

I am deeply grateful for the support and encouragement from many people during my time at Tennessee. First, I would like to thank my advisor, Dr. Paul Frymier for his time, enthusiasm, constructive criticism, patience, trusting me to work independently, and philosophical conversations. I would also like to thank my committee members, Dr. Eric Boder, Dr. Barry Bruce, and Dr. Hugh O'Neill for their time, guidance, insightful ideas, and involvement in collaborative projects.

I appreciate the assistance provided by Ifeyinwa Iwuchukwu, Prakitchai Chotewotmuntri, Richard Simmerman, and Khoa Nguyen in getting me acquainted with photosystem I. I also thank Maryam Raeeszadeh-Sarmazdeh for her guidance with sortase. I am also indebted to all of the undergrads (Carrie Lloyd, Donglee Shin, Stephanie Bailey, Anissa Goetz) who gave me their time and provided me with an extra set of hands with molecular cloning and protein purification.

To Jane Breder, thank you for coordinating everything STAIR-related. To my labmates, Sustainabilabuddies, Supergroup family, and classmates, thank you for your friendship, commiseration, and teaching me new things. To my 'Loe Down crew and Schmoopie, thank you for keeping me grounded, reminding me to be mindful, and for the love and support.

I am forever grateful to my parents for instilling a strong work ethic in me and believing in me, which helped me stay persistent throughout my time at Tennessee, especially when research did not go as planned, and giving me all of the opportunities to be creative and learn.

Finally, I gratefully acknowledge the financial support provided by the National Science Foundation's IGERT STAIR program (DGE-0801470) and support from the University of Tennessee Sustainable Energy Education and Research Center (SEERC) that made this work possible.

ABSTRACT

The aim of this dissertation was to optimize systems integrating the photosystem I (PSI) redox protein, which is involved in photosynthesis, with noble metals for electron transfer to show its versatility: 1) in solution coupled with platinum to mediate hydrogen evolution and 2) on a planar gold surface for electricity production.

Response surface methodology was utilized to study variables that affect hydrogen (H_2) yield from platinized-PSI. Light intensity, temperature, and platinum concentration were varied during the platinum-photo-reduction process. Analysis of the effects of the variables on H_2 yield allowed for determination of a condition for optimized hydrogen production: 240 μE/m^2/s [micro-Einsteins per square meter per second] light intensity, 638 μM [micro-molar] platinum, and 31°C [degrees Celsius] temperature. A model was developed from an experimental solution space and predicted an optimum H_2 yield of ~8.17 μmol H_2/mg chl *a*/h [micro-mole hydrogen per milligram chlorophyll *a* per hour]. The model was validated by an 8.02 μmol H_2/mg chl *a*/h value determined experimentally and platinum concentration had the greatest influence on H_2 yield.

Small-angle neutron scattering was used to investigate the solution structure of trimeric PSI from *Thermosynechococcus elongatus* in n-dodecyl-beta-D-maltoside (DDM) detergent to determine the orientation of the detergent molecules around PSI. The resulting PSI-DDM reconstruction structure showed the detergent oriented around the hydrophobic and interstitial periphery of the trimer in a non-uniform manner and did not agglomerate on the stromal or lumenal surfaces. Therefore, linkages to these faces are unlikely to be hindered by the presence of detergent.

Photo-activity has been observed from techniques attaching PSI to conductive surfaces. These techniques allow for dense deposition of the protein, but fail to control the orientation of PSI on the surface. The highly selective sortase-mediated ligation (SML) reaction was used to covalently attach PSI on tri-glycine functionalized gold surfaces. The exposed C-termini of PSI subunits from *Synechocystis* sp. PCC 6803 were targeted to study SML to control the orientation of PSI on gold for enhanced electron transfer, which yielded a 50% increase in current production from less than 100 nA/cm^2 [nanoampere per square centimeter] to approximately 150 nA/cm^2 compared to other monolayers.

TABLE OF CONTENTS

LIST OF TABLES

LIST OF FIGURES

1. INTRODUCTION

Photosynthesis has allowed for plants, algae, cyanobacteria, and other photosynthetic bacteria to flourish on solar energy via carbon fixation. This process is carried out by an elegant series of proteins that work in tandem to coordinate light absorption, charge separation, and electron transport. Here we are interested in utilizing one such protein, photosystem I (PSI) for integration into technologies to mediate hydrogen evolution *in vitro* when coupled with a noble metal (platinum) and photo-electrochemical applications for electricity production on gold to better understand and optimize systems that utilize PSI for electron transfer. This chapter presents a global overview for the rationale for pursuing technologies that employ solar energy, the functionality of PSI, and discusses the research efforts that inspired the work presented in this dissertation and techniques that were employed to study PSI in solution and on surfaces.

1.1 Global Energy Crisis

According to the International Energy Outlook 2013 (IEO2013), it is projected that the world's energy consumption will increase by 56% between 2010 and 2014. The rise in world energy use is expected to rise from 524 quadrillion British thermal units (BTU) in 2010 to 630 quadrillion BTU in 2020 and 820 quadrillion BTU in 2040. Though renewable energy and nuclear power are becoming the world's fastest-growing energy sources, each increasing by 2.5% every year, we are still highly dependent on fossil fuels. Fossil fuels continue to account for 80% of world energy use and will maintain at this level through 2040. Natural gas is steadily becoming the fastest-growing fossil fuel for future use, where global natural gas consumption is expected to increase by 1.7% every year, with discoveries of supplies of shale gas and methane. Furthermore, coal use continues to grow faster than petroleum and other liquid fuel use through 2030 [1].

We have become heavily dependent on cheap fossil fuels, but these sources of energy took millions of years to form and are not renewable within a human life span. In essence, all the energy found in fossil fuels (oil, gas, coal) originally came from the sun, captured through photosynthesis. One major issue with being dependent on these fossil fuels is that we are withdrawing from this natural energy bank without making any significant deposits. With the current rate of consumption, there may not be deposits available for future generations. Another implication of our consumption is the release of large quantities of carbon dioxide, a greenhouse gas associated with climate change. With the lack of strict policies and regulation on limiting fossil fuel use, worldwide energy-related carbon dioxide emissions are expected to rise from 31 billion metric tons in 2010 to 36 billion tons in 2020 to 45 billion metric tons in 2040, a 46% increase, which will undoubtedly have terrible environmental consequences. Natural processes can only absorb about half of the anthropogenic carbon dioxide emissions produced annually leading to a positive imbalance and contributing to the increase of greenhouse gases in the atmosphere [2]. Our reliance on these fuels is growing increasingly unsustainable. Therefore there is an urgent need to develop alternative and sustainable sources of energy that are carbon neutral. Since fossil fuels are a derivative of photosynthesis and solar energy capture, it is only natural to look to nature for a solution.

In 2011, the International Energy Agency stated that solar energy, in the forms of solar heat, solar photovoltaics, solar thermal electricity, and solar fuels, could make considerable contributions to solving many of the world's problems, such as climate change, energy security, and universal access to modern energy services. Furthermore, solar energy offers a clean, climate-friendly energy source that is abundant and inexhaustible. The global energy needs for one year can be met by sunlight that strikes the Earth in 90 minutes. In recent years, the high

costs associated with solar energy technologies have become increasingly more competitive, such that it could replace oil-fueled economies in the future. However, cost is the biggest obstacle preventing solar energy conversion devices from having a larger market due to the current affordability of fossil fuels [3].

1.2 Photosynthesis and Photosystem I

The primary source of energy for nearly all life on the Earth is the Sun. The energy of sunlight is introduced into the biosphere by a process known as photosynthesis, which occurs in plants, algae and bacteria. The photosynthetic process arises in a set of complex protein molecules that are located in and around a highly organized membrane. Through a series of energy converting reactions, the photosynthetic apparatus transforms light energy into a stable form of energy that can be stored for millions of years.

Photosynthesis is arguably the most important biological process on earth. By liberating oxygen and consuming carbon dioxide, it has transformed the world into the hospitable environment we know today. Directly or indirectly, photosynthesis fills all of our food requirements, many of our needs for building materials, and nearly all the fuel sources that we use today. The energy stored in petroleum, natural gas, and coal all came from the sun via photosynthesis, as does the energy in biomass, which is a major fuel in many parts of the world. This being the case, scientific research into photosynthesis is vitally important. The energy-harvesting secrets of photosynthetic organisms can be adapted to man-made systems which provide new, efficient ways to collect and use solar energy. Because photosynthesis helps control the makeup of our atmosphere, understanding photosynthesis is crucial to understanding how carbon dioxide and other greenhouse gases affect the global climate.

In plants, algae and certain types of bacteria, the photosynthetic process results in the release of molecular oxygen and the removal of carbon dioxide from the atmosphere that is used to synthesize organic materials, like carbohydrates (oxygenic photosynthesis). Other types of bacteria use light energy to create organic compounds but do not produce oxygen (anoxygenic photosynthesis). Photosynthesis is the main pathway for assimilation of the inorganic carbon in the biological cycle. It accounts for 98% of the world's atmospheric oxygen production and avoids the increase in the concentration of CO_2, thus, preventing overheating the Earth due to the greenhouse effect [4]. Although, photosynthesis occurs in cells or organelles that are typically only a few microns (10^{-6} m), the process has a profound impact on the Earth's atmosphere and climate. Each year more than 10% of the total atmospheric carbon dioxide is reduced to carbohydrates by photosynthetic organisms.

Photosystem I (PSI) is a large pigment protein complex involved in cyanobacterial, algal, and plant photosynthesis. PSI provides both a large antenna for harvesting solar energy and the reaction center that converts these excitons into a stable charge separation. It has been determined that PSI has an internal quantum yield near 1.0 [5]. The robust and stable nature of PSI has led to many studies using PSI in *in vitro* applications for alternative energy solutions, such as hydrogen or direct electricity production as part of biohybrid devices or materials [6-11].

The electron transport chain in the thylakoid membrane of cyanobacteria is shown in Figure 1.1. When the cell is hit by sunlight, the energy from a photon excites the P_{680} complex of photosystem II, which initiates water splitting and transfer of the electron released from splitting water into oxygen and protons. Electrons are then transferred to the membrane bound b_6f complex and then transferred to the photosystem I complex, which is also excited by photon energy, via a soluble cytochrome c_6 and eventually to a ferredoxin (Fd) electron acceptor.

Electrons shuttled across the thylakoid membrane can be used by the ferredoxin-$NADP^+$-reductase (FNR) to reduce $NADP^+$ to NADPH, which is a cofactor necessary for carbon fixation in the Calvin Cycle or to reduce protons to molecular hydrogen by hydrogenases if they are present in the cell.

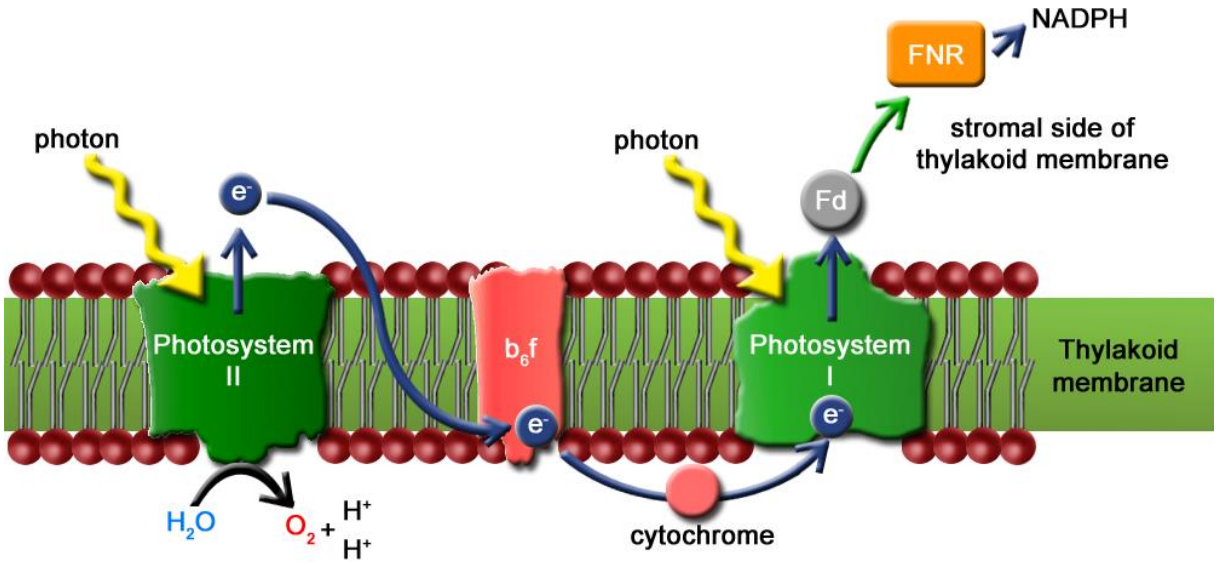

Figure 1.1. Electron transport chain within the thylakoid membrane of cyanobacteria.

In cyanobacteria, PSI is located in the thylakoid membrane and exists primarily as homo-trimeric complexes of the PSI monomer, a multi-subunit complex with several membrane-spanning domains [12]. The monomer of PSI from *Thermosynechococcus elongatus* (*T. elongatus*) is made up of 12 subunits. The PsaA and B subunits contain the majority of the transmembrane helices, the reaction center pigments including P_{700}, ~100 light harvesting chlorophyll *a* (chl *a*), carotenoids, quinones, and the proximal iron-sulfur cluster (F_x) that functions as an electron acceptor [12, 13]. The PsaC, D, and E subunits do not contain transmembrane domains yet are stably associated on the stromal surface of the thylakoid. The

terminal electron acceptors, F_A and F_B are found in this stromal domain and coordinated via PsaC. Electrons are transferred from F_B to the soluble FeS protein, ferredoxin, upon its transient association with the PsaD and E subunits [14]. Ferredoxin then provides electrons to support carbon fixation and other redox reactions. The monomer has an approximate diameter and height of 15 nm and 9 nm (Figure 1.2A), respectively [15]. It was determined from the crystal structure of trimeric PSI from the thermophilic *T. elongatus* resolved at 2.5 Å [12] that the trimer has a clover-leaf-structure with a diameter of 22 nm (Figure 1.2B) [16]. Hydrodynamic diameter measurements from dynamic light scattering of a single trimer have estimated its dimension to be 30 nm in diameter by 9 nm in height suggesting the presence of additional mass around the periphery of the complex that can be assumed to be lipid or detergent [17].

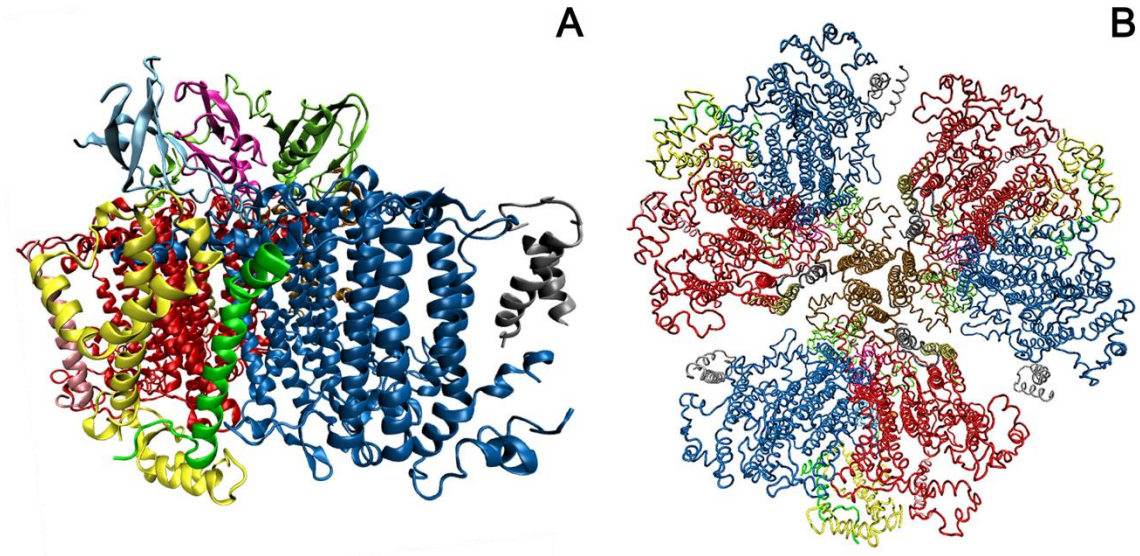

Figure 1.2. Crystal structure of *T. elongatus* PSI. (A) PSI monomer (PDB ID:1JB0) shown stromal side up. (B) Trimeric PSI complex constructed from 1JB0 structure shown lumenal side up.

Utilizing its light absorbing cofactors like chlorophyll and carotenoid molecules, which are excited by light, PSI has the ability to transfer electrons and convert excitation energy into chemical energy. PSI contains a reaction center (P_{700}/P_{700}^{*}) that is a powerful biological reductant. With a midpoint potential of -1.3 V [18] in its charge-separated state, considerable interest in using PSI for donating electrons upon the application of light energy allows for electron transfer from the PSI complex to surfaces for generation of photocurrent. Integrating redox proteins like PSI into photo-electrochemical cells requires a strategy that allows for enhanced direct or mediated electron transfer between the active sites of PSI to an electrode surface by minimizing the transfer distance and time of electrons since most electron transfer loss is due to charge recombination. In such a process, the primary electron donor, the P_{700} reaction center in PSI, is excited to P_{700}^{*} (E_m = -1.3 V vs. SHE) [19-21]. The excited electron in P_{700}^{*} is passed to the primary electron acceptors, F_A/F_B (E_m = -520 mV/-580 mV vs. SHE), which in turn reduces ferrodoxin (E_m = -440 mV vs. SHE). The resulting oxidized reaction center, P_{700}^{+} ($E_m \approx$ 490 mV vs. SHE) is then reduced back to P_{700} (E_m = 430 mV vs. SHE) after absorbing one electron from a reducing reagent.

1.2.1 The crystal structure of PSI from *Thermosynechococcus elongatus* as a surrogate for PSI from *Synechocystis* PCC 6803

The work in Chapters 2 and 3 utilized PSI from the thermophilic *T. elongatus* (*T.e.*) for *in vitro* applications that did not require genetic manipulation. However, in Chapter 4, it was necessary to insert a sequence on the C-terminus of a subunit of PSI so that it could be covalently attached to a conductive surface via a highly-specific transpeptidase reaction. Therefore, the model cyanobacterial organism *Synechocystis* PCC 6803 (6803) was utilized due to its ability to undergo spontaneous transformation and integrate foreign DNA into its genome via homologous

recombination. Unlike the well-characterized PSI from *T.e.* the crystal structure of PSI from 6803 has not been resolved. The PSI from 6803 is comprised of 11 subunits, rather than 12 like the PSI from *T.e.*, where the former lacks the PsaX subunit.

Using EMBOSS Needle (Needleman-Wunsch global alignment) [22] sequences for the subunits of PSI from 6803 and *T.e.* obtained from Kazusa Cyanobase (http://genome.microbedb.jp/CyanoBase) were aligned to determine the identity and similarity between the two species. In a Needleman-Wunsch global alignment, the entire length of each sequence is aligned where an overlap occurs between the two sequences; one sequence may be completely within the other or the ends can overlap. This alignment does not penalize for hanging ends of the overlap, gaps, or failing to align missing bases. The sequence identity is defined as the percentage of identical matches between the two sequences over the alignment, including any gaps in the global sequences. The sequence similarity is defined as the percentage of matches between the two sequences over the global alignment, including gaps. An identity of 25% or higher implies similarity in function and 18-25% implies similarity of structure or function. After analyzing the sequences of the subunits between the two PSI species, it was determined that the crystal structure of PSI from *T.e.* would be an appropriate surrogate for the structure of PSI from 6803 and analysis of its C-termini to determine sites for genetic manipulation since all of the subunit comparisons yielded both an identity and similarity of greater than 25%.

Table 1.1. Summary of sequence alignment results of subunits of PSI from *Thermosynechococcus elongatus* compared to PSI from *Synechocystis* 6803.

	Amino acid length				
Subunit	***T.e.***	***6803***	**Identity (%)**	**Similarity (%)**	**Gaps (%)**
PsaA	755	751	87.5	92.7	0.5
PsaB	741	731	86.3	92.2	1.6
PsaC	81	81	95.1	97.5	0
PsaD	139	141	66.9	77.5	2.8
PsaE	76	74	61.0	76.6	5.2
PsaF	164	165	60.0	73.3	0.6
PsaI	38	40	65.0	75.0	5.0
PsaJ	41	40	65.9	75.6	2.4
PsaL	155	157	73.9	83.4	1.3
PsaM	31	31	80.6	90.3	0.0
	6803 K1	**6803 K2**	**Identity (%)**	**Similarity (%)**	**Gaps (%)**
6803 PsaK1 vs. 6803 PsaK2	86	128	28.9	37.5	32.8
	T.e.	**6803 K1**	**Identity (%)**	**Similarity (%)**	**Gaps (%)**
T.e. PsaK vs. 6803 PsaK1	93	86	42.1	54.7	11.6
	T.e.	**6803 K2**	**Identity (%)**	**Similarity (%)**	**Gaps (%)**
T.e. PsaK vs. 6803 PsaK2	93	128	35.6	45.2	36.3

1.3 Scope of Work

The abundance of solar energy and the attractive features of PSI: ability to capture photonic energy, undergo charge separation, transfer electrons efficiently, inexpensive and simple extraction, make PSI an excellent candidate for coupling with metals or other proteins to produce hydrogen or adsorbed or linked to conductive materials to produce electricity. The objective of the work presented in this dissertation was to determine parameters that would allow for optimization of these systems to enhance photo-catalyzed hydrogen production from platinized-PSI particles and current production on PSI covalently attached to a gold electrode.

Due to the light-catalyzed behavior of PSI, some of the variables that can be considered for enhancing electron transfer are: the intensity of light the protein is exposed to, the

temperature at which reactions are carried out, concentration of metal present in solution, compatibility of electron mediators, and distance between reaction sites. Since PSI is a membrane bound protein, the type and amount of detergent used to solubilize PSI and retain its activity by creating biomimetic environments for *in vitro* studies also needs to be considered.

For the hydrogen-evolving system, the light intensity, temperature, and platinum salt concentration were varied during the platinum-photo-reduction process to determine their effect on the hydrogen yield by creating platinum nanoparticles of different morphologies, presumably directly on the stromal side of PSI, which minimizes the electron transfer distance for reduction of protons to molecular hydrogen. It was determined that the concentration of the platinum had the greatest impact on the hydrogen yield and optimal parameters for the light intensity, temperature, and platinum concentration were determined for the platinization process.

To understand what these particles look like in solution, small-angle neutron scattering (SANS) was used to investigate the structure of trimeric PSI from *Thermosynechococcus elongatus* stabilized in n-dodecyl-beta-D-maltoside (DDM) detergent solution to determine the orientation of the detergent molecules to gain insight on their orientation. The resulting PSI-DDM reconstruction structure showed the detergent oriented around the hydrophobic and interstitial periphery of the trimer in a non-uniform manner and did not appear to associate on the stromal or lumenal surfaces.

Understanding that the presence of detergent molecules is unlikely to interfere with the attachment of PSI to other proteins or surfaces, due to their localization to the hydrophobic transmembrane domains of PSI and absence on non-hydrophobic faces allowed us to covalently attach PSI to a planar gold surface using sortase-mediated ligation (SML) and further characterize the electron transfer behavior of PSI for light-catalyzed reactions, but on surfaces

rather than in solution. Previous attempts to attach PSI to conductive surfaces have exhibited moderate current densities and that PSI retains bioactivity when integrated into solid substrates. Furthermore, these techniques allow for dense deposition of the protein, but fail to control the orientation of PSI on the surface. The highly specific SML reaction was used to covalently attach PSI on tri-glycine functionalized gold surfaces. The exposed C-termini of PSI subunits from *Synechocystis* sp. PCC 6803 were targeted to study SML to control the orientation of PSI on gold for enhanced electron transfer, which yielded a 50% increase in current production from <100 nA/cm^2 to ~150 nA/cm^2 compared to other monolayers, in the presence of $K_4Fe(CN)_6$ as an electron donor and using the optimal light intensity determined from the platinized-PSI system. This result further contributes to the understanding of PSI integrated into systems containing noble metals for electron transfer and shows that the protein is sufficiently close to the surface for electron transfer, that SML is compatible with attaching PSI to solid substrates, and its bioactivity is not hindered by SML, the presence of detergent, or the selected redox mediator.

1.4 Applications utilizing photosynthetic reaction centers

To better understand where the future of this research could go, we must understand what has already been established. This section summarizes some of the efforts in biological hydrogen and current density production to date. A reason for pursuing artificial-photosynthesis technology is due to the fact that molecular nanoparticles are cheaper, lighter, and more environmentally sound when compared to current solar panel technology. Aside from providing a renewable energy source and decreasing our reliance on rapidly diminishing fossil fuels, it has also been suggested that artificial photosynthesis on a large industrial scale could reverse global warming since the process consumes CO_2 and releases O_2. With the potential of beneficial

impacts on the environment and energy supply, continued research into combining nanotechnology and natural processes should remain a central goal.

Nature provides finely tuned molecular machinery for solar energy conversion found in photosynthetic microorganisms that allow them to capture photonic energy and convert this energy to drive oxygenic water-splitting and carbon fixation. These energy converting biomachines can be used to convert water to environmentally friendly hydrogen to be utilized as an energy carrier or photovoltaic technology. Both avenues offer potentially long-term solutions for meeting future energy demands. Recently, there have been several strategies developed to enhance photosynthetic efficiency for solar fuel production by augmenting natural photosynthetic systems with metal and biological catalysts for hydrogen production and deposition of photosynthetic reaction centers like PSI to conductive surfaces for electricity production.

1.4.1 Hydrogen production

One pathway for solar energy conversion is towards the production of hydrogen for use as an alternative to hydrocarbon-based fuels. Its use depends on releasing the 143 kJ/g of energy available in the heat of combustion of the reaction: $H_2 + ½\ O_2 \rightarrow H_2O$. Hydrogen is an energy carrier, rather than a fuel and does not exist in mineable quantities on Earth. The current methods of hydrogen production include electrolysis of water or steam reformation of methane. These methods are costly and not carbon-neutral.

Hydrogen generation from electrolysis of water is described by the reaction: $H_2O \rightarrow H_2 + ½\ O_2$ and requires an energy input of at least 143 kJ/g of energy. This reaction occurs in an electrolytic cell, where an electromotive force is induced between the cathode and anode, which

are contained in separate vessels and connected via a salt bridge. The negatively charged electrode combines electrons with protons, which produces hydrogen. The positively charged electrode extracts electrons from water, which produces oxygen. A wire carries electrons from the anode to the cathode, and the salt bridge maintains the necessary electrical neutrality. To maintain a finite driving force and to overcome losses due to resistance between the two cells, electrolysis of water requires application of an overpotential. This means that a greater input of energy is required than by what is attained by the thermodynamic midpoint potential needed. Therefore, not all of the electrical power input is converted into the chemical bond energy of hydrogen.

The industrially preferred method for hydrogen generation is by heating water and methane at high temperatures in the presence of a nickel catalyst. This steam reformation method is less expensive compared to electrolysis of water and is described by the highly endothermic reaction: $CH_4 + H_2O \rightarrow CO + 3\ H_2$. Additional H_2 can also be recovered via the water-gas shift reaction: $CO + H_2O \longleftrightarrow CO_2 + H_2$, by using the resulting carbon monoxide during steam reformation as a feedstock. There are several pitfalls associated with this process for hydrogen production. Carbon dioxide, a greenhouse gas associated with the consequences of climate change is a by-product of this process. Furthermore, converting methane to hydrogen is an ineffectual way to produce a useful transportation fuel, because it is a poor exchange of one useful fuel for another due to the loss of energy during conversion.

Due to the energy losses and expensive costs associated with hydrogen production from current processes, alternative methods are being sought out via renewable sources. Solar energy conversion is a particularly good candidate due to its inexhaustible nature and the sufficient amount of solar energy that strikes the Earth's surface to meet global energy demands. There

have been many advances with light-induced bio-hydrogen production in recent years by coupling the redox properties of PSI with traditional and enzymatic hydrogen catalysts. The goal of these couplings is to produce hydrogen by the half-cell reaction $2H^+ + 2e^- + 2\ h\nu \longleftrightarrow H_2$, such that electrons can be delivered at high quantum yields, thermodynamic efficiency, and high rate. Below we discuss some of the techniques that have been used thus far in an attempt to optimize the configuration of a PSI-based system to reduce protons to hydrogen.

1.4.1.1 Hydrogen Production via Traditional Metal Catalysts

Hydrogen catalysis has typically been achieved through the use of noble metals, such as platinum and gold. These metals are able to catalyze the reaction $2\ H^+ + 2e^- \rightarrow H_2$, where the protons adsorb to the surface of the metal catalyst and combine with an electron to form one hydrogen atom. A H_2 molecule is formed by the covalent bonding of two adsorbed H atoms, which can then desorb from the metal (Pt) surface. On noble metals, this process has a midpoint potential of -420 mV at pH 7.0, with no overpotential and while non-noble metals are also able to catalyze this reaction, large overpotentials may be required, which leads to a loss of efficiency that is not desirable.

A challenge that needs to be overcome with using PSI for the photo-production of hydrogen is the diffusion limitation that may occur between the protein and its catalyst if they are not directly linked. Electrons must be transferred from the F_B cluster of PSI to the catalyst within 60 ms to prevent charge recombination within PSI. An initial approach by Greenbaum and co-workers [23-25] successfully mitigated the distance effect on electron transfer between PSI and platinum catalysts by directly depositing platinum nanoparticles onto thylakoid membranes and PSI complexes, where a platinum salt (hexachloroplatinate, $[PtCl_6]^{2-}$) was combined with

spinach chloroplasts and illuminated, causing the Pt^{4+} ions to be reduced to Pt (solid). Under continued illumination, the PSI complexes with solid platinum nanoparticles deposited on its surface led to hydrogen production and the deposition of 50 to 500 Pt atoms when the maximal rate of hydrogen was evolved [26]. It was shown that metal deposition was also possible with hexachloroosmiate ($[OsCl_6]^{2-}$) [27] and hexachlororuthenate ($[RuCl_6]^{2-}$) [28]. The highest rates of hydrogen evolution occurred with the osmiate precipitate at a rate of 0.113 mol H_2/mg chl *a*/h. When sodium ascorbate (NaAsc), a sacrificial electron donor and plastocyanin (PC), the native electron donor for spinach/plant PSI were used to reduce oxidized P_{700}^{+}, the photo-induced hydrogen yielded was 0.025 μmol H_2/mg chl *a*/h [29]. A 3-fold higher rate was accomplished by eliminating diffusion-limitations by crosslinking PC to the reaction center, yielding an evolution rate of 0.080 μmol H_2/mg chl *a*/h [30]. More recently, Iwuchukwu et al. attained a light-induced hydrogen yield by platinized PSI from the thermophillic cyanobacterium *Thermosynechoccocus elongatus* yielding a rate of 5.5 μmol H_2/mg chl *a*/h [31]. This allowed for the platinized system to be operated at higher temperatures (55°C) and observable system stability was maintained for 85 days, when tested intermittently. A major disadvantage of reduction of metal salts on PSI particles is the large amount of Pt (or Os or Ru) required. It is possible that many of the deposited metal atoms are not actively involved in catalysis, due to their improper location on the surface of PSI and these atoms are inaccessible to protons, nor will they receive electrons to reduce the protons to hydrogen, which may not be economical in the long run.

In the work by Grimme et al. PSI from *Synechocystis* PCC 6803 was directly wired to preformed platinum bioconjugates via a dithiol molecular wire to generate hydrogen when illuminated [32, 33]. An altered form of the PsaC subunit containing a free cysteine allowed for the covalent attachment of 3 nm platinum or 12 nm gold particles using the molecular wire.

Under saturating white light (2500 μE) in the presence of NaAsc as a sacrificial electron donor and 2,6-dichlorophenolindophenol (DPIP), the electron mediator and substitute for cyt *c*, the wired PSI-metal bioconjugates generated 3.4 μmol H_2/mg chl *a*/h and 9.6 μmol H_2/mg chl *a*/h for gold nanoparticles and platinum particles, respectively [32]. The addition of cytochrome to the Pt system increased the hydrogen evolution rate to 49.6 μmol H_2/mg chl *a*/h. To maximize the hydrogen production of these bioconjugates, PC isolated from spinach leaves was cross-linked to spinach PSI core complexes that had been rebuilt using the Cys_{13}Gly variant of PsaC and molecular wires of varying lengths [33]. Bioconjugates constructed from the PC cross-linked spinach PSI evolved H_2 at rate of 98.6 μmol H_2/mg chl *a*/h under 70 μE/m^2/s light intensity. Using 1,8-octanedithiol, 1,10-decanedithiol, 1, 4-benzenedithiol and 4, 4'-biphenyldithiol as molecular wires, hydrogen evolution rates of 49.0 μmol H_2/mg chl *a*/h, 16.0 μmol H_2/mg chl *a*/h, 150.5 μmol H_2/mg chl *a*/h and 92.5 μmol H_2/mg chl *a*/h where obtained, respectively. A one-time H_2 evolution measurement under "optimal conditions" (solution buffer at pH 6.0, cross-linked PC, rebuilt PsaC PSI, and 1,4-benzenedithiol molecular wire) yielded a rate of 312 μmol H_2/mg chl *a*/h for a PSI-molecular wire-Pt bioconjugate [33].

1.4.1.2 Hydrogenase-mediated Hydrogen Production

To bypass the need for large amounts of rare noble metals, a system that employs metals or biomolecules that are abundant is highly desirable. Such a system may utilize a hydrogenase enzyme as the catalyst, which make use of iron and/or nickel cofactors to reduce protons to molecular hydrogen. Hydrogenases (H_2ases) are enzymes that are found in many microorganisms that perform the reversible reaction $2H^+ + 2e^- \longleftrightarrow H_2$. Three distinctive classes of H_2ases are known: [NiFe]-H_2ases, [FeFe]-H_2ases, and [Hmd]-H_2ases [34-36]. The focus of

this section will be on applications using [NiFe]-H_2ases, which are active in H_2 uptake/oxidation reactions and are often more stable and oxygen tolerant, and [FeFe]-H_2ases, which are frequently involved in H_2 evolution, but are significantly more oxygen-intolerant than [NiFe]-H_2ases and become inactivated. The scope of this thesis does not utilize H_2ases, therefore an in-depth overview will not be included here (for recent reviews, see [37, 38]).

Initial studies using H_2ase enzymes showed hydrogen evolution by the direct transfer of electrons from dithionite-reduced spinach PSI to both H_2ase I and H_2ase II from *Clostridium pasteurianum* was observed in the dark [39]. A hydrogen evolution rate of 0.01 μmol/h/mg H_2ase was observed from H_2ase purified from *Clostridium pasteurianum* H_2ase mixed with 5 mM dithionite and 0.96 mg chl/mg PSI. Light dependent hydrogen evolution was also observed, using high potential electron donors to PSI, H_2ase I, and purified PSI or thylakoids [39]. In this system, sodium ascorbate (NaAsc) and dithiothreitol served as electron donors to PSI. The rate of hydrogen evolution with the purified PSI yielded a rate of 0.00003 μmol H_2/h/mg H_2ase with 2.4 μM PSI and 0.0003 μmol H_2/h/mg H_2ase with thylakoids. Despite their modest outputs and severe oxygen inhibition, these initial experiments showed the potential for using these enzymes for hydrogen evolution in aqueous solution, but revealed the need to directly link these proteins for enhanced electron transfer.

In 2006, Ihara and co-workers demonstrated light-driven hydrogen production by a hybrid complex of [Ni-Fe]-H_2ase and the cyanobacterial photosystem I [40, 41]. It was deduced using X-ray crystal structures that fusing a [NiFe]-H_2ase from *Ralstonia eutropha* (*R. eutropha*) H16 to the PsaE subunit of the stromal side of PSI from *Thermosynechococcus elongatus* could minimize the distance between F_B to a [4Fe-4S] cluster to approximately 14 Å, which is sufficiently short enough for electrons to be effectively transferred within ~60 ms. Though using

aqueous *in vitro* mixtures of PSI and hydrogenase to evolve hydrogen is possible, the formation of direct fusion complexes of the proteins enhances the rate of hydrogen production by five times compared to a mixture of the two proteins. They were the first to report a fusion of the membrane bound [Ni-Fe]-H_2ase from *R. eutropha* H16 and the peripheral PSI subunit PsaE of the cyanobacterium *Thermosynechococcus elongatus* [40], where a H_2ase-PsaE fusion was associated with a PsaE-free PSI that yielded a photo-induced hydrogen rate of 0.58 μmol H_2/mg chl *a*/h.

Although the direct fusion of H_2ase to PSI was a clever technique to decrease the electron transfer distance between the proteins to enhance hydrogen production, the modest result was unexpected. The rate-limiting step of this system is likely the transfer of electrons between the photochemical and catalytic molecules, which is dependent on the relative orientation of the two enzymes. The probability that the respective iron-sulfur clusters are in alignment suitable for electron transfer is likely low. To overcome the electron transfer deficits of the H_2ase-PSI fusion, Lubner et al. expanded on the method of linking PSI to other particles using a molecular wire by Grimme et al. [32] to produce hydrogen by replacing platinum nanoparticles with H_2ase [11]. The Hyd A protein of [Fe-Fe]-H_2ase from *Clostridium acetobutylium* (*C. acetobutylium*) was linked to PSI from *Synechocystis* PCC 6803. The F_B cluster of the Cys_{13}Gly mutant of PsaC on PSI was covalently linked to the distal [4Fe-4S] of the Cys_{97}Gly mutant of the H_2ase enzyme using a 1,6-hexanedithiol molecular wire. The mutant Hyd A enzyme had a hydrogen evolution activity of 11.5 mol H_2 evolved/s/mol H_2ase which was significantly lower than the wild type enzyme activity of 80.6 mol H_2/s/mol H_2ase. In the presence of cyt c_6, sodium ascorbate (NaAsc), and 2,6-dichlorophenolindophenol (DPIP) , which acted as soluble electron donors, the photo-induced hydrogen evolution rate of this system was 3.9 μmol H_2/mg chl *a*/h. This is

significantly lower than the PSI-molecular wire-Pt system which yielded a rate of 312 μmol/mg chl *a*/h. The disparity of the two systems is likely the oxygen inhibition of the [Fe-Fe]-H_2ase, like nearly all hydrogenases.

In 2011, Lubner et al. improved upon their molecular wiring technique by tethering the terminal [4Fe-4S] cluster of PSI from *Synechococcus* sp. PCC 7002, F_B, to the distal [4Fe-4S] cluster of the [FeFe]-H_2ase from *C. acetobutylicum*. This is achieved by site-specific conversion of a ligating Cys residue (C13) of F_B to a Gly [42-44] and by chemically rescuing the cluster with a small sulfhydryl containing molecule. The hydrogen evolution rate of this system was further enhanced by chemical cross-linking of cytochrome to the lumenal side of PSI yielding an average rate of 2200 ± 460 μmol H_2/mg chl *a*/h. In their study, they varied the buffer, pH, and linker lengths to optimize photo-induced hydrogen production. It was determined that using 1,8-octanedithiol linker in a medium of sodium-phosphate buffer at pH = 6.5 was optimal, yielding a one-time maximum rate of 2839 μmol H_2/mg chl *a*/h.

Another viable method for biological hydrogen production is immobilization of a PSI-H_2ase fusion to an electrode. Krassen et al. created a fusion using PSI from *Synechocystis* PCC 6803 and H_2ase from *R. eutropha*, which was attached to a gold electrode via a histidine/Ni-NTA interaction, where a decahistidine tag was engineered on lumenal side of the PsaF transmembrane subunit of PSI. Electrons were provided by the gold electrode and transferred through P_{700} by a soluble electron carrier, N-methylphenazinium methyl sulfate (PMS), and eventually to the active site of the H_2ase hydrogenase upon light excitation. This immobilized PSI-H_2ase hybrid complex produced hydrogen at the rate of 4500 ± 1125 mol H_2/min/mol hybrid complex (3150 μmol H_2/mg chl *a*/h) [7]. Though this value is impressive, the rate of hydrogen evolution had a lifetime of a few minutes, which limits the usefulness of this system for as an

applicable device. In another attempt at immobilization of a similar H_2ase complex from the green algae complex, *Chlamydomonas reinhardtii,* using carboxy-terminated self-assembled monolayers and methyl viologen as the electron mediator, this system produced hydrogen at a rate of 85 mol H_2/min/mol H_2ase [45].

Though Lubner et al. outperformed natural photosynthesis [46] by overcoming diffusion limitations for electron transfer by directly wiring reaction centers of PSI and hydrogenase and tethering a redox mediator to PSI, their system remains temporally unstable. Our work to optimize platinum nanoparticle-decorated PSIs for increased hydrogen yield has previously shown to be remain active for several months and therefore a systematic factorial design could be adapted to integrate techniques that enable enhanced electron transfer as described above and therefore increased hydrogen yield with long-term stability and further improve our understanding of electron transfer behavior of PSI-based technologies.

1.4.2 Electricity production

PSI has shown to be a highly versatile redox protein that can be integrated with metal and biological catalysts for electron transfer, as discussed previously. Another opportunity that can be pursued to study electron transfer performance in PSI is attachment to planar conductive substrates, such as protein-based photovoltaic technologies. Though biophotovoltaics need to prove themselves against current photovoltaic technology, with efficiencies at least two orders of magnitude greater than the best photosynthetic based materials, the abundance and robustness of these photosynthetic reaction materials have their advantages. With a quantum efficiency of near unity [5], and 1 V potential, the photosynthetic reaction center, photosystem I (PSI), is an ideal candidate for incorporation into a steady-state photovoltaic device. With cheap and easy

extraction, PSI can be adsorbed or linked to conductive or semi-conductive materials to produce electricity. Though many strategies for immobilizing PSI onto conductive substrates or materials (gold, titanium oxide, silicon, graphene, or gallium (III) arsenide (GaAs), carbon nanotubes or other nanoparticles, and redox polymers) have arisen, the focus of this review is on immobilization of PSI monolayers on gold, as will be discussed in Chapter 4.

The origins of using photosynthetic complexes on electrodes began with the work done by Greenbaum that showed that PSI complexes immobilized on gold behaved like diodes, which allowed for electron transfer in a vectorial direction parallel to the electron transport chain of the protein [47]. Using scanning tunneling spectroscopy, where I-V scans were performed using a scanning probe above individual protein complexes attached by electrostatic interactions with thiol-surface treatments, changes in the shape of the resulting scans were attributed to different orientations of the electron transport vector of PSI thereby allowing one to elucidate the orientation of PSI on a surface. Building on this observation, Munge et al. used cyclic voltammetry to observe direct electron transfer between the P_{700} reaction center and the F_A/F_B iron sulfur clusters of PSI [48].

Attachment of PSI to gold surfaces typically involves self-assembled monolayers (SAMs) of organothiol-based compounds. In 1997, Lee et al. used SAMs terminated with –OH, –COOH, and –SH groups to attempt oriented immobilization of PSI, yielding 70% useful orientation when using an organic compound terminated with an –OH group [47]. Much of the recent progress in PSI-immobilization for current production has occurred during 2004 to the present. Das et al. oriented PSI by recombinantly expressing the PsaD subunit of PSI with a His_6 tag so that it could bind to Ni-NTA functionalized gold [49]. The natural PsaD of PSI was exchanged with the PsaD-His_6 mixing wild type PSI with stoichiometric excess of the recombinant subunit. This

method yielded PSI with a stromal side down orientation. The Terasaki group has fabricated high-surface area electrodes comprised of gold nanoparticles decorated with PSI capable of producing larger currents compared to planar electrodes [50]. They have also engineered genetic mutants to directly wire PSI to a surface [51] and have created biohybrid sensors using this immobilization scheme [52]. In 2007, Frolov et al. generated cysteine mutants on the lumenal side of PSI [53] so that direct thiol coupling to a gold surface could occur while fabricating oriented multilayers of PSI by reducing platinum ions on the reducing stromal side of the protein to allow for Pt-sulfide bonds above the initial monolayer [54]. In addition, the group of Frolov and Carmeli used Kelvin probe force microscopy to measure the change in surface voltage by a PSI film when illuminated [55].

The groups of Cliffel and Jennings have also contributed to the field of PSI immobilization on surfaces. They began investigating the adsorption of PSI films onto substrates modified with SAMs with various ω-terminated alkanethiols [56] and showed increased reduction current and that the length of the alkanethiol has a significant effect on how ordered the resulting PSI monolayer will be. They also observed that PSI adsorbs to hydrophilic surfaces rather than hydrophobic surfaces due to the presence of Triton-X surfactant [57]. To speed up the time consuming preparation of PSI attachment on SAMs, Faulkner et al. developed a tandem strategy to covalently attached the PSI to functionalized SAMs with vacuum assistance which created dense monolayers of PSI [58]. In 2011, Ciesielski et al. immobilized dense monolayers of PSI onto aminoethanethiol SAMs functionalized with terephaldialdahyde (TPDA) and developed kinetic and electrochemical parameters to predict photocurrent production.

In 2010, Mukherjee et al. investigated the deposition of PSI on –OH terminated alkanethiol SAMs in an attempt to better control the morphology of PSI. They showed that using

a lower concentrations of PSI in conjunction with applying an electric field minimized PSI aggregation and yielded uniform coverage of PSI on the surface when compared to gravity-driven deposition [59]. To follow up with this work, they also investigated various conditions for a PSI-SAM/gold system, by studying the effects of temperature, monomeric or trimeric forms of PSI, the type and concentration of detergent used, and assembly assistance on the adsorption of PSI to the surface. This study also showed the use fluorescent antibody detection to determine orientation of PSI based on the dipole present in the protein [60].

In 2013, Manocchi et al. attached PSI onto gold SAMs that were functionalized with –CH_3 (hexanethiol), –CH_2-NH_2 (aminohexanethiol), –CH_2-OH (mercaptohexanol), and –COOH (mercaptohexanoic acid) terminated alkanethiols with the assistance of electric field to study the influence of various surface modifications. They demonstrated that PSI density could be controlled and the surface charge of the SAM had an influence on the quantity of bound PSI, especially for the –CH_2-OH and –COOH terminated SAMs [61].

Though these methods are effective for depositing dense monolayers or multilayers of PSI, their orientation within the layer(s) is generally unknown. Modeling by Ciesielski has shown that the distribution of orientation of a PSI monolayer is 70% of the reaction center with its F_B site accessible to the conductive surface, stromal side down, and 30% with the P_{700} site of the reaction center accessible to the conductive surface, or lumenal side down, based on lysine residues available for covalent bonding to a gold surface [8]. Orientation of the protein complex is important for obtaining useful current density. Though the stromal side down orientation is dominating over lumenal side down, in the case of a monolayer, current production will be observed, when terminal iron sulfur clusters (F_B) donate electrons to an electrode, while some of this current will be canceled out PSIs are oriented such that it can accept electrons from the

electrode, which may not desirable. It has been determined by modeling that for significant improvements in net current to be produced, at least 90% of the complexes must be oriented in the same orientation, whether an anodic or cathodic current is desired.

A selection of the current densities (nA/cm^2) produced from PSI photo-conversion of energy to date is listed in Table 1.2. For a comprehensive review of advancements in the progress and strategies for PSI-based photovoltaic energy conversion including non-gold based systems, see the review by Nguyen and Bruce [62].

In this dissertation, sortase-mediated ligation, which can create covalent protein fusions with other proteins or substrates via an extremely selective reaction, was employed to attempt to obtain highly oriented PSI monolayers on gold to enhance electron transfer and observe current densities greater than what has previously been shown by other PSI-gold monolayer systems and verify the model for protein orientation and current density proposed by Ciesielski.

Table 1.2. Sampling of the current densities produced per area for PSI immobilized on conductive surfaces for comparable attachment schemes/systems.

Author	**Method**	**current density (nA/cm^2)**
Faulkner et al. [58]	alkanethiol SAM (monolayer)	100
LeBlanc et al. [63]	p-doped silicon, PSI multilayer	875,000
Frolov et al. [54]	PSI-Pt, cysteine multilayer	120,000
Ciesielski et al. [64]	nanoporous Au-leaf	300
Terasaki et al. [51]	molecular wire, Au	40
Ciesielski et al. [65]	PSI multilayer, Au	7,900
Manocchi et al. [61]	alkanethiol SAM, Au	75
Ciesielski et al. [66]	PSI self-contained cell	1,500
Mershin et al. [67]	TiO_2	362,000
Le et al. [68]	SML, Au (monolayer)	225

1.5 Neutron scattering

The methodology described below was used in Chapter 3 to study the structure of isolated PSI that was reconstituted in n-dodecyl-β-D-maltoside to elucidate its solution structure to understand the potential impact the presence of detergent may have on the ability of PSI to be covalently attached and oriented unidirectionally on a gold electrode, while retaining its bioactivity so that it can be characterized electrochemically.

Neutrons are electrically neutral, subatomic, elementary particles, found in all atomic nuclei, except hydrogen (^{1}H). They are approximately 1,840 times more massive than an electron and have a nuclear spin of ½. Neutrons are only stable when bound by an atomic nucleus, while unstable free neutrons have a mean lifetime of approximately 900 s, decaying into a proton, an electron, and an anti-neutrino [69, 70]. Due to their weak interaction with atomic nuclei, neutrons are highly penetrating. This allows neutrons to probe samples in complex environments and measurement of bulk processes under physiological conditions [6-8]. Furthermore, an atom's scattering ability is independent of its atomic number, which allows neutrons to differentiate or locate "light" low atomic number atoms from "heavy" atoms. For example, in polymeric materials, neutrons can precisely locate hydrogen atoms [71, 72].

Hydrogen (^{1}H) has a negative coherent scattering length (= -0.37×10^{-12} cm) while deuterium (^{2}H or D) has a positive scattering length (= 0.67×10^{-12} cm) [73]. As a result, this difference in scattering power allows for hydrogen atoms to be contrasted from other atoms in a macromolecule. This contrasting feature allows the study of biological samples that are intrinsically rich in hydrogen, where ^{1}H can be substituted with ^{2}H, a powerful method for selectively tuning the contrast of a given macromolecule. Substituting hydrogen molecules for heavier molecules can allow the accentuation or masking of the scattering from particular parts

of a macromolecular complex, typically referred to as "contrast variation" [74-76]. Neutron contrast variation in H_2O/D_2O mixtures allows for determination of matching points for all major components of biological macromolecules (ex. ~10-15% D_2O for lipids and ~40% D_2O for proteins) [77]. Moreover, specific deuteration is a very effective method for highlighting selected structural fragments in complex particles. The scattering length density of deuterated protein or nucleic acid is significantly different from that of the protonated material and contrast variation on selectively deuterated hybrid particles allows positions of the labelled fragments to be established.

Small angle neutron scattering (SANS) probes structure in materials of length scales ranging from tens of angstroms (Å = 10^{-9} m) to hundreds of nanometers (nm = 10^{-7} m) [19]. The length scale, d, is determined by the neutron wavelength, λ, and the scattering angle, θ, Bragg's Law:

$$\lambda = 2d\sin\left(\frac{\theta}{2}\right)$$

Using SANS the size and shape of a particle, conformational changes, and molecular associations in solution can be elucidated. SANS is arguably a powerful neutron scattering technique for polymeric materials, biomolecules, and allows for the study of disordered materials that are difficult to crystallize. Advancements in neutron scattering in the last decade, namely the production of cold neutrons whose long wavelengths have greatly facilitated the investigation of materials with large unit cells such as proteins. The addition of enhanced collimation of the beam has allowed for length scales approaching tens of microns to be studied [78, 79].

In biological neutron scattering experiments, neutron beams of suitable wavelengths and energies are directed at a biological sample. When neutrons pass through the sample, they are scattered by atomic nuclei of the sample, which results in changes in the energy and momentum

of the incident neutrons. By measuring these changes, information about the structure and internal dynamics of atoms/molecules that make up the sample can be inferred [80]. In neutron scattering experiments, one measures the number of neutrons scattered within a solid angle between Ω and $\Omega+d\Omega$ with a change in energy $\hbar\omega$ and momentum $\hbar Q$. This number is proportional to the double-differential cross-section $\delta\sigma/\delta\Omega\delta\omega$, which in turn is proportional to the dynamic structure factor, $S(Q, \omega)$, (2):

$$\frac{\partial^2\sigma}{\delta\Omega\delta\omega} \propto S(Q,\omega)$$

The dynamic structure factor can be written in terms of the van Hove function, $G(r,t)$, which characterizes the space-time correlation of individual atoms as well as between pairs of atoms. In SANS experiments one measures the flux of neutrons of wavelength λ scattered into an angle θ. The scattering intensity $I(Q)$ is a function of the scattering vector:

$$I(Q) \propto P(Q)\cdot S(Q),\ Q = \frac{2\pi}{\lambda}\sin\left(\frac{\theta}{2}\right),$$

where $P(Q)$ is the particle form factor and $S(Q)$ the particle structure factor. SANS intensity profiles are obtained by examining scattering bodies, ensembles of particles that scatter in an identical way. The form factor $P(Q)$ takes into account interference effects between scattering by different atoms of the same scattering body and is given by:

$$P(Q) = \frac{1}{N_P}\int n(r)\exp[iQ\cdot r]\,dr,$$

where N_p is the total number of atoms in the scattering body and the scattered density $n(r) = \sum_{i=1}^{N_P}\delta(r-r_i)$, r_i is the coordinate of the i^{th} atom. $P(Q)$ is determined by the overall shape of the scattering body.

In the work presented in Chapter 3, we focus on the coherent scattering structure factor $S(Q)$ that is given by:

$$S(Q) = 4\pi\rho \int r^2 \left[g(r)-1\right] \frac{\sin(Qr)}{Qr} dr,$$

where g(r) is the pair-correlation function and ρ is the density of the scattering particles. The structure factor describes how I(Q) is modulated by interference effects between radiation scattered by different scattering bodies and can be used to gain information about the relative positions of these scattering bodies.

The radius of gyration (R_g) was determined from the Guinier region of the SANS data with the Guinier approximation [81]:

$$I(Q) = I(0)e^{\frac{Q^2R_g^2}{3}}$$

where I(0) is the forward scattering intensity, a shape-independent function of the total scattering power of the sample. A linear fit of ln(I(Q)) vs. Q^2 (a Guinier plot) provides I(0) and R_g from the y-intercept and slope, respectively [82].

Coupling SANS with simulations is a commonly used method to construct structural models of biological systems [83]. One application is rigid body modeling, where a high resolution structure, such as a well characterized crystal structure, is fit to a model that can correctly describe or replicate experimental SANS data. Rigid body modeling is usually improved by allowing configurational flexibility to the structures of interest via the use of coarse-grained molecular dynamics simulation [84]. When a crystal structure is unavailable for a molecule being studied, the shape of structure can be reconstructed *ab initio*, by placing dummy atoms to represent the solvent and sample and using Monte-Carlo-based switching to simulate the placement of the components of the system [85-87].

The combination of molecular dynamics simulation and neutron scattering techniques has emerged as a highly concerted approach to elucidate the structure, dynamics, and function of biological systems at an atomic level. Simulation models can be verified by calculating neutron

scattering structure factors and comparing the results directly with experimental results. If the simulated scattering profiles fit well to the experimental profiles, the simulation can provide further insight for interpretation of the experimental result. If the fit fails, the models can be logically adjusted until the systems converge.

Characterizing the structure and dynamics of proteins is essential to understanding the mechanisms of their biological functions that cannot be observed directly. Therefore, molecular simulation models are a powerful tool to elucidate physiological behavior. This can be done by directly comparing experimental and calculated scattering intensities. It can also be done indirectly by comparing the simulated system with the experimental one by examining "derived" quantities, such as the radius of gyration or fractal dimensions. However, it must be noted that determining these derived values requires approximations, assumptions, and model-dependent data interpretation [88].

Biological systems that contain multiple components, such as membrane proteins in lipid bilayers or free micelles, produce complex neutron scattering patterns and can be difficult to interpret. This is further complicated by the similarity in the scattering length densities that can occur from the different components. This problem can be avoided experimentally by the use of contrast variation techniques that allow the separation of the scattering profiles by tuning the replacement of hydrogen with deuterium and preparing pure samples that minimize extraneous particle species. Elucidating the individual scattering contributions from the various components is simplified with the use of molecular dynamics (MD) simulation, assuming the correct assumptions for the representative model system were used.

1.5.1 Understanding the detergent structure for reconstituted PSI in solution

Although the use of detergents is necessary to solubilize proteins and retain activity for *in vitro* studies, their presence in solution hinders understanding of protein-protein interactions and structural effects [17, 89, 90]. The difficulties associated with solubilizing membrane proteins such as PSI are due primarily to exposure of their hydrophobic domains, which are protected by the lipid bilayer *in vivo*. Therefore, it is important to account for detergent effects when studying membrane proteins. Previous investigations have been conducted on the structure of plant and cyanobacterial PSI complexes in solution using small angle X-ray (SAXS) and neutron (SANS) scattering [89, 91]. These techniques, which involve the comparison of experimentally determined data acquired for isolated PSI complexes stabilized in detergent solution to theoretical models of the solution conformation obtained through molecular dynamics (MD) simulations, is a valuable tool for interpreting protein solution structure.

Though detergents allow membrane complexes to be soluble in aqueous solution, their abundance and non-native characteristics can interfere with the ability to study protein-protein interactions and/or structural and functional properties [60, 92, 93]. The difficulties associated with solubilizing and stabilizing membrane proteins like PSI are due primarily to the exposure of its hydrophobic domains, which are protected by the lipid bilayer in the native environment. Therefore it is necessary to understand the effects of detergents used for membrane protein studies, as it has been shown that short alkyl chain detergents are more effective at solubilization than long alkyl chain detergents, which can cause protein denaturation [94, 95]. Furthermore, it is important to understand the impact of detergent micelles on membrane proteins in solution, particularly the protein-detergent interactions that affect protein conformation or cause aggregation. Recent studies [60, 96] have shown that the critical micelle concentration (CMC)

and critical solubilization concentration (CSC) are of particular importance for determining how effective a detergent is at solubilizing a membrane protein.

1.6 Sortase

Understanding PSI-detergent interactions will enable us to incorporate PSI into systems for photo-catalyzed electron transfer in solution or on solid substrates, such as in fusions with other redox proteins or attachment to surfaces for electricity production in a manner that minimizes the distance between redox centers that may be hindered by detergent or reduce activity, which would have a detrimental effect on electron transfer. Chapter 4 of this dissertation focuses on covalently attaching PSI to a gold surface in a highly uniform monolayer to improve electron transfer for light-induced current production. To achieve this goal, a sortase enzyme was employed. The sortase family of transpeptidase enzymes catalyzes sequence-specific ligation of proteins to the cell wall of Gram-positive bacteria as shown in Figure 1.3. *In vivo*, sortase A (srt A) from *Staphylococcus aureus* [97, 98], the enzyme utilized in Chapter 4 of this dissertation, is a cysteine transpeptidase, that hydrolyzes the threonine-glycine peptide linkage in a cell wall "sorting tag" (with the amino acid sequence LPXTG, where X is any amino acid, typically glutamic acid, E) to form a thioacyl intermediate. The intermediate undergoes a nucleophilic attack by an amino group of a $(Gly)_n$ unit ("n" signifies the number of repeats of the glycine residue, preferably $n \geq 3$) creating a new peptide bond and a resulting $LPXT(G)_n$ linkage. [99-102].

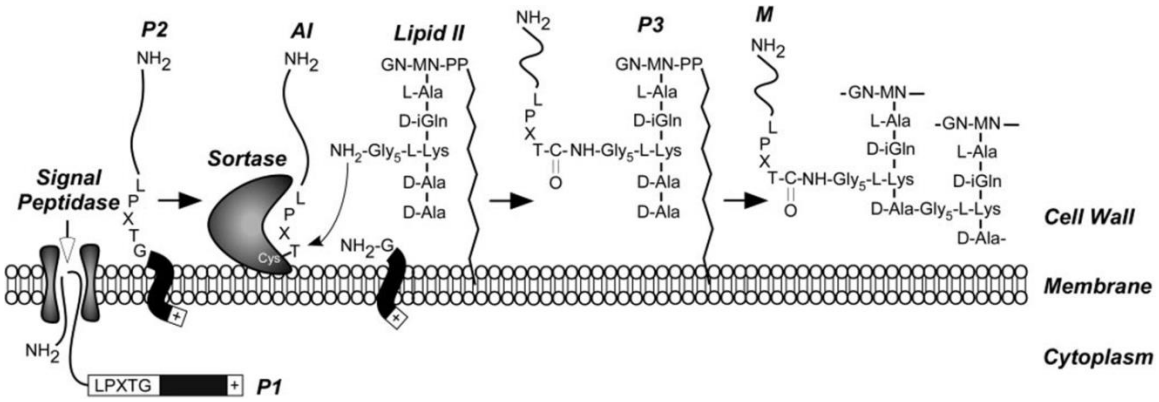

Figure 1.3. Anchoring of surface proteins to the cell wall in gram-positive bacteria via a cell sorting pathway, adapted from Marraffini et al., 2006 [99]. Surface proteins are first synthesized in the cytoplasm containing an N-terminal signal sequence and a C-terminal sorting signal. The signal sequence directs the cellular export of the polypeptide and upon translocation is cleaved by signal peptidase. This pathway is universal to many gram-positive bacteria. (Reprinted from Microbiology and Molecular Biology Reviews, Vol. 70/Issue 1, Luciano A. Marraffini, Andrea C. DeDent and Olaf Schneewind, Sortases and the Art of Anchoring Proteins to the Envelopes of Gram-Positive Bacteria, Pages 192–221, 2006, with permission from the American Society for Microbiology. http://mmbr.asm.org/content/70/1/192)

The enzyme activity of *Staphylococcus aureus* sortase A has been used *in vitro* to link various compounds displaying the C-terminal LPETG motif to compounds exposing either an 6-aminohexose moiety motif [103] or N-terminal glycine [97]. Other examples include: peptide nucleic acids, oligosaccharides, polyethylene glycol (PEG), lipids, fluorescent labels and green fluorescent protein (GFP), streptavidin, alkaline phosphatase, and for peptide cyclization [98, 104-108].

We are interested in using sortase for the attachment of proteins to solid supports for the production of light-induced current in the presence of PSI and an electron mediating solution. A critical prerequisite for applications of attaching proteins to solid substrates is the generation of a stable linkage between the immobilized protein to the support surface, while maintaining the functionality of the protein. A major advantage of utilizing sortase is the specificity of the enzyme enables proteins to be immobilized uniformly and in a defined orientation [109]. A range

of immobilization techniques have been utilized to attach proteins to surfaces including simple absorption, trapping the protein within a gel matrix, or covalent linkage. Chan et al. showed that sortase-mediated ligation (SML) could be used to link proteins to cross-linked polymer beads, beaded agarose, and planar glass surfaces by functionalizing them with an oligoglycine motif [110]. Clow et al. presented a method for a site-directed immobilization of recombinant proteins to a biosensor chip and showed that SML allowed for site-specific coupling in an orientated uniform manner. They also concluded that the high specificity of the sortase reaction allows immobilization of proteins from less than pure protein samples, which is an attractive benefit for time-saving and short cuts for protein purification especially those involving difficult protocols. However, one drawback of SML is the amount of protein immobilized cannot be controlled, as this reaction is dynamic and the equilibrium of bound and unbound proteins is constantly in flux, that is – coupled proteins can be re-cleaved [111]. Srt A has been demonstrated as a versatile and viable option for a wide variety of protein engineering and bioconjugation applications [112-114]. The simple yet specific mechanism of this enzyme makes it the ideal tool for site-specific protein ligation.

2. OPTIMIZATION OF PHOTOSYNTHETIC HYDROGEN YIELD FROM PLATINIZED PHOTOSYSTEM I COMPLEXES USING RESPONSE SURFACE METHODOLOGY

A version of this chapter was originally published by Iwuchukwu et al.:

Iwuchukwu, I. J.; Iwuchukwu, E.; Le, R.; Paquet, C.; Sawhney, R.; Bruce, B.; Frymier, P., Optimization of photosynthetic hydrogen yield from platinized photosystem I complexes using response surface methodology. International Journal of Hydrogen Energy 2011, 36 (18), 11684-11692. (http://www.sciencedirect.com/science/article/pii/S0360319911015400)

All response surface modeling, statistical analysis, ANOVA, and mathematical model development were contributed by Ernest Iwuchukwu and interpretation of the resulting platinization/hydrogen evolution yield was a collaborative effort with Ifeyinwa Iwuchukwu. All figures and tables have previously appeared or were adapted from the reference above or the dissertation of Ifeyinwa Iwuchukwu, "Protein engineering for the Enhanced Photo-production of Hydrogen by Cyanobacterial Photosystem I." (http://trace.tennessee.edu/utk_graddiss/982) and shown with permission.

2.1 Introduction

As discussed in Section 1.4.1, hydrogen has the potential to replace traditional fossil fuels due to its ability to be used in fuel cells, its high energy per unit mass, and its potential for carbon neutrality [115-118]. However, unlike fossil fuels molecular hydrogen is not present in great quantities on Earth. While hydrogen can be produced from the steam forming of natural gas, this process releases carbon dioxide into the atmosphere and is ultimately limited by the availability of natural gas. It has previously been demonstrated that platinum nanoparticles can be photo-precipitated onto the reducing side/stromal hump of PSI complexes by photo-precipitation of hexachloroplatinate ($[PtCl_6]^{2-}$) [26, 30, 119, 120], following the reaction: $[PtCl_6]^{2-} + 4e^- + h\nu \rightarrow$

Pt(s) + Cl^-. The platinized complexes are then able to catalyze the photo-production of molecular hydrogen. The platinization reaction is enabled by the same photo-catalyzed reaction for electron transport to reduce protons to hydrogen, by direct electron transfer from PSI to the platinum salt. Therefore, variables that affect the hydrogen production rate (such as temperature, light intensity, and platinum concentration) affect the platinization process.

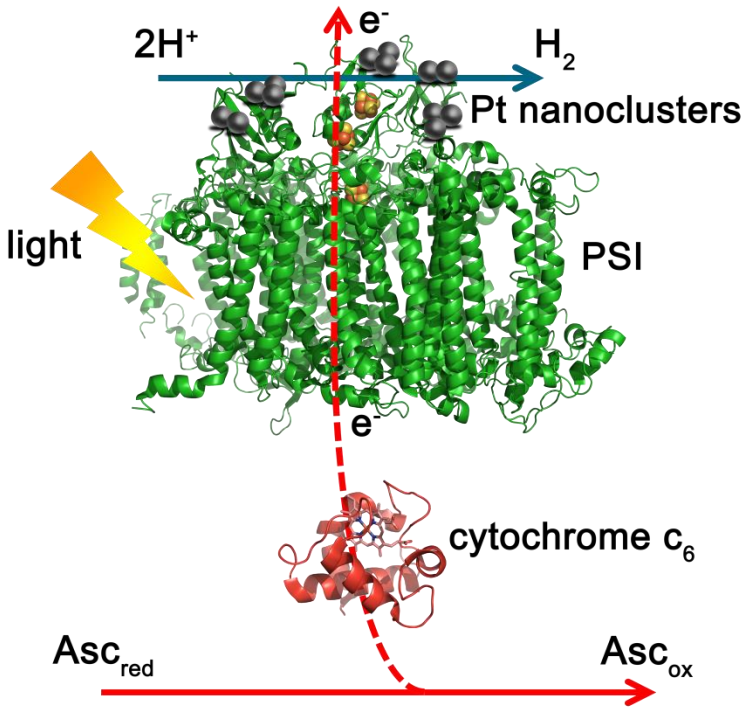

Figure 2.1. Schematic of the platinized PSI system for light-catalyzed hydrogen production with sodium ascorbate as the sacrificial electron donor and cytochrome c_6 as the electron mediator.

In situ platinization and hydrogen evolution was previously demonstrated with trimeric PSI derived from *Thermosynechococcus elongatus* [120], which only utilizes *c*-type cytochrome (cyt c_6) as the primary electron donor to PSI. It has been demonstrated that a platinized PSI system utilizing this cytochrome as the direct electron donor to PSI is capable of evolving H_2 in a cyt c_6- and light-dependent fashion. H_2 was produced at temperatures up to 55°C and was temporally stable for > 85 days. A maximum hydrogen evolution rate of ~5.5 µmol H_2/mg chl

a/h was previously reported for this system [120]. Up to this point, the effect of variables during platinization on the rate of H_2 production has not been investigated. Typically, one variable would be changed at a time, while keeping the other variables constant. This is extremely time consuming and expensive, due to the multiple variables that could be tested. In this chapter, response surface methodology (RSM) was used to efficiently optimize the study of the multiple variables while minimizing the number of experiments required to determine the effect of a variable on the platinization process and hydrogen yield. RSM has been used previously to optimize phototrophic hydrogen production processes [121-124]. For this study, a central composite experimental design was used to determine the individual and interactive effects of the concentration of platinum salt, light intensity and temperature on the platinization process and H_2 evolution of this system. These variables were chosen due to the ease of manipulation.

2.2 Materials and Methods

2.2.1 Growth of *Thermosynechococcus elongatus*

The thermophilic cyanobacterium *T. elongatus BP-1* wild type was grown in a 5 L capacity BIOFLO 3000 Bioreactor (New Brunswick Scientific) in NTA media. The reactor was maintained at 56°C, 300 rpm agitation, 4 L/min air flow, under continuous illumination by fluorescent lights (50 $\mu E/m^2/s$). Cells were harvested during late log phase, OD_{730} ~2.4, by centrifugation for 10 minutes at 7,000 x g, and the cell pellets stored at -80°C until use for PSI isolation.

2.2.2 Isolation of trimeric PSI

Trimeric PSI was purified following a protocol previously established by Fromme et al. [125] with modifications. Frozen cells were thawed on ice and resuspended in 30 mL of

lysozyme buffer (10 mM $CaCl_2$, 10 mM $MgCl_2$, 50 mM HEPES at pH 8.0 and 500 mM sorbitol) and homogenized with a Dounce tissue grinder. The resuspended cell solution was adjusted to chlorophyll *a* (chl *a*) concentration of 1 mg/mL with lysozyme buffer, determined by methanol extraction. A 1:10 dilution of cell suspension in 90% methanol was incubated at 60°C for 2 minutes, then spun at 21,000 x g in a microcentrifuge. 800 µL of the supernatant, while avoiding the pellet, was transferred to a 10 mm pathlength quartz cuvette and the chlorophyll *a* concentration was determined by the equation:

$$\frac{\mu g \text{ chl } a}{mL} = Abs_{665} \times 13.9 \text{ [126]}.$$

Lysozyme powder was then added to a final concentration of 0.25% (w/v) and the mixture was incubated, shielded from light, 37°C with gentle rocking for 1 hour. The mixture was centrifuged for 10 min at 7,000 x g and the supernatant was discarded. The pellet was resuspended in lysis buffer (10 mM $CaCl_2$, 10 mM $MgCl_2$, 20 mM MES at pH 6.4, and 500 mM sorbitol). The volume was adjusted again so that the concentration of chl *a* was 1 mg/mL. 50 µM (final concentration) PMSF protease inhibitor was added before lysis.

The resuspension was passed through a French Press (SLC Aminco) 3 times at a cell pressure of 25,000 psi (1400 on the pressure gauge with the selector set to the high pressure ratio). The flow rate of the lysate was controlled such that the sample exited the cell slowly in a dropwise fashion (2-3 drops per second), and not as a stream. The lysate was centrifuged at 19,000 x g for 30 minutes at 10°C and the highly fluorescent lysate (red/blue color) was supernatant was discarded. The crude membrane fragments collected in the pellet was resuspended in wash buffer (10 mM $CaCl_2$, 10 mM $MgCl_2$, 20 mM MES at pH 6.4) once at the volume determined for 1 mg chl *a*/mL, homogenized with the Dounce homogenizer, and centrifuged at 19,000 x g for 30 minutes at 10°C followed by a resuspension/wash step with half

the volume for 1 mg chl a/mL wash buffer amended with 3 M NaBr, and the balance volume with wash buffer without NaBr, and centrifuged again at 19,000 x g for 30 minutes, 10°C. The membrane fragments were repeatedly resuspended/washed and centrifuged with wash buffer (without NaBr) until the supernatant was no longer fluorescent and clear or only faintly blue in color. The membrane fragment pellet was resuspended/washed one final time in wash buffer, adjusting to the volume for 1 mg chl *a*/mL. n-dodecyl-β-D-maltoside (DDM, 99.5% purity, GLYCON Biochemicals, D97002-C) was added to a final concentration of 0.6% w/v and the mixture was incubated for 30 minutes at room temperature (~20°C) shielded from light, with gentle rocking. The insoluble material was pelleted and separated from the solubilized membrane fraction by centrifugation at 19,000 x g for 30 minutes at 10°C. The supernatant was immediately decanted and loaded onto 10 – 30% sucrose gradients (23 mL total) with a 2 mL 60% sucrose cushion. The sucrose solutions were made by dissolving the sugar in wash buffer containing 0.03% (w/v) DDM. The gradients were poured using a gradient mixer with 21 gauge needles connected to $1/16^{th}$ inch Tygon tubing. The entire apparatus was rinsed with ddH_2O and the pump was calibrated to run at ~4 mL/min sucrose, although this rate may have been adjusted so that the sucrose fell dropwise down the wall of the 32 mL polycarbonate ultracentrifuge tubes (compatible with Beckman SW 28 or SW 32 Ti rotors). Ensuring that the valve between the two chambers of the gradient mixer was in the closed position, 23 mL of the 30% sucrose solution was loaded into the "heavy" chamber, closest to the gradient mixture, and 23 mL of 10% sucrose was loaded into the "light" chamber. A small stir bar was placed into the heavy chamber and allowed to spin as fast as possible without going out of control. The pump was started and after the 30% solution traveled to the tube splitter of the pump, the valve of the gradient mixer was opened so that the 10% and 30% solutions began mixing and the pump was allowed to run until

all of the sucrose had run through. After pouring the gradients, ~5 mL of the soluble membrane fraction was carefully loaded onto the sucrose gradient with a glass Pasteur pipette and bulb, dropwise, allowing the drops to slide down the wall of the tube. Loaded gradients were balanced to an accuracy of ± 0.01 g, using excess sample or 10% sucrose. The gradients were centrifuged overnight (~18 hours) at 24,000 rpm, 10°C.

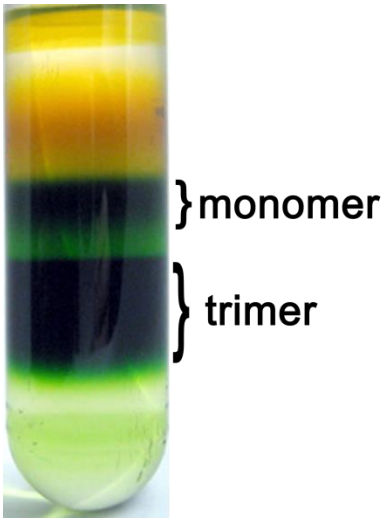

Figure 2.2. Trimeric PSI separation on sucrose gradient.

The lowest green band of the gradient (Figure 2.2) contained the trimeric PSI complex; these bands were pooled using a large blunt-ended syringe. The pooled PSI samples were dialyzed against 20 mM MES pH 6.4, 10 mM $CaCl_2$, 10 mM $MgCl_2$ and 0.03% DDM overnight to remove sucrose, and then loaded onto a POROS 20HQ (Applied Biosystems) anion exchange column (BioCAD 202 Chromatography workstation) and eluted with a non-linear 0 to 400 mM $MgSO_4$ gradient. The method used for the HPLC is shown in Appendix I. The $MgSO_4$ was removed by dialyzing against 20 mM MES pH 6.4, 10 mM $CaCl_2$, 10 mM $MgCl_2$ and 0.03% DDM. The chlorophyll *a* concentration was measured and aliquots were stored at -80°C for future use.

2.2.3 PSI-mediated hydrogen evolution and measurement

Platinization of PSI was performed by incubation of trimeric PSI (50 μg chl *a*/mL), hexachloroplatinate sodium salt ($Na_2[PtCl_6]$), cytochrome c_6, sodium ascorbate and 20 mM pH 6.4 MES buffer in a thermostatically controlled photo-bioreactor as described by Iwuchukwu et al. [120]. The initial screening experiments were carried out with varying concentrations of platinum salt (50 μM, 275 μM, and 500 μM) and varying temperatures (25°C, 35°C, and 45°C). The temperature of the reaction vessel was maintained by an external water bath. The light intensity was also varied during the platinization experiments (120 $\mu E/m^2/s$, 210 $\mu E/m^2/s$, and 300 $\mu E/m^2/s$). All the reaction components were combined, shielded from light exposure, and injected via a needle through a gas-tight septum into the photo-bioreactor, which was also shielded from light. N_2 gas was flowed at a rate of 50 mL/min through the mixture for 30 – 60 minutes to purge air out of the system. After an anaerobic environment was established, the photo-bioreactor was illuminated with focused gooseneck lamps at the intensities above and shielded from external light. A Chrontrol Model XT microprocessor-based timer was used to cycle USHIO 150 W halogen lamps (USHIO INC, Tokyo, Japan) on and off at 2 h intervals. After 24 h of the light catalyzed platinum deposition and hydrogen evolution, the platinized PSI was separated from the reaction by sucrose density gradient centrifugation as described in Section 2.2.2 to remove excess hexachloroplatinate and cyt c_6. The re-isolated platinized PSI formed a pellet at the bottom of the sucrose gradient, which was extracted along with the bottom green PSI layer with a large blunt end syringe. The pellet was homogenized to break up the aggregated PSI-Pt and dialyzed in 20 mM MES buffer pH 6.4. The platinized PSI was reinjected into the reactor for the hydrogen evolution experiment. For the second portion of the experiment (hydrogen evolution), the light intensity and temperature were kept constant for all of the pre-

screening experiments at 280 μE/m^2/s and 35°C, with addition of fresh 10 mM ascorbate as the sacrificial electron donor for light-catalyzed hydrogen production. The rate of hydrogen production was measured in micromoles of hydrogen produced per hour per mg chlorophyll *a* (μmol H_2/mg chl *a*/h). The total (integrated) hydrogen yield for the first 3 cycles was measured for each experiment and used for statistical analysis. Raw data for all experiments are shown in Appendix II.

2.2.4 Screening experiments

Preliminary experiments were carried out to screen the appropriate parameters affecting H_2 yield. During this process, light intensity, platinum salt ($Na_2[PtCl_6]$) concentration and temperature were determined as potentially important factors affecting the rate of H_2 production. The effect of light color (red or white, as described above) during platinization on the H_2 yield was also investigated. It is well-known that high levels and certain wavelengths of light can be damaging to photosynthetic functions. The vast majority of these studies have focused on PSII because it is generally understood to be easily photo-damaged (see [127-129] for reviews of photo-damage and repair in PSII). A study by Takahashi et al. looked at the effects of different wavelengths on PSII and determined that wavelengths around 325 nm (near UV) and 600 nm (yellow) caused the most photo-damage to PSII [130], however this has not be substantiated for PSI. Previous experiments in our laboratory suggested that the use of white light during platinization leads to different hydrogen yields when compared to platinization with red light at similar intensities.

The experimental design for this study was based on a 2^{k-1} fractional factorial design (where *k* is the number of factors) with 4 center points blocked by light color. The values tested and coded levels for the variables considered are shown in Table 2.1. The experiment conditions studied are listed in Table 2.2.

Table 2.1. Level and code for central composite design.

Variables	Symbols	Coded Levels		
		-1	0	+1
Light Intensity ($\mu E/m^2/s$)	X_1	120	210	300
Platinum Concentration (μM)	X_2	50	275	500
Temperature (°C)	X_3	25	35	45

Table 2.2. Fractional factorial design with two center points for white and red light.

Run	Light color	Light Intensity ($\mu E/m^2/s$)	Platinum conc. (μM)	Temp. (°C)	Total yield ($\mu mol\ H_2/mg\ chl\ a/h$)
1	White	120	50	45	0.0565
2	White	120	500	25	2.7849
3	White	300	500	45	0.0979
4	White	300	50	25	0.0886
5	White	210	275	35	2.5578
6	White	210	275	35	2.1938
7	Red	120	50	45	0.0776
8	Red	120	500	25	3.355
9	Red	300	500	45	2.0106
10	Red	300	50	25	4.0594
11	Red	210	275	35	1.5552
12	Red	210	275	35	1.0053

2.2.5 Experimental design and data analysis

Based on the screening experiments, the mean total yield of white light was less than the red light, therefore red light was used for subsequent experiments. Platinum salt ($Na_2[PtCl_6]$) concentration and temperature were selected as independent variables for evaluation in this study. RSM was applied to evaluate the effects of these variables on the rate of H_2 production.

The experimental design was based on a three-factor face-centered central composite design (CCD). Face centered central composite design, a cubic design, contains axial points that are situated at a distance α from the center of the design. The process variables are scaled so that α takes a value of ±1 in the design [131]; an α value of +1 indicates the parameter takes on the value greater than the center point and a value of -1 indicates the parameter is below the center point. A value of 0 denotes the center point value. The total number of experimental points (N) in a central composite design [131] can be calculated by the equation:

$$N = 2^k \text{ (factorial points)} + 2k \text{ (axial points)} + n_0 \text{ (center points)}$$

where N is the number of experimental points, k is the number of independent factors, and n_0 is the number of center points. Therefore the total number of experimental points for this design was 16 (k = 3, n_0 =2). The original experimental design had 16 experimental points; however, one additional point was replicated to offset error estimates. Experiments at the center point were conducted for evaluation of experimental error.

Cumulative H_2 yield was predicted using RSM. JMP version 8 software (SAS Institute Inc., Cary, North Carolina, USA) was used in the experimental design, data analysis, model building, and three-dimensional response surface plot generation. The model was built based on the variables with confidence levels of 95%. Analysis of variance (ANOVA) was performed to evaluate the adequacy of the generated mathematical model.

2.3 Results and Discussion

2.3.1 Screen Experiments

As discussed in Section 2.2.4, an initial screening experiment was done to determine the effect of light color (red or white) on the rate of photo-catalyzed H_2 production. Spectral

irradiance of red light and white light used for the experiment, overlaid with the absorbance PSI in this region are shown in Figure 2.3. The spectral irradiance for the red-filtered light was in the range of 600-850 nm and the spectral irradiance for the white light was in the range of 400-800 nm. The light intensities reported in this experiment were calculated from the integration of only the region between 650 and 750 nm for both white and red light, where the peak absorbance for P_{700} occurs and contains the photosynthetically active wavelengths for PSI excitation. As a result, the light intensity of the white light was considerably higher if the integration of the entire visible spectrum had been used due to the area below 600 nm, when compared to the spectrum for "red" light through a 590 nm long-pass filter, which cuts off wavelengths below 600 nm. It was postulated that the addition of light in the non-photosynthetically active regions, particularly lower wavelength light in the blue region below 500 nm, would increase the rate of photo-damage and therefore decrease the rate of hydrogen production.

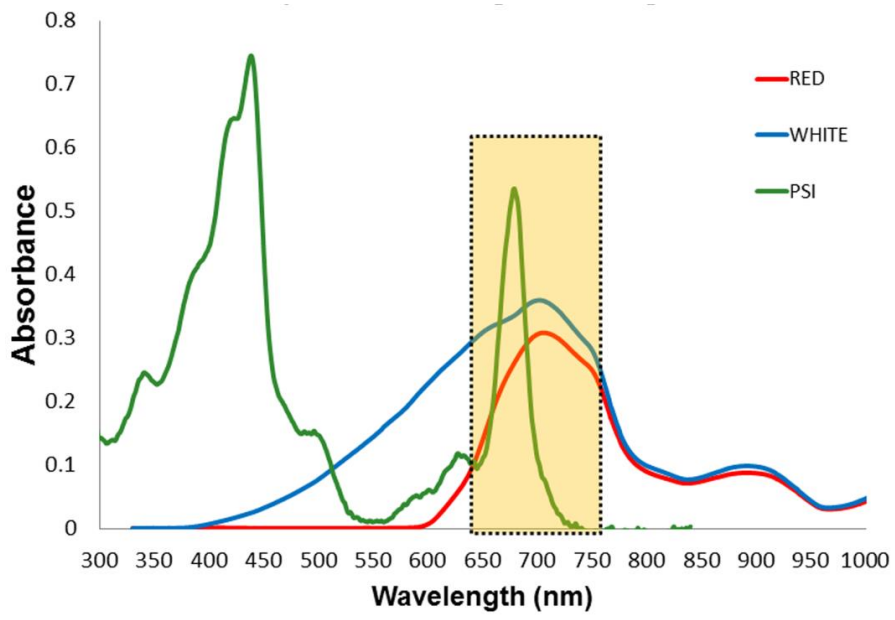

Figure 2.3. Spectral irradiance of red light (red) and white light (blue) shown with the absorbance spectra of PSI (green).

The dependent variables used in this study were: light intensity, platinum salt concentration, and temperature. The highest yield for both the red and white light occurred under the same conditions, 25°C, 120 µE/m^2/s light intensity, and 500 µM platinum salt concentration. The mean total yield for white light (1.297 µmol H_2/mg chl *a*/h) was less than with red light (2.011 µmol H_2/mg chl *a*/h). However, the hydrogen yield during platinization in the red light case is not significantly larger than with white light, which suggests there may not be an advantage in the quality of light provided during the platinization process. This is further evidenced by Figure 2.4, which indicates there is not a preference for light color for platinization step. However, to minimize the amount of resources utilized in this study and to reduce the number of intensive experiments, a single light color was selected for subsequent investigations. Since the prediction profile suggests a minor bias towards red light, the remainder of the study was carried out with red light.

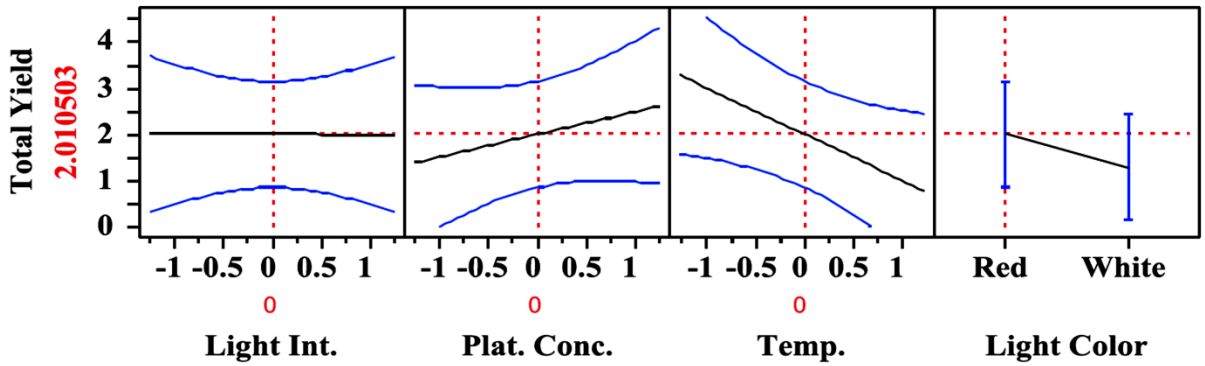

Figure 2.4. Prediction profiler showing effect of white and red light on H_2 yield during platinization.

The predictor also suggests the light intensity does not have a significant effect on hydrogen yield, which is not particularly surprising, because at some light intensity, the system

will become light-saturated and will not increase the platinum salt reduction or hydrogen yield. With increasing platinum salt concentration, the profile indicates that hydrogen yield will also increase. This is a reasonable assumption, because the presence of increased platinum salt would allow for more platinum nanoparticles to be deposited to the reducing side of PSI and therefore more sites to catalyze the reduction of protons to hydrogen. The profiler predicts that increasing temperature has a detrimental effect on hydrogen evolution. This is unexpected, because this study utilizes a thermotolerant PSI, extracted from cells that are typically grown at 55°C. However, this may indicate an issue unrelated to the protein itself, but that at increased temperatures the photocatalytic activity is initially fast, which oxidizes the ascorbate electron donor present and therefore the proton reduction reaction cannot proceed and the system is limited by ascorbate.

2.3.2 Model Fitting

The screening experiments were run in a random order to prevent result bias and effects of uncontrolled variables. The actual and predicted yields from all experimental conditions tested are listed in Table 2.3. Preliminary analysis of the data revealed that the platinum concentration was the most significant variable and impacted the hydrogen yield disparately as the concentration of platinum salt increased. As discussed in Section 2.2.3, the predictor profiler indicated that platinum concentration would likely be the most active variable, however it is unlikely for a saturation bound for the addition of platinum to be determined, since larger particles of platinum could continue to be created with increasing salt concentration, unlike light saturation or reaction limitations caused by temperature or concentration of ascorbate (which was

not studied here). To offset the potentially runaway variable impact of platinum concentration, a natural logarithm was applied to the yield transformation [132].

A model equation was developed to express the transformed total H_2 yield as a function of the independent variables light intensity (X_1^*), platinum salt concentration (X_2^*) and temperature (X_3^*). The raw variables are related to their scaled counterparts such that $X_1=(X_1^*-210)/90$, $X_2=(X_2^*-275)/225$, and $X_3=(X_3^*-35)/10$. The resulting model equation, in terms of the scaled variables, was:

$$\ln(\text{Total } H_2 \text{ yield}) =$$

$$0.2689-0.1173X_1+2.4555X_2+0.5346X_3-0.2593X_1^2-0.8768X_2^2-0.6971X_3^2-0.7321X_2X_3.$$

ANOVA was used to evaluate the significance of the constructed quadratic model and insignificant terms were eliminated. The significance of each coefficient was determined by the t–values and p–values. Detailed data and results for these analyses can be found in Iwuchukwu et al. [10]. From the model equation above, it can be observed that the linear effect, quadratic effect, and interaction effect of light intensity (X_1) did not have significant effects on the model, due to its small and negative coefficient. Therefore, all two-factor light intensity interaction terms were eliminated from the model (X_1*X_2, light intensity-platinum concentration interaction and X_1*X_3, light intensity-temperature interaction) as shown in the model equation above. The analysis also revealed that individually, platinum salt concentration (X_2) and temperature (X_3) had a strong linear effect on the hydrogen yield response. The model shows that platinum concentration ultimately has the largest impact on the hydrogen yield, due to the large coefficient preceding the platinum (X_2) variable.

2.3.3 Analysis of response surfaces

Surface response curves describing the model were constructed to illustrate the effect of the independent variables on the total H_2 yield, by varying two of the variables and holding the third parameter constant at the central point. The effect of light intensity and platinum salt concentration on the total H_2 yield with the temperature fixed at 35°C is shown in Figure 2.5A. At low light intensity, increasing platinum salt concentration increased the total H_2 yield with an inflection point optimum for platinum concentration, after which the yield decreased. Similarly, at high light intensity, increasing platinum salt concentration increased the total H_2 yield. At low platinum salt concentration, increasing the light intensity had minimal effect on the total H_2 yield; this was likely due to platinum salt being the limiting reagent in the formation of the Pt nanoparticles which drives the photo-production of H_2. Increasing the light intensity did not have a significant effect on H_2 yield and this further supports the results presented early that suggested Pt concentration has a significant effect on H_2 compared to the other variables. There was a marginal increase in total H_2 yield up to light intensity of ~230 $\mu E/m^2/s$, observed at high platinum concentration. In general the independent variable, light intensity may indicate the system becomes light saturated at moderate light intensity. The steep slope in the curve on the platinum axis and the red surface response at high platinum concentration suggests platinum salt had a significant effect on the system.

Figure 2.5B illustrates the effect of light intensity and temperature on the total H_2 yield. At both low and high temperatures, increasing the light intensity had a less pronounced effect on the total H_2 yield than the effect of platinum noted above. Similarly, at low and high light intensities, changing the temperature had a less pronounced effect on the total H_2 yield. This result suggests that the interactive effect of light intensity and temperature on the total H_2 yield

was not significant, allowing the interaction term to be eliminated from the model equation. On the temperature axis, looking at the variable individually, the red surface response suggests there is an optimal temperature during the platinization process between 35°C and 40°C. Figure 2.5C shows the effect of platinum salt concentration and temperature, the two variables that carry the most weight in the model equation. At low platinum salt concentration, the total H_2 yield increased with increasing temperature. At high platinum salt concentration, increasing the temperature generally had a negative effect on the total H_2 yield. PSI was isolated from a thermophillic organism and increasing the temperature increases the rate of electron transfer [120] and therefore the formation of the Pt nanoparticles. At high platinum concentration, increasing temperature probably results in the formation of large platinum clusters which suggests that there may be an optimum size for the platinum clusters. At low temperature, increasing the platinum salt concentration increases the H_2 yield, while at the highest temperature, there is an optimum platinum concentration, with a significant decrease in rate on either side of the optimum value. Figure 2.5C shows that these two variables were interdependent and there was significant interactive effect between temperature and platinum salt concentration on the H_2 yield, unlike the interactions of light intensity with both temperature and salt concentration. This surface response plot suggests that the optimal hydrogen yield is likely to occur at moderate temperatures and high platinum salt concentration. Other factors that were not considered in this study such as PSI concentration, PSI/cyt c_6 ratio, ascorbate concentration, illumination time with respect to platinization and hydrogen evolution, and pH may also have an effect on the total H_2 yield. Therefore, further investigation is required to evaluate the effect of these variables on the total H_2 yield and to advance the optimization of hydrogen evolution for this system.

The prediction profiler that integrated the results of all of the screening experiments is shown in Figure 2.6. Like the contour plots of Figure 2.5A-C, it shows light intensity has little effect on H_2 yield. Conversely, platinum salt concentration has a significant effect on H_2 yield as indicated by the steep curve, where the optimal concentration lies between $X_2 = 1 – 1.5$, where +1 corresponds to a value of 500 µM and +1.5 corresponds to 725 µM and there is an optimal value within that range. Beyond the inflection point, the profile for platinum concentration suggests H_2 yield will decrease in the presence of excessive platinum and as expected, at low platinum salt concentrations the yield is likely low due to minimal catalyst surface available for proton reduction. The profile for the effect of temperature indicates the optimal temperature for H_2 yield lies between 25°C and 35°C and may have an effect on yield, though not as significant as platinum salt concentration. The profile also suggests temperatures above 35°C have a slight negative effect on hydrogen yield.

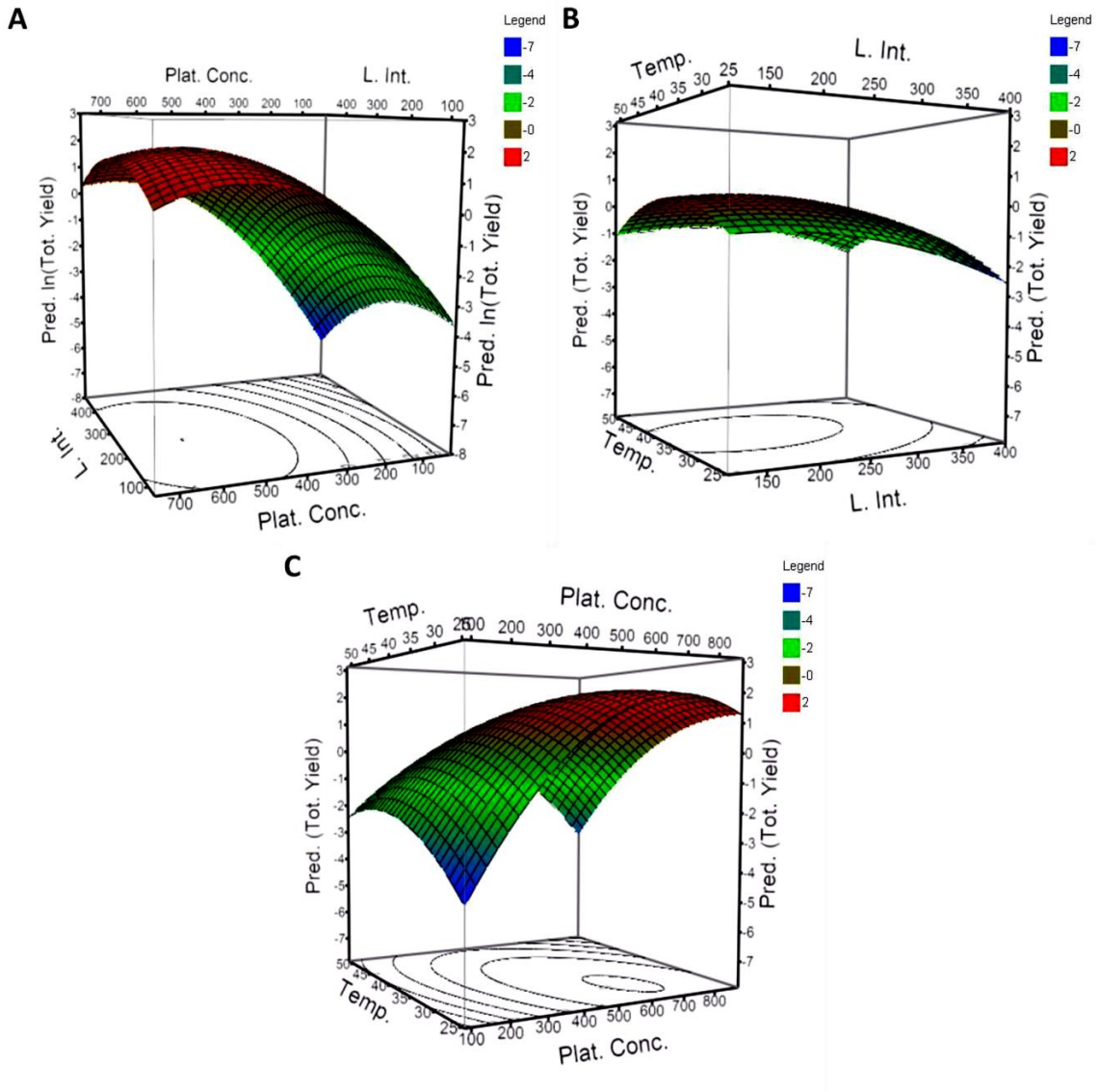

Figure 2.5. Response surface and contour plots on the combined effects of independent variables on the total H_2 yield. A) Light intensity and platinum salt concentration, temperature constant. B) Light intensity and temperature, platinum salt concentration constant. C) Platinum salt concentration and temperature, light intensity constant. The scales on the y-axes are the natural log of the predicted yield.

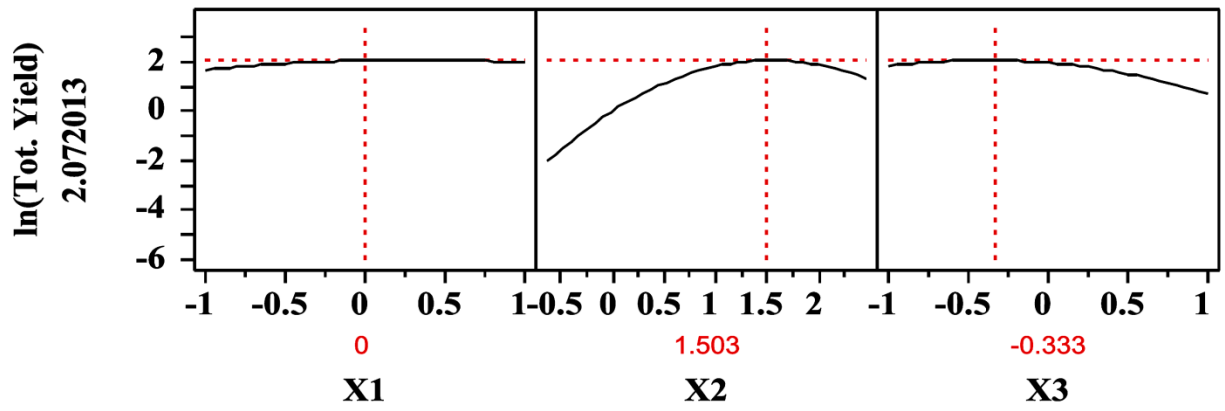

Figure 2.6. Prediction profiler for the different variables incorporating screen experiment results. Light intensity (X_1), platinum salt concentration (X_2), and temperature (X_3).

2.3.4 Optimization and validation of model

Using the fitted model equation to optimize the variable settings to maximize hydrogen yield shows that the optimal values are outside the range of the data tested. However, visual inspection of the surface contour plots in Figure 2.5 show that H_2 yield is likely optimized at the inflection points of 240 μE/m^2/s light intensity, 638 μM platinum, and 31°C temperature. The model predicted the optimum H_2 yield was ~8.17 μmol H_2/mg chl *a*/h. An additional experiment was performed to verify the predicted yield by platinizing PSI under the conditions listed above. The hydrogen yield phase was performed at the same constant conditions as all of the previous experiments (280 μE/m^2/s light intensity and 35°C). The experimental value for the validation experiment was 8.02 μmol H_2/mg chl a/h (Figure 2.7) a value higher than any found in the earlier experiments used to derive the model.

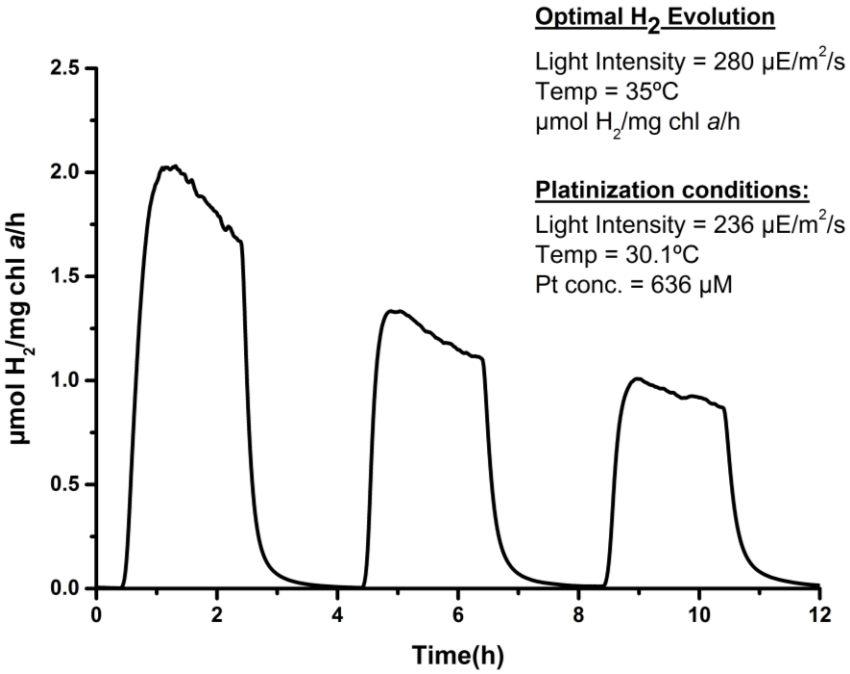

Figure 2.7. Hydrogen evolution under the optimum condition. (Light intensity of 240 µE/m^2/s, platinum salt concentration of 636 µM and temperature of 31°C).

2.4 Conclusion

This was the first study to investigate the effects of light intensity, platinum salt concentrations, and temperature during the platinization process for photo-dependent H_2 production and the subsequent hydrogen yield from platinized PSI particles. Fraction factorial design was used to screen a series of experiments to determine the effect of light quality (white vs. red) on the rate of H_2 production. The mean total yield using red light during platinization was marginally higher than the yield for white light. Application of RSM to the full central-composite design showed that a second-order polynomial model for light intensity, platinum salt concentrations and temperature during platinization could be used to optimize H_2 yield in photo-catalyzed Pt-PSI hydrogen evolving systems. Platinum salt concentration, temperature and the interaction between platinum salt concentration and temperature during platinization showed significant effects on the total H_2 yield. Light intensity during platinization had a minimal effect

of the total H_2 yield within the region studied. The optimum parameters for H_2 photo-production were at light intensity of 240 μE/m^2/s, platinum salt concentration of 638 μM, and temperature of 31°C during the platinization process. Response surface methodology (RSM) was an effective technique for analyzing and optimizing the photo-dependent H_2 production utilizing platinized-PSI particles and the experimental design to determine optimal parameters was successful in reducing resources used and time necessary to study these conditions.

3. ANALYSIS OF THE SOLUTION STRUCTURE OF *THERMOSYNECHOCOCCUS ELONGATUS* PHOTOSYSTEM I IN *N*-DODECYL-*B*-D-MALTOSIDE USING SMALL-ANGLE NEUTRON SCATTERING AND MOLECULAR DYNAMICS SIMULATION

A version of this chapter was originally published by Le et al.:

Le, R. K.; Harris, B. J.; Iwuchukwu, I. J.; Bruce, B. D.; Cheng, X.; Qian, S.; Heller, W. T.; O'Neill, H.; Frymier, P. D., Analysis of the solution structure of *Thermosynechococcus elongatus* photosystem I in n-dodecyl-β-d-maltoside using small-angle neutron scattering and molecular dynamics simulation. Archives of Biochemistry and Biophysics 2014, 550–551 (0), 50-57. (http://www.sciencedirect.com/science/article/pii/S0003986114001350)

All figures presented in this chapter have previously appeared in the reference above. All DAMMIF reconstruction files of PSI in DDM were created by Bradley Harris (BH). Figure 3.3 was created using data generated by BH and is shown with permission by the author.

3.1 Introduction

We initially set out to use small-angle neutron scattering (SANS) to visualize the localization of platinum nanoparticles on PSI. The simplified schematic of platinized PSI (Figure 2.1 of Chapter 2) typically shows Pt clusters on the stromal hump of the protein, however it is still unknown if this depiction is accurate. Furthermore, we wanted to characterize the size of the resulting particles under different platinization conditions to determine the optimal distribution and size of particles for enhanced photo-catalyzed hydrogen production. Previous attempts to characterize the Pt-PSI samples using SEM and TEM were unsuccessful and showed that microscopy could not resolve the complex. These 2D Pt-PSI samples (protein on solid support surface) caused aggregation, therefore SANS (3D solution structure) was pursued. Pt-PSI samples precipitated/aggregated with the addition of D_2O. Additional *n*-dodecyl-*β*-D-maltoside (DDM) detergent had to be added above the typical concentration used for our previous PSI

studies (0.03% wt/vol) to prevent aggregation. Therefore we sought to understand how DDM oriented itself around a PSI trimer since PSI-detergent interactions may have a significant role when integrating PSI into fusions with other proteins or with surfaces, as the presence of detergent could change surface density or prevent the protein from getting close to other surfaces. The Pt-PSI samples were too aggregated to study, consequently pursuing further characterization did not seem like an avenue worth continuing and PSI-DDM samples, without platinum were studied.

Since PSI is a large multi-subunit membrane complex its isolation requires the use of non-ionic detergents such as Triton X-100, *n*-octyl-*β*-D-glucoside, *n*-dodecyl-*β*-D-maltoside, or a combination of them. These detergents both disrupt the membrane and solubilize the membrane complexes in mixed micelles that prevent aggregation and mimic its native membrane-like environment. Though detergents allow membrane complexes to be soluble in aqueous solution, their abundance and non-native characteristics can interfere with the ability to study protein-protein interactions and/or structural and functional properties [60, 92, 93]. The difficulties associated with solubilizing and stabilizing membrane proteins like PSI are due primarily to the exposure of its hydrophobic domains, which are protected by the lipid bilayer in the native environment. Therefore it is necessary to understand the effects of detergents used for membrane protein studies, as it has been shown that short alkyl chain detergents are more effective at solubilization than long alkyl chain detergents, which can cause protein denaturation [94, 95]. Furthermore, it is important to understand the impact of detergent micelles on membrane proteins in solution, particularly the protein-detergent interactions that affect protein conformation or cause aggregation. Recent studies [60, 96] have shown that the critical micelle concentration (CMC) and critical solubilization concentration (CSC) are of particular importance

for determining how effective a detergent is at solubilizing a membrane protein. Both parameters have been studied for various detergents, such as *n*-dodecyl-*β*-D-maltoside (DDM) which was used in this study.

Our interest in understanding the interaction of detergent with cyanobacterial PSI stems from its ability to undergo charge separation for unidirectional electron transfer upon exposure to light, which can be integrated into bio-hybrid solid-state electronic devices for electricity [49, 58, 66, 67, 133] or hydrogen [11, 32, 33, 46, 134, 135] production. As these technologies have great potential in the field of energy conversion, it is important to develop robust, reproducible techniques to uniformly orient PSI molecules on conductive substrates or in complexes with other proteins. Knowledge of the protein–detergent interactions is important for retaining protein activity and preventing denaturing environments for studying protein function *in vitro* [136] as well as addressing issues related to solution-phase aggregation which could impact the oriented assembly of PSI at a surface.

Small-angle neutron scattering (SANS) is very useful for probing structural properties of biological complexes [137]. By varying the ratio of H_2O and D_2O in solution, which have distinct scattering length densities [138], it is possible to match the background scattering to one component of the complex, effectively masking it and allowing a view of the remaining portions of the complex without disturbing the complex. There have been many different applications of contrast matching methods, ranging from block copolymers [139, 140] and self-assembled materials [141] to biological systems [142-144]. The naturally occurring differences in scattering length densities of protein and other molecules makes SANS with the contrast matching an excellent tool for such studies [145, 146].

Molecular dynamics (MD) simulation is a valuable tool for interpreting neutron scattering data. It has been widely used to investigate polymer systems [147, 148], chemical reactions [149-151], and biological systems [149-158]. Additionally, the simulations can be used to generate simulated scattering curves for comparison against experimental SANS data. This allows a greater understanding of the interactions between protein and detergent, and the structure of the overall complex. For example, Scott et al. demonstrated that MD models of membrane proteins, such as PSI, require additional bilayer lipid molecules beyond those defined in the crystal structure to maintain the native structure [159].

We combined neutron scattering and MD simulations to study the interaction of PSI from *T. elongatus* with DDM in solution to improve our understanding of how the complex is solubilized by the detergent. The results from MD simulations were compared to scattering from protein-detergent complexes with and without detergent contrast-matching, providing detailed structural information on the protein-detergent complex. The results indicate that the detergent belt around the PSI transmembrane domains is not consistent with a uniform toroidal structure, as previously suggested [96]. Instead, the monolayer of DDM molecules adopts a clover-like envelope around the PSI trimer shape. The structural insight gained not only improves the broader understanding of membrane protein-detergent interactions, but will also guide strategies for incorporating PSI into energy harvesting devices. The MD simulation portion of the SANS work was performed by Bradley Harris and the details of this contribution have been excluded from this chapter but can found in the reference at the beginning of this chapter.

3.2 Materials and Methods

3.2.1 Isolation and purification of trimeric PSI from T. elongatus

PSI trimers used in this study were obtained from *T. elongatus BP-1* [160]. Cells were grown as described in Section 2.2.1. Trimers were generated from frozen cell pellets as described in Section 2.2.2. Previous transmission electron microscopy (TEM) of the complexes purified in this manner also confirmed the uniformity and purity of the trimeric PSI nanoparticles [31]. The chl *a* concentration of the PSI trimer used was 0.59 mg/mL and 0.64 mg/mL in the 18% D_2O and 100% D_2O samples respectively.

3.2.2 Analytical Procedures

The concentration of chlorophyll *a* present in the samples was determined by Eq. 1:

$$\frac{\mu g \text{ chl a}}{mL} = Abs_{665} \times 13.9 \quad (1)$$

as in Hall, 1999 [161]. The trimer concentration was approximated by stoichiometric conversion with conversion factors: 893 g chl *a* per mol chl *a*, 96 mol chl *a* per mol P_{700}, and 3 mol P_{700} per mol trimer.

3.2.3 Small-Angle Neutron Scattering

SANS experiments were performed at the Bio-SANS beamline [162] located at the High Flux Isotope Reactor (HFIR) of the Oak Ridge National Laboratory. Samples were measured at 20°C, in 1 mm path length quartz cells (Hellma U.S.A., Plainview, NY). Scattered neutrons were collected with a 1 m by 1 m two-dimensional (2D) position-sensitive detector with 192 by 192 pixel resolution (ORDELA, Inc, Oak Ridge, TN). The 2D data were corrected for detector pixel sensitivity, as well as the dark current, from ambient background radiation and the detector's

electronic noise. The 2D reduced data were azimuthally averaged to yield the 1D scattering intensity I(q) vs. q, where q is described by Eq. 2:

$$q = \frac{4\pi\sin(\theta)}{\lambda} \quad (2)$$

and 2θ is the scattering angle from the incident beam and λ is the neutron wavelength (6Å, Δλ/λ, ≈ 0.15%). SANS data were taken at sample-to-detector distances of 1.1 m, 6.8 m, and 15.3 m for each sample to cover the expected q-range. The 1D profiles from different detector distances were merged to produce a complete scattering intensity plot.

PSI in 0.12% DDM was measured in 18% D_2O buffer, the contrast match point for the detergent [163], and in 100% D_2O buffer. Additionally, a PSI-free DDM solution at 0.12% (w/v) was measured in 100% D_2O. The corresponding buffers with DDM were also measured for background correction for the PSI-containing samples. The radius of gyration (R_g) was determined from the Guinier region of the SANS data with the Guinier approximation [81], Eq. 3:

$$I(q) = I(0)e^{\frac{q^2R_g^2}{3}} \quad (3)$$

where I(0) is the forward scattering intensity, a shape-independent function of the total scattering power of the sample. A linear fit of ln(I(q)) vs. q^2 (a Guinier plot) provides I(0) and R_g from the y-intercept and slope, respectively [82]. The data were processed using the program package PRIMUS [164].

3.3 Results and Discussion

3.3.1 SANS Analysis of DDM Micelles

SANS measurements were performed to characterize the DDM micelles in the absence of PSI. The SANS data P(r) derived from it are shown in Figure 3.1A and Figure 3.1D (red curve),

respectively. The radius of gyration, R_g, of the DDM micelles in 100% D_2O was determined to be 2.04 ± 0.30 nm by the Guinier approximation (Figure 3.2A) and 2.03 ± 0.02 nm from the P(r) fitting (Table 3.1). This result is consistent with the value of 2.01 nm determined by Abel et al.[165] The fully extended length of a DDM molecule is ~2.3 – 2.8 nm, determined by Auer et al. [166], suggesting a reasonable micellar structure. The value of D_{max} from the GNOM fit is 6.4 nm, which is greater than twice this length and the P(r) is not symmetric, indicating that the micelles are not spherical. Using the gyration radius of 2.6 nm to determine the approximate surface area of a spherical DDM micelle (84.9 nm^2) and assuming a DDM monomer head has the projected area of an ellipse (0.63 nm^2, with a = 1.05 nm and b = 0.76 nm measured in PyMOL [167]) for dense hexagonal-packed headgroups ($\eta = \frac{\pi}{2\sqrt{3}}$) yields an aggregation number of ~122 DDM molecules. Our measured aggregation number for the DDM micelles is consistent with previously reported values [168-173]. This aggregation number yields a micelle concentration of 1.79 x 10^{-2} mM (2.18 mM DDM in micelles) calculated from Eq. 4:

$$[\text{total detergent}] = [\text{monomer}] + [\text{micelles}] \times AN_{DDM} \qquad (4)$$

where [total detergent] = 2.35 mM DDM, [monomer] = [CMC] = 0.17 mM DDM, and AN_{DDM} = 122 monomers per micelle.

3.3.2 SANS Analysis of PSI

The SANS data collected for the PSI-DDM sample in 18% D_2O, the contrast match point for DDM, are shown in Figure 3.1B and represent the scattering profile of PSI alone. The P(r) is shown in Figure 3.1D. The R_g of PSI/DDM in 18% D_2O, presented in Table 3.1, are 7.79 ± 2.86 nm from Guinier analysis (Figure 3.2B) and 7.59 ± 0.09 nm from P(r) fitting, and agree well with each other. The P(r) curve has an asymmetric shape similar to those previously reported for

membrane proteins [85, 86]. It has a peak at 8.6 nm and trails to a maximum particle size, D_{max} of 21.5 nm ± 1.0, suggesting a disk-shaped structure [92, 174, 175]. These dimensions are in good agreement with the crystal structure trimer (PDB ID: 1JB0).

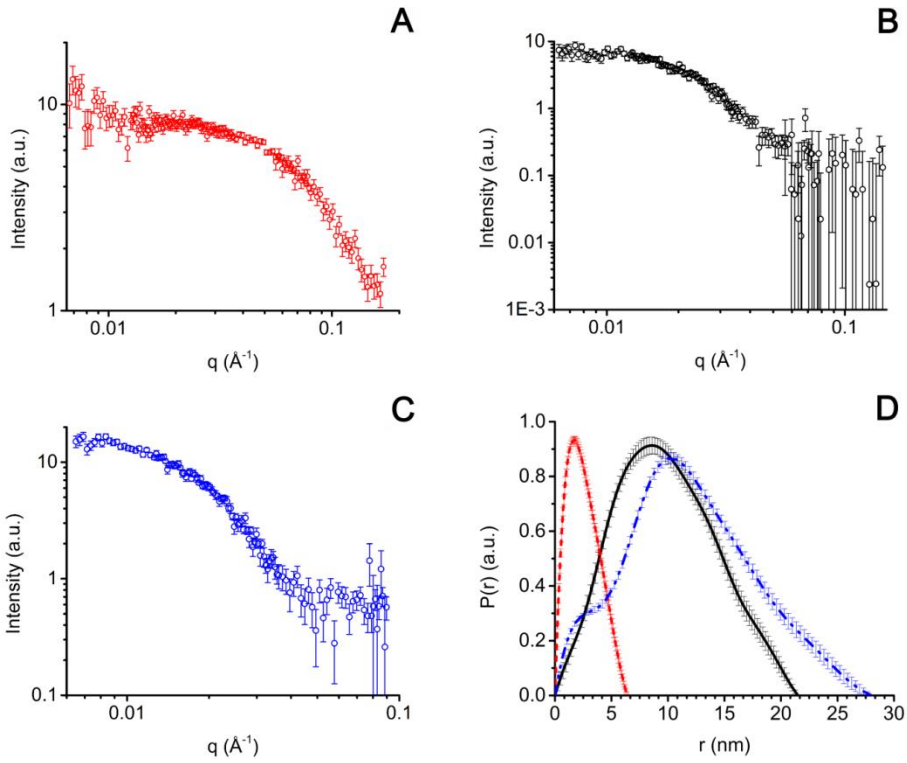

Figure 3.1. Experimental scattering and particle distance distribution functions of SANS samples. (A) 0.12% DDM in 100% D_2O. (B) 0.12% DDM and PSI in 18% D_2O. (C) PSI in 100% D_2O. (D) P(r) of 0.12% (w/v) DDM in 100% D_2O (red curve), PSI with 0.12% (w/v) DDM in 18% D_2O (black curve), and PSI with 0.12% (w/v) DDM in 100% D_2O (blue curve) generated with GNOM.

Table 3.1. Structural parameters of DDM micelles in 100% D_2O and PSI in 0.12% (w/v) DDM in 18% and 100% D_2O from SANS measurements. Calculated parameter values are shown as the mean value plus/minus the standard error of the mean of Rg.

Sample	**[D_2O] (%)**	**[PSI trimer] (mM)**	**[DDM] (mM)**	**Guinier R_g (nm)**	**P(r) R_g (nm)**	**D_{max} (nm)**
DDM only	100%	0	2.35	2.04 ± 0.30	2.03 ± 0.02	6.4 ± 0.5
PSI+DDM	18%	2.27 x 10^{-3}	2.35	7.79 ± 2.86	7.59 ± 0.09	21.5 ± 1.0
PSI+DDM	100%	2.48 x 10^{-3}	2.35	9.49 ± 2.32	9.31 ± 0.11	28.0 ± 1.0

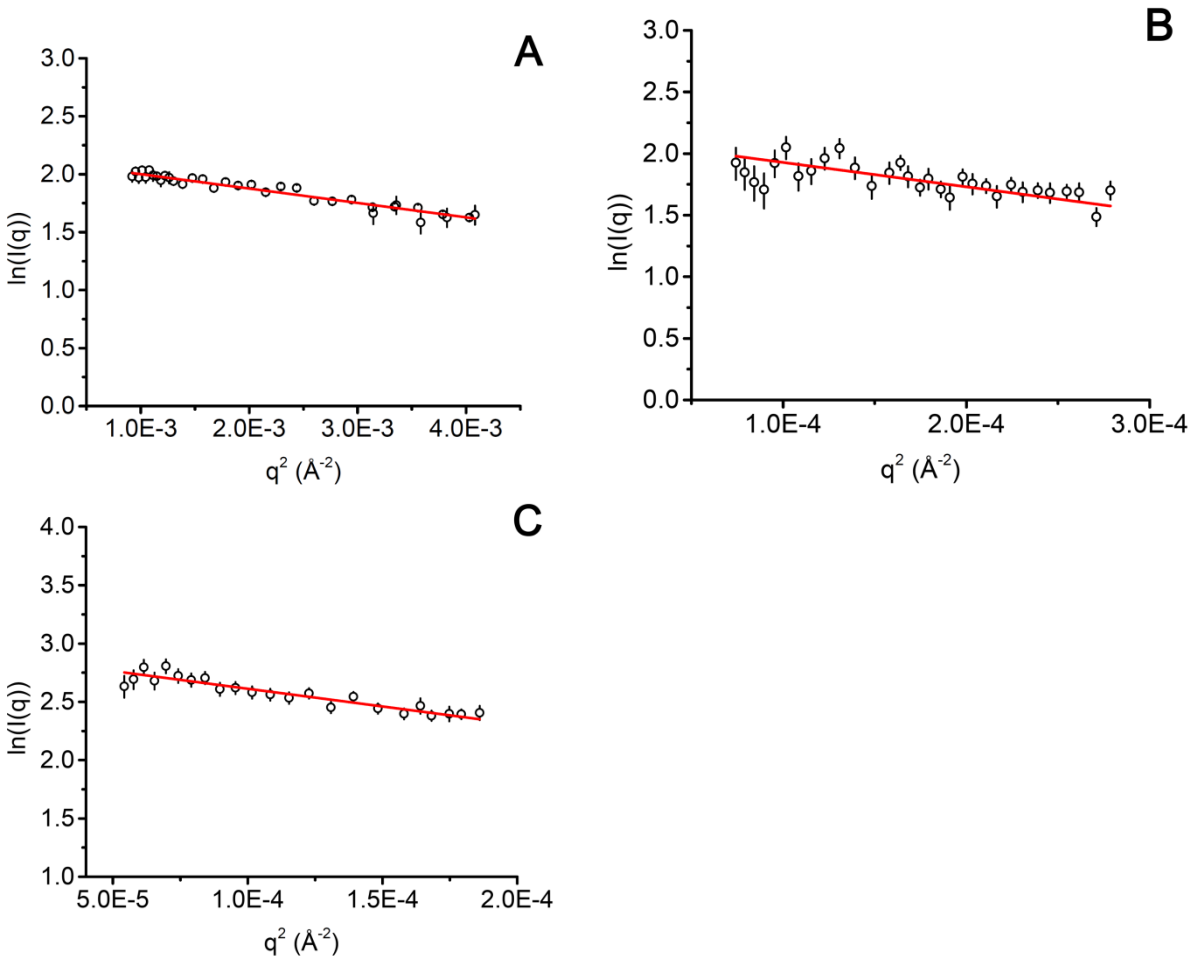

Figure 3.2. Guinier analysis of (A) 0.12% (w/v) DDM in 100% D_2O, (B) PSI with 0.12% (w/v) DDM in 18% D_2O, (C) PSI with 0.12% (w/v) DDM in 100% D_2O shown with linear fits in the respective experimental scattering in the low-q regime with qR_g <1.3. All plots are shown with the standard error associated with each point of the respective samples. See Table 3.1 for the resulting R_g values and associated error.

3.3.3 Interaction of PSI and DDM

The structure of the PSI-DDM complexes and the interactions between the two components of the mixture were probed by collecting scattering data for PSI with 0.12% (w/v) DDM in 100% D_2O, which is shown in Figure 3.1C. At 100% D_2O there is maximum contrast between both PSI and DDM and the solvent and scattering results from both protein and detergent. The R_g of the protein-detergent complexes was determined by Guinier analysis

(Figure 3.2C) of the experimental scattering and by using the program GNOM, yielding R_g values of 9.49 ± 2.32 nm and 9.31 ± 0.11 nm, respectively. The P(r) curve has an asymmetric parabolic shape and peak at 10.1 nm that tapers off at longer distances, which is suggestive of a disk-like structure [92, 176], a D_{max} of 28.0 ± 1.0 nm, and a shoulder feature at short vector lengths below 5 nm. In Table 1, the R_g value for PSI in 0.12% (w/v) DDM and 100% D_2O as determined by both Guinier analysis (9.49 ± 2.32 nm) and P(r) analysis (9.31 ± 0.11 nm) is larger than the value of a 7.7 nm in the DDM contrast-matched sample at 18% D_2O. A change in the D_{max} from PSI/DDM at 18% and 100% D_2O by 6.5 nm from P(r) is slightly larger than the expected size change for twice the fully extended length of a DDM molecule, approximately 5 nm. These values support the existence of detergent around the periphery of the trimer, surrounding the trans-membrane alpha-helixes that have also been seen in other studies [96, 177-181].

The aggregation number for the PSI/DDM complex was estimated by assuming the complex is roughly a squat cylinder (made up of two concentric cylinders, the inner of which is PSI and the outer is a toroidal band of DDM) and that the DDM exists with the hydrophilic head groups closed packed on the periphery of the cylinder. The geometry of the cylinder was determined using the radius (13 nm) calculated from R_g of the PSI-DDM complex and a height excluding the stromal hump of 6.7 nm (height of the crystal structure of the PSI trimer transmembrane-spanning domain as measured by PyMOL). These radius and height values were used to calculate the approximate surface area of the periphery of a cylindrical PSI trimer-DDM complex (547 nm^2). The number of DDM monomer "heads" around the complex was determined by assuming a DDM monomer head has the projected area of an ellipse of 0.63 nm^2 (with axes of 1.05 nm and 0.76 nm as measured in PyMOL). It was further assumed that the monomer

heads are packed in a dense hexagonal pattern around the periphery of the cylindrical complex ($\eta = \frac{\pi}{2\sqrt{3}}$). This procedure yields an aggregation number of ~792 DDM molecules per PSI trimer. The concentration of micelles was calculated using Eq. 5:

$$[\text{total detergent}] = [\text{monomer}] + [\text{PSI}] \times AN_{DDM\text{-}PSI} + [\text{micelles}] \times AN_{DDM} \quad (5)$$

where [total detergent] = 2.35 mM DDM, [monomer] = [CMC] = 0.17 mM DDM, [PSI] = 2.48 x 10^{-3} mM PSI trimer, $AN_{DDM\text{-}PSI}$ = 792 DDM monomers per trimer, and AN_{DDM} = 122 monomers per micelle. The resulting concentration of DDM complexed with PSI ([PSI] x $AN_{DDM\text{-}PSI}$) is 1.95 mM and that of detergent molecules in micelles ([micelles] x AN_{DDM}) is 0.23 mM. This yields a free micelle concentration of 1.85 x 10^{-3} mM. The free micelle concentration in the PSI-DDM sample was therefore about 10% of that in the DDM-only sample (1.79 x 10^{-2} mM free micelles). The resulting distribution of DDM monomer is 83% associated with PSI trimers, 10% in micelles, and 7% in non-associated monomer. For this reason, we used a monodisperse arbitrary particle model for calculating the distribution P(r) and, in the following simulations, modeled only the PSI/DDM complexes. This effectively assumes that the scattering due to the DDM micelles is negligible relative to that of the PSI/DDM complexes.

To visualize the structure of PSI in DDM, shape restoration was performed using DAMMIF from the SANS data for $q \leq 0.1$ Å^{-1}. The superposition of the average structure at 18% D_2O with the crystal structure can be seen in Figures 3.3A-C. The reconstruction of PSI-DDM at 18% (green) appears to be slightly larger than the crystal structure (blue) due to the selected representation, but its D_{max} is ~22 nm, which is consistent with the expected diameter from the crystal structure. The reconstruction from the SANS data of the PSI-DDM complex in 100% D_2O (black) shown in Figures 3.3D-F overlaid with the model reconstructed from the SANS data collected in 18% D_2O (green) show where the DDM is found around the PSI structure. The

models indicate that DDM exists primarily as a non-uniform envelope about the periphery of the trimer. The overall structure of the PSI-DDM complex provided by the reconstruction indicates that the DDM is localized around the periphery of the PSI (visible prominently in Figures 3.3D-F) at each PSI monomer lobe and fills interstitial spaces between the monomers. There is no detergent on the stromal and lumenal surfaces, as can be seen in Figures 3.3D-F. Examination of the surface characteristics of the stromal and lumenal surfaces of the crystal structure using VMD shows no significant hydrophobic patches on these surfaces, consistent with minimal coverage of detergent there. Examination of the transmembrane regions of the trimeric crystal structure revealed a uniform distribution of hydrophobic alpha-helices around the periphery of the complex, which is consistent with the distribution of detergent molecules within the interstitial spaces of the monomers and on the exposed outer surfaces.

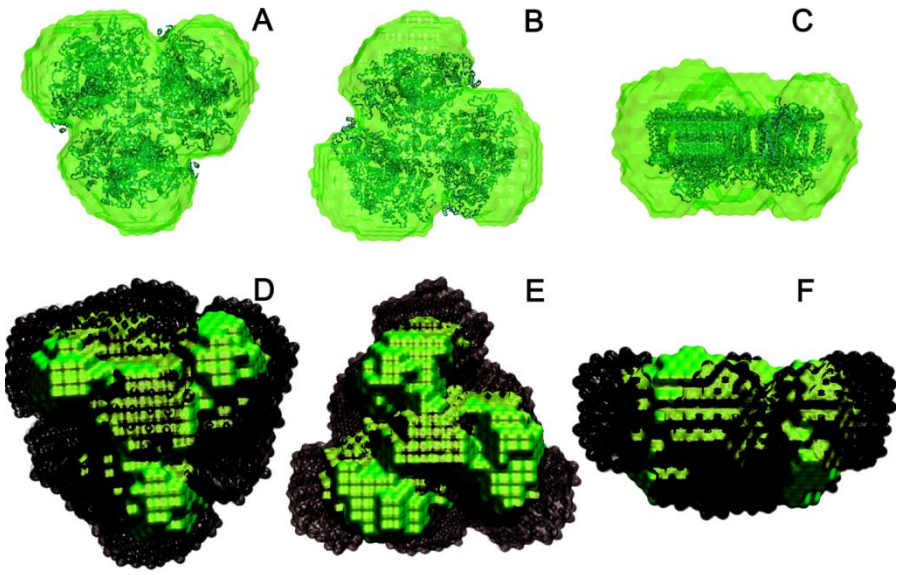

Figure 3.3. Dummy-atom reconstruction of PSI trimer with DDM in 18% and 100% D_2O buffer using DAMMIF. (A), (B), (C) Stromal side up, lumenal side up, and side views of the trimeric crystal structure (blue) superimposed with the reconstruction of PSI-DDM at 18% D_2O (green), respectively. (D), (E), (F) Stromal side up, lumenal side up, and side views of PSI-DDM at 18% D_2O reconstruction (green) superimposed with PSI-DDM at 100% D_2O reconstruction (black), respectively.

3.4 Conclusion

The solution structure of detergent-associated PSI preparations was investigated by SANS analysis and produced results that have not been seen previously. Analysis of the data with and without the scattering contribution of DDM suggests that the detergent exists primarily as a belt surrounding the transmembrane domains of the protein complex with no interaction with the stromal and lumenal surfaces. This study provides important insights into properties of PSI from the thermophile *T. elongatus* in solution with detergent that can be utilized in designing solutions possessing minimal aggregation for energy converting applications that could lead to enhanced operation and longer useful lifetimes. Additionally, the results provide new information about how detergent surrounds membrane proteins, which will be crucial for understanding how these detergent/protein complexes can interact with other proteins or surfaces to form conjugate structures for energy applications, such as protein fusions or surface attachments [58, 64, 66, 133]. The often-seen schematics of membrane proteins suspended in solution within a uniform detergent structure are an idealization and oversimplification, as the results presented here demonstrate.

4. SORTASE-MEDIATED LIGATION OF PSAE-MODIFIED PHOTOSYSTEM I FROM *SYNECHOCYSTIS* SP. PCC 6803 TO A CONDUCTIVE SURFACE FOR ENHANCED PHOTOCURRENT PRODUCTION ON A GOLD ELECTRODE

4.1 Introduction

Due to the inability to fully characterize the solution structure of platinum nanoparticles of the platinized PSI particles, the advancements made in hydrogen yield observed in PSI-hydrogenase fusions, and the transition from hydrogen technologies to electrification to align our research efforts with the goals of the current energy economy, we began optimizing a PSI-conductive surface system for photo-catalyzed current production. Studying PSI attached to solid supports allows for an alternative approach for studying the electron transfer behavior of photo-catalyzed reactions involving PSI. In recent years, exploration of bio-based photovoltaic technology utilizing photosynthetic reaction centers has become popular in the renewable energy field and may prove to be a viable, inexpensive, and easily maintained alternative to current traditional photovoltaics. As discussed in Section 1.4.2, the robust nature coupled with its high photon-electron conversion efficiency of PSI has led to many studies integrating PSI onto solid substrates for alternative energy applications. Current efforts have shown that PSI can be attached to conductive materials via self-assembled monolayers (SAMs) [57, 60, 61, 64, 182-184], covalently linked to gold by targeting cysteine residues of the protein complex [53], or deposited via vacuum [58] or electric field [59] assist. Though these methods are effective for depositing PSI on surfaces, the orientation is generally unknown and likely mixed. Modeling has shown that at least 90% of the complexes must be oriented in the same orientation to achieve useful current density and when 20 – 80% of the PSI complexes are uniformly oriented the competing directionalities of electron transfer result in relatively small net photocurrents [8]. Figure 4.1 shows the electron transport pathway for electrons between PSI and a conductive surface. Regardless of the desired path, the orientation of PSIs should be identical to prevent electron transfer events from canceling each other out.

To overcome the limited current densities in monolayers due to lack of protein orientation, sortase-mediated ligation (SML) was used to attach the PSI complex from *Synechocystis* sp. PCC 6803 in a desired orientation to enhance electron transfer to a conductive gold surface to convert solar energy into electrical energy. Sortase A (srt A) enzyme from *Staphylococcus aureus* was used in this chapter to aid in the coupling of PSI to a tri-glycine peptide decorated gold surface (schematic of reaction shown in Figure 4.2).

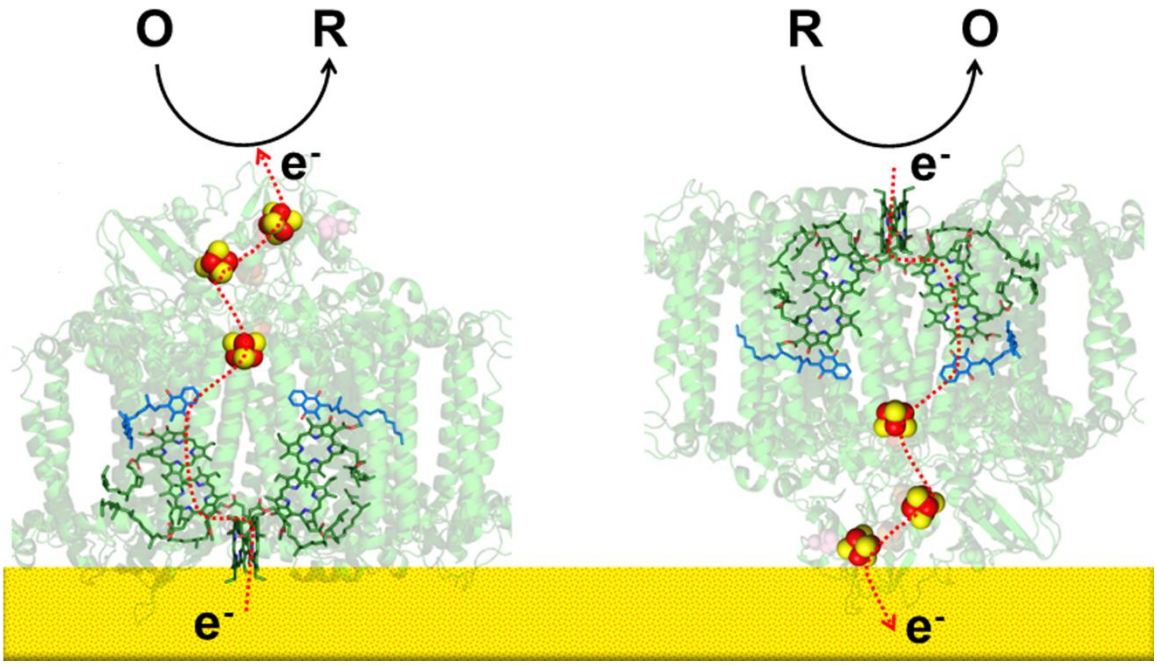

Figure 4.1. Flow of electron through PSI oriented lumenal side down (left) and stromal side down (right) expected for a monolayer in orientations that can produce current in the presence of an electron acceptor or donor.

In this work, the subunits of PSI were modified to contain the sortase recognition sequence, LPETG, with a glutamic acid in the X position, on the exposed C-termini of the trimer. A cysteine-terminated tri-glycine peptide will create a tri-glycine decorated gold surface via thiol bonds between the cysteine residue and gold to be the coupling complement. PSI ligated to gold

surfaces were characterized using atomic force microscopy and photochronoamperometry to correlate current density to protein orientation controlled by the sortase-mediated ligation reaction. This chapter focuses on the genetic manipulation and electrochemical characterization of PsaE-LPETG PSI. The PsaE-modified PSI was the first of the subunit mutants to be completed segregated from the wild type species and characterization of the PsaB, PsaL, and PsaM subunits are ongoing and will not be discussed in depth here. The PsaE subunit was also selected as the first candidate due to the highly exposed nature of its C-termini on the stromal hump of the trimer (Figure 4.3). The location of the targeted sites would likely lead to successful ligation of the complex to the surface and minimize the distance between the iron sulfur clusters of PSI to enhance electron transfer.

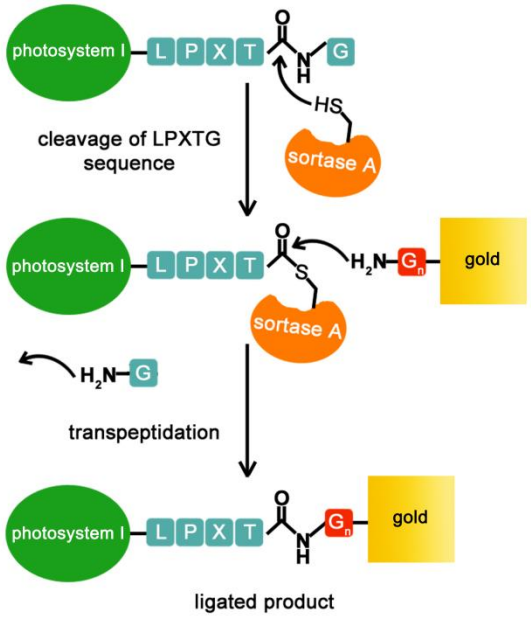

Figure 4.2. Schematic of the sortase A transpeptidation reaction with a C-terminal LPETG-modified photosystem I to ligate the protein complex to a (glycine)n decorated gold surface. Linkage shown not drawn to scale.

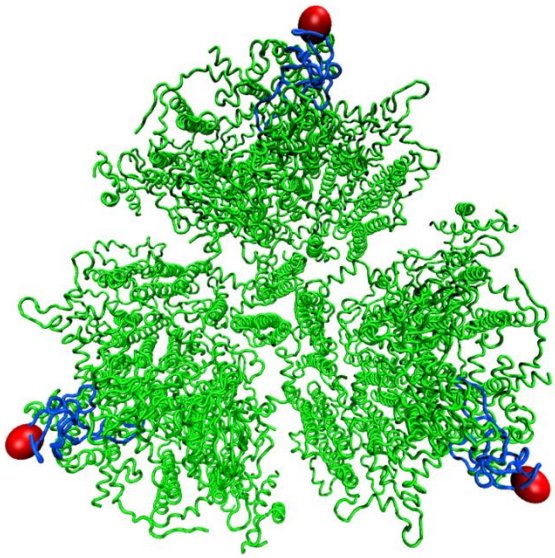

Figure 4.3. Crystal structure of the PSI trimer of *Thermosynechoccocus elongatus* (PDB ID: 1JB0) as a surrogate for *Synechocystis* PCC 6803 PSI with the PsaE subunits highlighted in blue. The red spheres indicate the C-termini of the PsaE subunits targeted for introduction of the LPETG recognition sequence.

4.2 Materials and Methods

4.2.1 Screening of Photosystem I Trimer

Since it is not physically possible to visualize the way a protein is actually oriented on a surface, it is necessary to explore all possible orientations to evaluate the orientation that is best for electron transfer. Though one can speculate that the best orientation is either lumenal side down or stromal side down is best for electron transfer, depending on whether an anodic or cathodic current is desired, one must also assume that the protein linkage via SML has some flexibility to rotate around, and some subunits may be more desirable than others for producing significant net currents. In addition, one must take into consideration that sortase, *in vivo*, attaches peptides on the surfaces of cell membranes, so it is necessary to produce mutants containing the sortase recognition sequence where the sortase enzyme will be able to access the tag, cleave it, and reform an amide bond and attaching the protein to its GGG-complement. Only

educated predictions from the crystal structure for selecting potentially accessible termini can be made.

Using VMD, the crystal structure of PSI from *Thermosynechoccocus elongatus* (1JB0), a surrogate for the PSI of *Synechocystis* sp. PCC 6803 for which there is not a known crystal structure, was modified to show all exposed C-termini and determine possible targets for inserting the LPETG sortase recognition sequence (Figure 4.4A-D). Targeting the C-terminus of the selected subunits of PSI yields a trimer with three potential anchoring sites and opportunities for attaching the complex to the surface. It can be inferred that the likelihood of a triple-sortase anchor is increased by the sortase coupling of at least one of the monomers, assuming all C-termini are exposed on the same face of the trimer. Candidates for successful coupling of PSI to the surface for useful electron transfer are LPETG-modified PsaA, PsaB, and PsaL for lumenal side down coupling to the surface, where P_{700} is accessible to the surface. However, the C-termini of the PsaL subunits are located within the interstitial spaces of the monomers of the trimeric complex as seen in Figure 4.4D, which may have accessibility issues and may likely be the case for the PsaA and PsaB subunits as well, shown in Figure 4.4C. It is possible that the length of the LPETG sequence is sufficiently long enough so that is accessible to sortase. For successful stromal side down coupling, such that the iron sulfur clusters are directed towards the surface for electron transfer to the surface, PsaD and PsaE are ideal due to the exposed nature of their C-termini (Figure 4.4A). PsaC (Figure 4.4A), PsaI, and PsaM (Figure 4.4B) may also be potential candidates for stromal side down coupling to the surface. However, these subunits are buried within the stromal humps of the trimer, as in the case of PsaC, while cleavage of the LPETG motif of PsaI and PsaM may be impeded by the stromal subunits which has a height 3.5 nm [185] above the larger subunits, while the equilibrium length of the LPETGGG linkage is

approximately 2.4 nm (estimated by measuring bonds from N-C termini with PyMOL). Studying the cases of PsaC, PsaI, PsaL, and PsaM may lead to insight of the ability and effectiveness of sortase to access the cleavage site and couple the protein to the surface. In *Synechocystis* sp. PCC 6803 the PsaK is encoded as two different gene sequences on the genome PsaK1 and PsaK2, therefore this subunit was not targeted. PsaF and PsaJ were also not be targeted since their gene sequences are located next to each other on the genome. In targeting PsaF or PsaJ it might be possible for the introduction of the LPETG sequence onto either could introduce undesired effects on the protein expression for both subunits and therefore these subunits will be ignored. Furthermore, the C-terminus of PsaJ is located on the transmembrane region of PSI, rather than on a stromal or lumenal face, which would result in only one coupling event to the surface, decreasing the chances for a favorable orientation for electron transfer to the surface. The LPETGGG linkage may also be too short and inflexible to allow the protein to direct electrons productively.

For donating electrons to the surface via PSI, I assumed that engineering the LPETG sequence on the C-terminus of PsaD or PsaE would result in a stromal side down orientation of the PSI trimer with F_B donating electrons towards the surface. However, this is highly dependent on the redox mediator selected for donating electrons. Assuming the goal is to donate electrons to an electrode surface via PSI, rather than the surface donating electrons to PSI to donate electrons to an electron acceptor, tagging the PsaA and PsaB subunits on lumenal side of PSI will act as controls, where little to no current will be produced in the presence of an electron donor, instead of an electron acceptor, due to lack of orientation of protein to the surface.

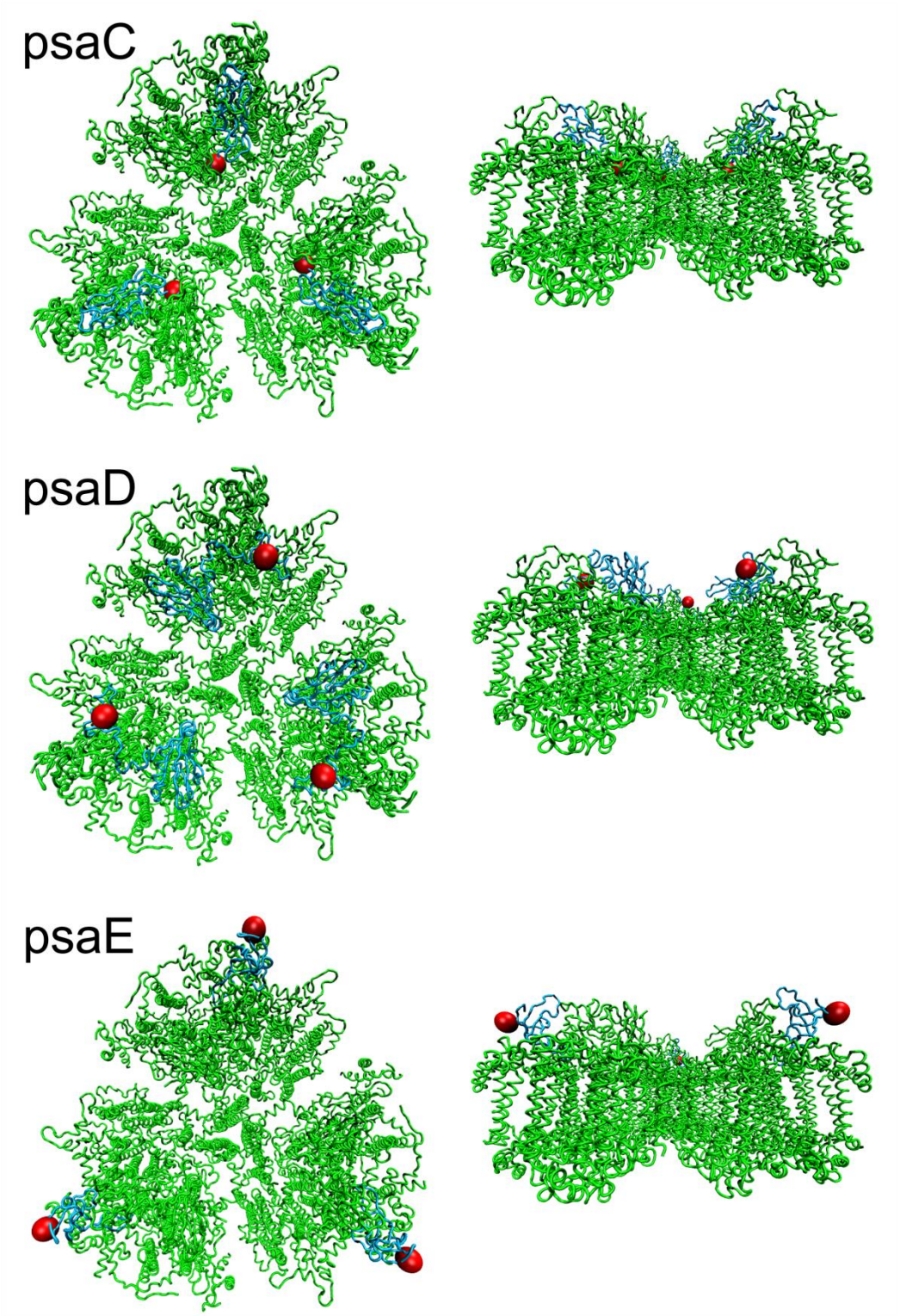

Figure 4.4A. Potential C-terminal target sites for engineering of an LPETG sortase recognition sequence on the stromal side of PSI for PsaC, PsaD, and PsaE. The trimers are shown looking down on the stromal hump (left) and transverse view (right).

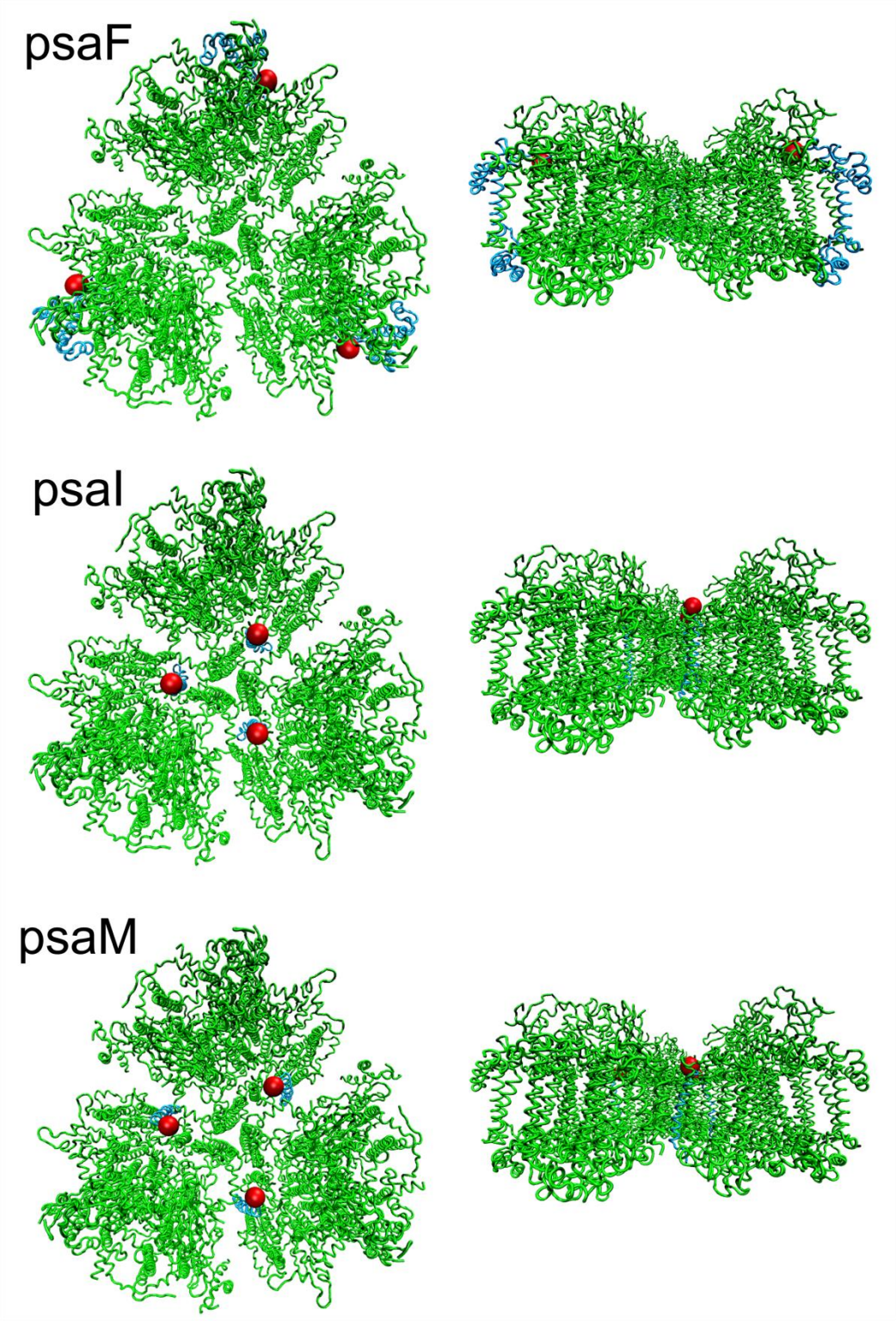

Figure 4.4B. Potential C-terminal target sites for engineering of an LPETG sortase recognition sequence on the stromal side of PSI for PsaF, PsaI, and PsaM. The trimers are shown looking down on the stromal hump (left) and transverse view (right).

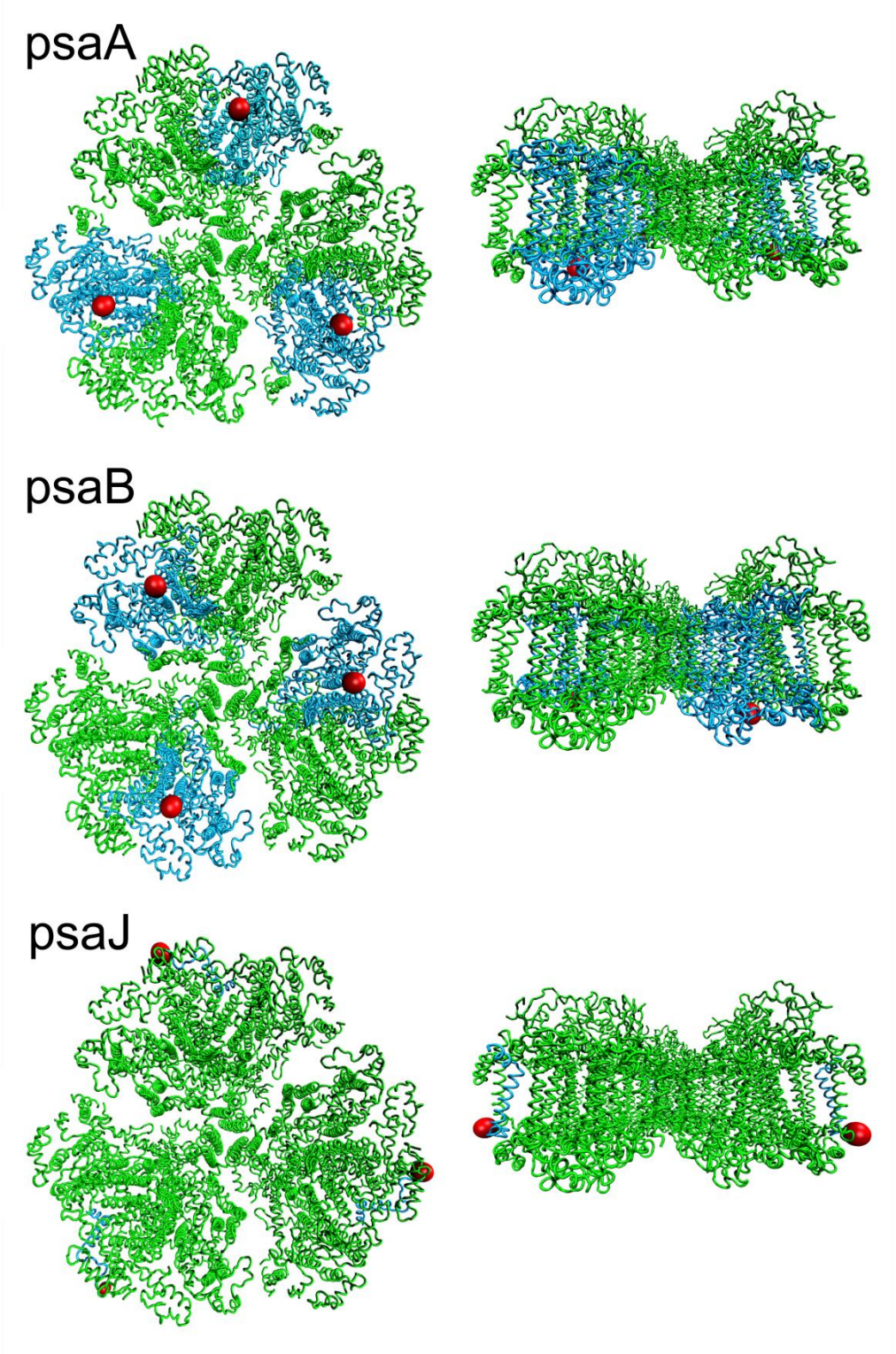

Figure 4.4C. Potential C-terminal target sites for engineering of an LPETG sortase recognition sequence on the lumenal side of PSI for PsaA, PsaB, and PsaJ. The trimers are shown looking down on the lumenal side (left) and transverse view (right).

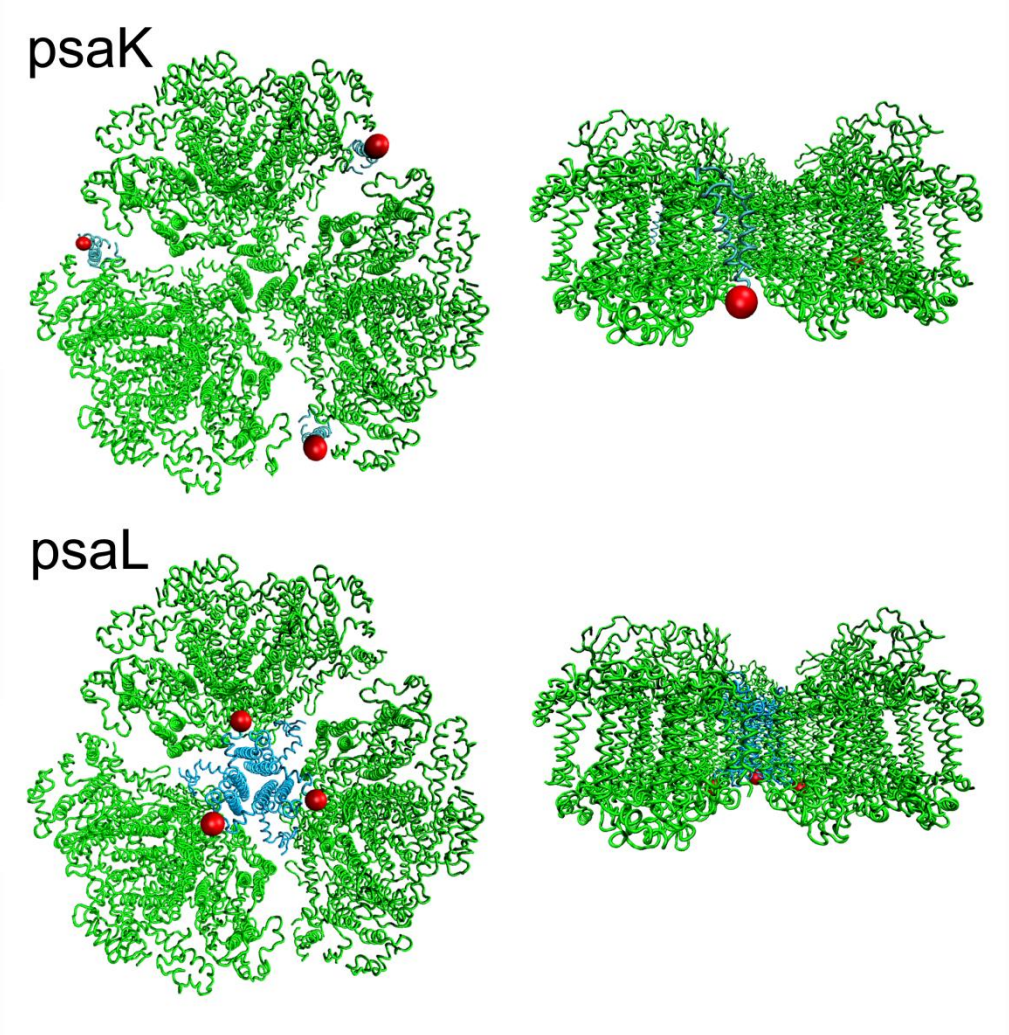

Figure 4.4D. Potential C-terminal target sites for engineering of an LPETG sortase recognition sequence on the lumenal side of PSI for PsaK, and PsaL. The trimers are shown looking down on the lumenal side (left) and transverse view (right).

4.2.2 Construction, Culture, and Purification of LPETG-His tagged Photosystem I

The focus of the genetic modification presented here is on targeting the PsaE subunit. However, all of the techniques used are applicable and were used in targeting the C-termini of the remaining subunits. PSI from the model cyanobacterium *Synechocystis* sp. PCC 6803 (ATCC: 27184) was engineered to express an LPETG recognition sequence necessary for sortase coupling on the exposed C-terminus of the PsaE subunit. The PsaE sequence from *Synechocystis*

genomic DNA was modified by PCR to include a sequence encoding a C-terminal sortase recognition tag (LPETG, glutamic acid is used in the middle position) and a six-histidine tag to facilitate protein purification.

The PsaE-LPETG-His_6 mutant photosystem I strain of *Synechocystis* PCC 6803 was generated by transforming wild-type 6803 cells with PsaE-LPETG-His plasmid under conditions following the protocol for construction of mutants by Eaton-Rye [186] and guidelines for optimal transformation of *Synechocystis* established by Zang et al. [187]. PsaE was targeted in particular due to the exposed nature of its C-terminus and the likelihood that sortase would be able to access the LPETG tag (Figure 4.4A). Genomic DNA was extracted from wild type *Synechocystis* sp. PCC 6803 following the protocol by Eaton-Rye. The gene sequence of the PsaE subunit was obtained from the online resource Kazusa CyanoBase (http://genome.microbedb.jp/cyanobase), as well as the 1 kb upstream and 1 kb downstream regions of the target gene. Primers were designed to target the gene of interest and the respective 1 kb upstream and 1 kb downstream regions; Zang et al. have shown that with increasing homology, the transformation efficiency increases [187]. The target gene and the upstream and downstream regions were analyzed to determine if restriction sites were present in the gene sequence compatible with the pGEM Easy-T vector (Promega) and to avoid undesired cutting of the gene from non-unique restriction sites in subsequent cloning steps. The upstream forward primer (UF1) introduced an ApaI restriction site 1 kb upstream from the gene and the upstream reverse primer (UR1) introduced an AatII restriction site, a six-histidine moiety, and the LPETG sortase recognition sequence to the C-terminus of PsaE (sequence shown in Table 4.1; primer sequences for other subunits can be found in Appendix III). The downstream primers (DF1, forward and DR1, reverse) introduced SacI and NsiI restriction sites at the N- and C-terminus of

a 1 kb fragment downstream from the PsaE gene, respectively. A kanamycin resistance cassette (from pCkmTe used in the dissertation work of Iwuchukwu and codon optimized for expression in *T. elongatus* [188]) was introduced into the pGEM Easy-T vector via TA cloning. The target gene sequences were amplified from wild type genomic 6803 DNA using conventional PCR. Each DNA fragment was double digested with appropriate restriction enzymes and ligated into the pGEM:kan^r plasmid vector and transformed into JM109 competent *E. coli* cells sequentially until the desired construct was created (Figure 4.5). Positive clones were selected and plasmid DNA was extracted using a plasmid extraction kit (Promega A1223). The new plasmid was sequenced to verify the correct insertion of the LPETG sequence. A 10 mL culture of transformed *E. coli* cells was grown, such that at least 5 µg of plasmid DNA could be recovered for transformation into wild type *Synechocystis* cells.

Table 4.1. Primer sequences used for PCR amplification of genomic target sites. Underlined sequence for upstream reverse primer (UR1) encodes the LPETGH$_6$ sortase recognition sequence at the end of the PsaE gene.

Primer	Primer sequence (5' – 3')
UF1	AAAGGGCCCCAGTTCATCGATGGTGAAGGG
UR1	AAGACGTCCTAGTGGTGGTGGTGGTGGTGGCCCGTCTCAGGAAG TTTTGCCGCCGCTTGCACCAATTC
DF1	AAAGAGCTCCAGAAGTTGAAACAGTATGCCGGG
DR1	AAAATGCATAAACTAGTGCCTCCAGCCTCA

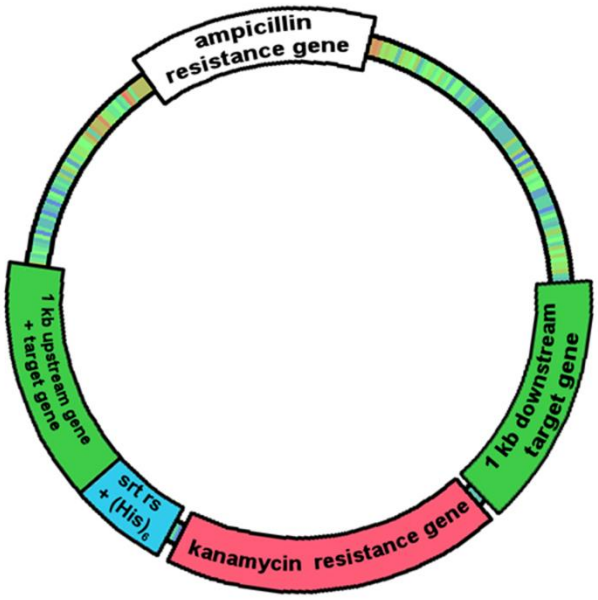

Figure 4.5. Psa-subunit LPETG mutant construct. pkan-Psa-subunit plasmid containing flanking regions of the gene/subunit of interest and a kanamycin resistant gene.

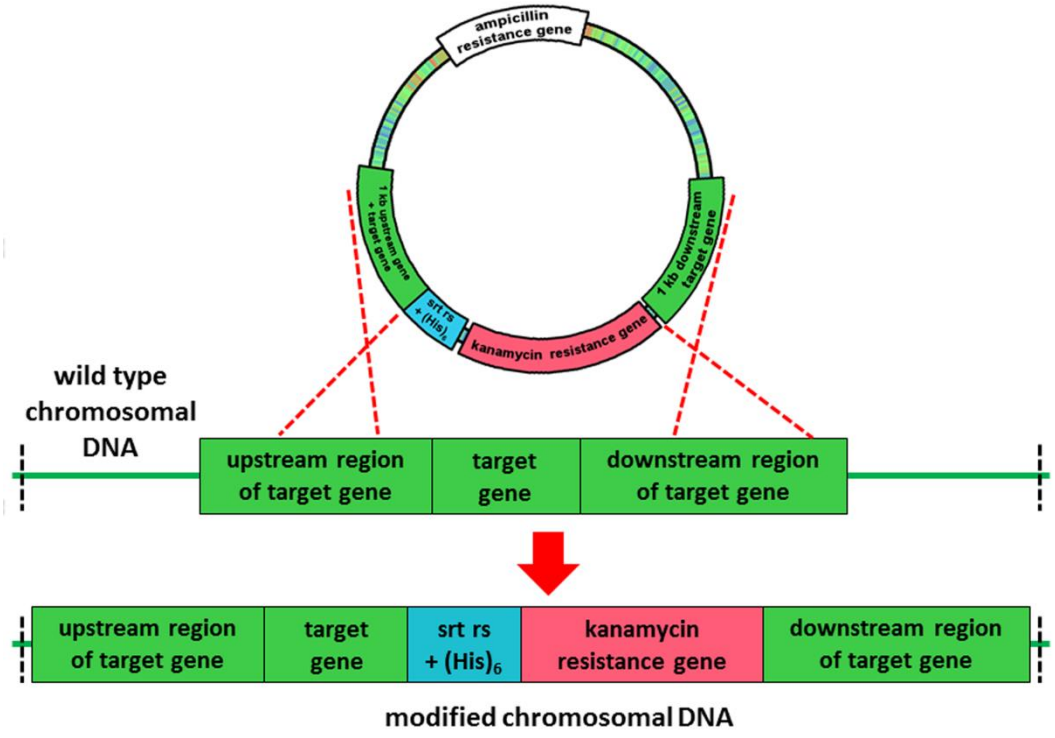

Figure 4.6. Schematic for homologous recombination of mutant construct and genomic DNA.

Wild type *Synechocystis* was transformed following the protocol by Zang et al. [187] 5 mL cultures of the wild type strain were grown in BG-11 media without antibiotics for approximately 3 days or until an OD_{730} = 0.2 – 0.8 was achieved. The cells were centrifuged at 2760 x g for 5 minutes at room temperature and washed with fresh BG-11 media, repeating this step twice. The pellet was then resuspended with BG-11 media to an OD_{730} = 2.5 such that 0.5 mL was available per transformation. The LPETG-gene modifying plasmid (~2 – 10 μg) was added to the 0.5 mL volume of cells in a 1.5 microcentrifuge tube. The microcentrifuge tube was seated in a glass culture tube, slanted in a tube rack, and incubated at 30°C, 25 $\mu E/m^2/s$ light intensity, with shaking at 120 rpm for 5 hours. Transformed cells were pipetted onto a sterile piece of Whatman filter paper and placed on top of non-selective BG-11 agar. The filter was dried with sterile house air (outfitted with a 0.22 μm filter) before placing into a lighted incubator at 30°C shielded from light (~15 $\mu E/m^2/s$ light). The filters rested on non-selective agar for three days to help the cells recover and undergo homologous recombination (as shown in Figure 4.6) before being transferred to 12.5 μg/ml kanamycin selective BG-11 agar for three days. After recovering on a half dose of selective media, the filter was transferred to full antibiotics at a concentration of 25 μg/ml kanamycin. Growth on full antibiotics took two to three weeks for colonies to appear (as seen in Figure 4.7). Colony PCR was performed on colonies that appeared on 25 μg/ml kanamycin using UF1 and DR1 primers to amplify the target subunit for sequencing. Weekly re-streaking of mutant colonies was performed to segregate true mutants from those retaining copies of the wild type genome, since *Synechocystis* 6803 has at least 12 copies of its genome [186]. Increased selection pressure was implemented by increasing the kanamycin concentration to 50 μg/mL. After 3 months of re-streaking, colonies were sequenced again to ensure only the mutant genomic species was present. Figure 4.8A verifies

that the $LPETGH_6$ was correctly inserted into the genome. This is further supported by Figure 4.8B, which shows the 1 kb size shift between the wild type and mutant PCR products obtained

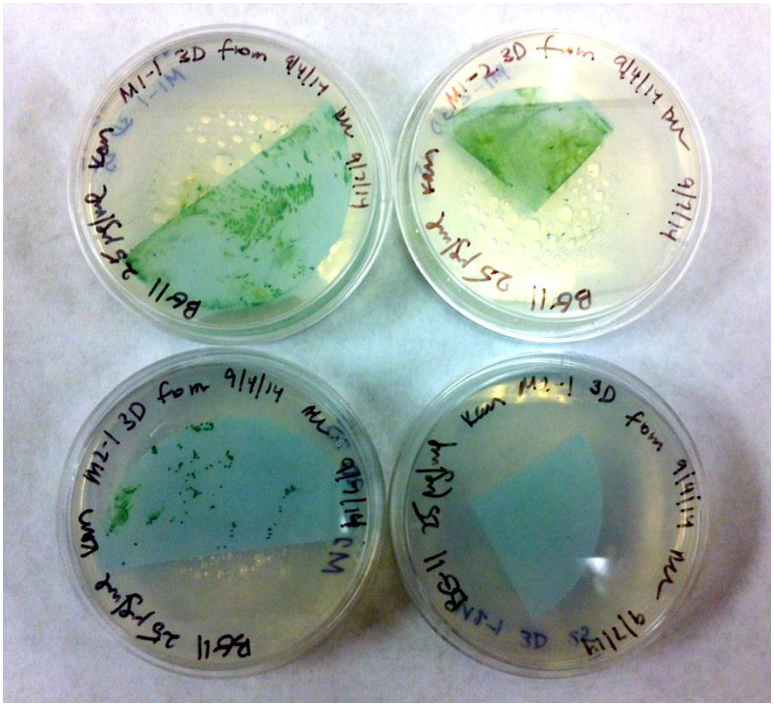

Figure 4.7. Sample mutant 6803 cell growth on filters after two weeks on BG-11 plates with 25 µg/mL kanamycin.

from using the same forward and reverse primers on isolated wild type and mutant PsaE genomic DNA. The lack of the wild type product band in the mutant lane confirms the elimination of the wild type species in the mutant genome. Frozen stocks of the mutant strains were made by mixing a 3 day old culture pellet with BG-11 media amended with 15% (final volume) glycerol and stored at -80°C.

The constructs for PsaB-LPETG, PsaL-LPETG, and PsaM-LPETG PSI have also been successfully constructed, transformed, and sequenced as described above with the primers listed in Appendix III. Figure 4.9 shows the 1 kb size shift between the wild type and mutant PCR

products for PsaL and PsaM three weeks after transformation. Compared to the PCR products from the PsaE-LPETG modified genomic DNA, the PsaL and PsaM mutants have not been fully segregated, as seen in the faint bands corresponding to the mutant genomic product with significant wild type product present. This indicates these mutants require continued segregation to ensure complete separation of the mutant strains from the wild type species and the difficulty associated with generating cyanobacterial mutants.

Confirmed mutants were grown in 50 µg/ml kanamycin selective BG-11 media in a New Brunswick™ BioFlow3000 Bioreactor (Eppendorf, Inc., Enfield, CT, USA) at 30°C under 25 $\mu E/m^2/s$ illumination, 350 RPM impeller agitation, and 150 ml/min air flow rate. Cells were harvested, pelleted, and frozen at –80°C before PSI extraction. PSI was extracted from the mutant PsaE 6803 strain following modified protocols [10, 189-191]. Frozen cells were resuspended in Buffer A (50 mM MES-NaOH, pH 6.0; 10 mM $MgCl_2$; 5 mM $CaCl_2$; 25% v/v glycerol) by vortexing. Thermo Scientific™ protease inhibitor cocktail for His-tagged proteins was added at 100 µL per 10 mL cell suspension before cell lysis with a French press at 25,000 PSI. The cell lysate was collected and spun down at 19,000 x g for 30 minutes. The supernatant was removed and the cell lysate pellet was resuspended in Buffer A and solubilized in DDM at final concentration of 1% (wt/v) for 30 minutes at 4°C. The solubilized solution was centrifuged at 19,000 x g for 30 minutes. The recovered supernatant containing the solubilized fraction of the LPETG-His-tagged PSI was run on a HisPur Cobalt (Thermo Scientific™) column to purify the tagged protein from undesired proteins. The column and sample were equilibrated with Buffer A, pH 7.8, 0.04% (wt/v) DDM, 5 mM histidine. After applying the PSI sample and re-applying the flow through, the column was washed with nine bed volumes or until the 280 nm UV-VIS measurement of the wash reached a baseline. The protein was eluted from the column using

Buffer A, pH 7.8, 0.04% (wt/v) DDM, 100 mM histidine. Elution fractions were pooled and dialyzed in Buffer A with 0.04% (wt/v) DDM for two hours, twice, followed by overnight dialysis at 4°C with gentle stirring. An SDS-PAGE gel of the column fractions was run and a size shift in LPETG modified PsaE compared to the wild-type was observed (Figure 4.8C). An SDS-PAGE gel of the column fractions was run and a size shift in LPETG modified PsaE compared to the wild-type was observed. Interestingly, the mutant-PsaE, which was expected to run higher with a sequence predicted molecular weight of 9.47 kDa, appeared to run lower on the 4-12% SDS-PAGE gel than wild type-PsaE, with a predicted molecular weight of 8.15 kDa. This size-shift is likely due to the amino acid composition of the sortase recognition tag and difference in the SDS binding by the mutant-PsaE compared to the wild type, which changed the mobility of the protein compared to the predicted sequence.

4.2.3 Purification of sortase

Sortase-His6 enzyme was expressed as described by Levary et al. [97] BL21 DE3 *E. coli* (Invitrogen) were transformed with pHTT27 (a gift to Dr. Eric Boder from Dr. Olaf Schneewind, University of Chicago). The culture was induced with 1 mM isopropyl-ß-D-1-thiogalactopyranoside (IPTG, Fisher BioReagents™ BP1620) for 4 hours after reaching an OD_{600} of 0.4. The cytosolic proteins were extracted using B-PER reagent (Thermo Scientific™) from pelleted cells that had been frozen overnight at -20°C. Sortase was purified from cell lysate using His-Pur resin (Thermo Scientific™) followed by buffer exchanged into 50 mM Tris, 150 mM NaCl, pH 8 using Spectra/Por 6-8 kDa molecular weight cutoff, 40 mm width dialysis tubing (SpectrumLabs, part no. 132660), replacing the buffer twice after two hours, followed by overnight dialysis.

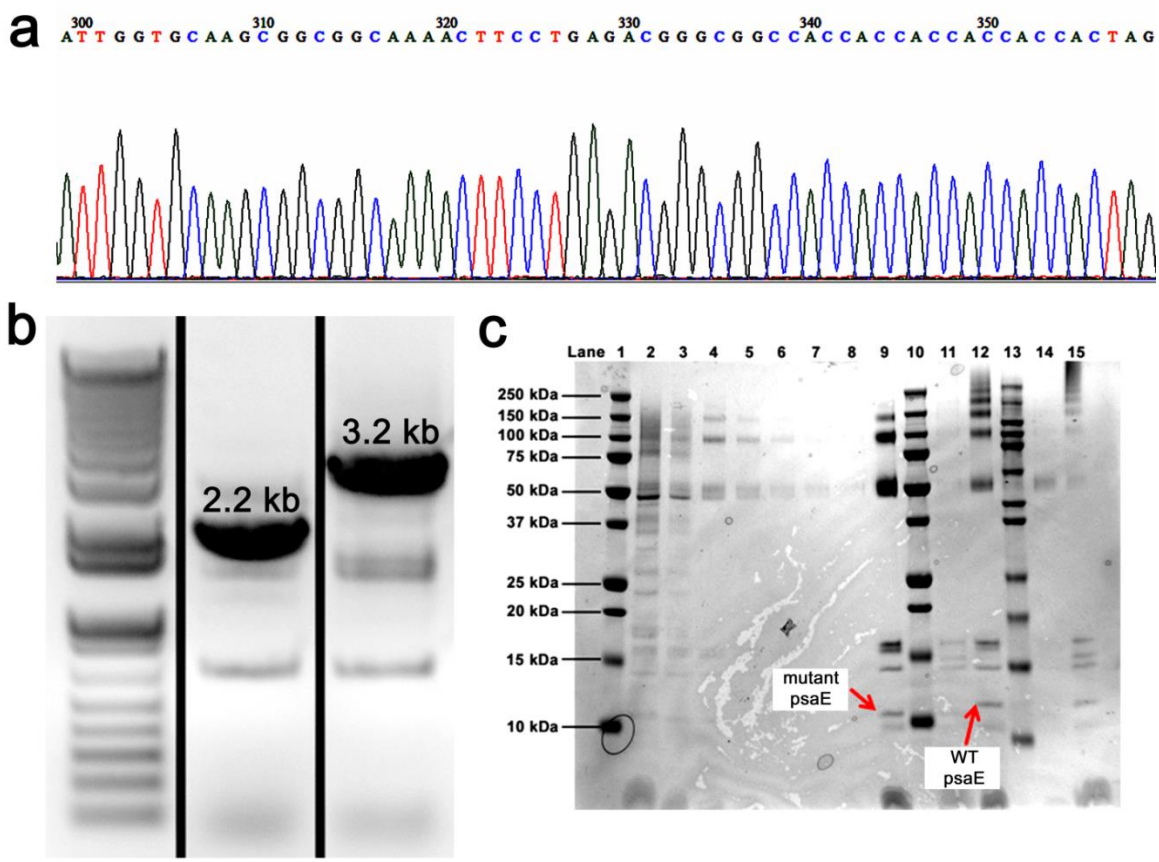

Figure 4.8. Characterization of mutant PsaE-PSI. (a) Sequencing result of mutant PsaE 6803 genomic DNA shows insertion of LPETG$(H)_6$ sequence into mutant genome. (b) 1 kb band shift from insertion of kanamycin gene confirms segregation of WT genome (2.2 kb band from 1 kb upstream PsaE gene, plus PsaE gene, plus 1 kb downstream PsaE gene) from mutant 6803 (3.2 kb band from 1 kb upstream PsaE gene, plus PsaE gene, plus kanamycin resistance, plus 1 kb downstream PsaE gene). (c) SDS-PAGE gel of fractions from His-column purification fractions. Lane 1: 10-250 kDa marker, 2: Flow through, 3-8: Wash, 9: mutant PSI, 10: 10-250 kDa marker, 11: mutant PSI, 1:4 dilution, 12: WT 6803 PSI, 13: 7.5-250 kDa marker, 14: mutant PSI, 15: WT 6803 PSI, 1:2 dilution.

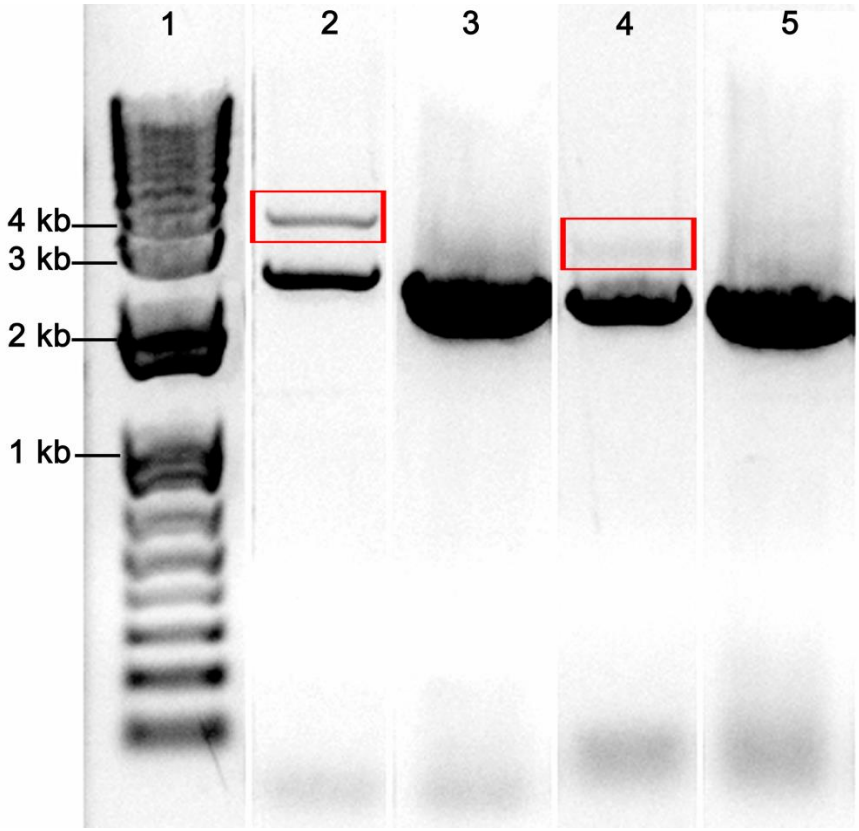

Figure 4.9. Gel electrophoresis of PCR products from mutant and wild type PsaL and PsaM genomic DNA in 0.8% agarose gel. Confirmation of PsaL and PsaM mutants is shown by 1 kb band shift from insertion of kanamycin gene. Lane 1: 1 kb plus DNA molecular weight marker, Lane 2: PsaL-LPETG mutant product (4.47 kb band from 1 kb upstream PsaL gene, 1.47 kb PsaL gene 1.1 kb kanamycin resistance gene, and 1 kb downstream PsaL gene, 3.47 kb wild type product band. Lane 3: PsaL wild type product band (3.47 band from 1 kb upstream PsaL gene, 1.47 kb PsaL gene, and 1 kb downstream PsaL gene. Lane 4: PsaM-LPETG mutant product (4.2 kb band from 1 kb upstream PsaM gene, 1.1 kb PsaM gene, 1.1 kb kanamycin resistance gene, and 1 kb downstream PsaM gene, 3.1 kb wild type product band. Lane 5: PsaM wild type product band (3.1 band from 1 kb upstream PsaM gene, 1.1 kb PsaM gene, and 1 kb downstream PsaM gene). Red rectangles indicate mutant PCR products.

To verify the sortase was active and the LPETG tag on the PsaE-LPETG PSI mutant was present and accessible, the mutant PSI was incubated with sortase and a GGG-GFP along with the appropriate controls. A mix of 10 µM PSI (mutant and wild type), 100 µM GGG-GFP, 110 µM sortase, 60 µM $CaCl_2$, and 1X TBS at pH 8.0 with 0.04% DDM was incubated at 38°C with gentle stirring (50 rpm) for 4 hours. The reaction was inactivated with 10 mM (final) EDTA.

Figure 4.10 shows that the sortase was active and the LPETG sequence was successfully incorporated into the mutant PsaE-LPETG PSI strain as determined by the size shift between the green and red lines of Figure 4.10 in the controls where no sortase was added in lane 6 and in comparison to the WT PSI controls (lanes 8 and 9), which did not react and are in line with the red guide line and the GFP band (27 kDa) did not shift. The green line indicates the PsaE-LPETG shift, that should have resulted in a band at approximately 35 kDa ((8.1 kDa + 0.5 kDa = 8.6 kDa), however GelAnalyzer software indicates that the shift is approximately 3 kDa, which is much smaller than expected. This may be the result of wrong gel selection, since a 12% Bis-Tris LifeTechnologies NuPAGE Novex gel run with MES buffer does not have sufficient band separation between 31 kDa and 36 kDa, the region where the fusion should have occurred. This band shift is further complicated by the PsaE-LPETG-mutant running shorter than the wild type PsaE band as seen in Figure 4.8C. The PsaE-LPETG:GGG-GFP fusion band from lane 7 was sent to Bioproximity for in-gel mass spectrometry-based proteomic profiling and analysis using a LTQ Velos instrument with 30 minutes LC-MS/MS gradient time, detecting GFP, PsaD, and contamination. Therefore the fusion has not been definitively confirmed.

4.2.4 Preparation of Peptide and PSI Decorated Gold Surfaces

Slides coated with 100 Å gold (Platypus Technologies) were cut into ½" x ½" squares and cleaned in a 3:1 ammonium hydroxide:hydrogen peroxide base piranha solution for ten minutes (until bubbles formed on the gold surface) to remove organic contaminants. The substrates were then rinsed thoroughly with oxygen-free ddH_2O before being immersed in a cysteine-terminated tri-glycine (Gly_3) peptide solution for 48 hours. Incubating the substrates with the peptide created a dense monolayer of Gly_3 via thiol bonds with the gold which serves as

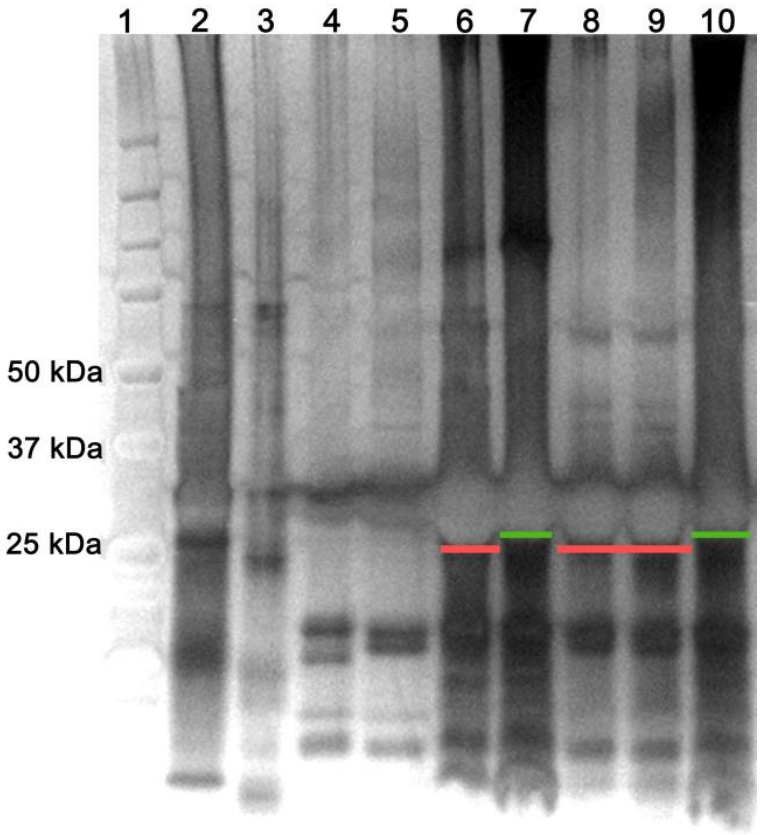

Figure 4.10. SDS-PAGE gel of PsaE-LPETG PSI sortase ligation to GFP. Lane 1: 10-250 kDa marker, 2: GFP, 3: sortase, 4: mutant PSI, 5: WT PSI, 6: GFP, mutant PSI, -sortase, 7: GFP, mutant PSI, +sortase, 8: GFP, WT PSI, -sortase, 9: GFP, WT PSI, +sortase, and 10: GFP, mutant PSI, +sortase.

the complimentary acceptor of the sortase-catalyzed ligation of modified PsaE-LPETG-PSI to the surface. The peptide solution was prepared by dissolving dried peptide in an isopropanol-DMF solution with vortexing and diluting to the appropriate concentration under oxygen-free conditions to prevent disulfide bond formation between peptides in solution. The peptide-coated substrates were rinsed with O_2-free ddH_2O to remove excess peptide and dried under nitrogen prior to analysis using atomic force microscopy and PSI deposition.

The ¼ in^2 peptide-coated gold substrates were incubated with a solution containing modified PsaE-LPETG-PSI (100 µM chl *a* ~ 0.35 µM PSI trimer), sortase (5 µM), $CaCl_2$ (10

mM), 0.04% (wt/v) DDM, and 1X pH 7.6 TBS buffer applied as a 150 µL droplet (Figure 4.11). The substrates were placed in a petri dish that was wrapped with parafilm to prevent evaporation and incubated at 38°C shielded from light for 4 hours. The PSI-LPETGGGC-gold surfaces were washed with ddH_2O to remove excess PSI not bound by the sortase linkage and stored in 1X TBS buffer with 0.04% (wt/v) DDM. The surfaces were dried with nitrogen before use such that a 1-¼ inch piece of copper tape (JVCC CFL-5CA) could be attached to a corner of the substrate/working electrode and folded onto itself, adhesive side together, to make a sealed connection with the working electrode for use in the custom electrochemical cell.

4.2.4 Atomic Force Microscopy

Atomic force microscopy, or AFM, is a scanning probe technique in which a sharp tip on the end of a cantilever is scanned over a substrate, and forces between the substrate and the tip are measured by monitoring the deflection of the cantilever. This technique can provide information about the topography of the sample on the scale of a few microns down to several nanometers and can even provide atomic resolution in some cases. An AFM provides a basic advantage over other high-resolution imaging techniques such as scanning tunneling microscopy in that the sample does not need to be electronically conductive, which allows the application of AFM to biological systems and other systems composed primarily of insulating materials such as glasses and ceramics. There are several modes in which an AFM is commonly operated: contact mode and non-contact ("tapping") mode. In contact mode, the tip remains in contact with the sample as it is scanned over the surface, and the topography is measured directly by monitoring the beam deflection. During tapping mode, the cantilever is oscillated such that it occasionally contacts the sample, hence the term—tapping. This method nearly eliminates frictional forces

associated with lateral movement of the tip and can provide improved resolution on rough samples or substrates on which the features of interest are weakly attached and prone to being pushed or dragged by the tip.

Topographical scans were performed using an Asylum Research MFP-3D atomic force microscope with silicon Olympus AC240TS cantilevers with a spring constant of 2 (0.5 – 4.4) N/m and resonant frequency of 70 (50 – 90) kHz. 20 µm by 20 µm samplings of each control were scanned in four sections of each ¼ in^2 sample. The uniformity of deposition was judged by further increasing the magnification to encompass 5 µm by 5 µm sections within each 400 μm^2 section.

4.2.5 Electrochemical Measurements

Assuming that the heterogeneous reactions are reversible, single-electron transfer events that occur between the working electrode and the redox couple, the electrode potential E(t) is related to the concentrations of reduced and oxidized mediators at the electrode surface at time *t* by the Nernstian expression (equation 1) [192]:

$$E(t)=E^{0'}+\frac{RT}{F}\ln\frac{C_O(0,t)}{C_R(0,t)} \qquad (1)$$

where E^0 is the formal potential of the working electrode at standard conditions, R is the gas constant, T is the absolute temperature, F is Faraday's constant, and $C_O(0,t)$ and $C_R(0,t)$ are the concentrations of the oxidized and the reduced form of the mediator at any time t and position x = 0 (at the surface of the electrode, the electrode-mediator interface) respectively. When the working electrode is illuminated, charge separation rapidly occurs within PSI causing the oxidation of the P_{700} reaction center and the formation of a reduced distal iron sulfur cluster F_B^- described by equation 2:

$$P_{700}+F_B \overset{h\nu}{\rightarrow} P_{700}^{+} + F_B^{-} \qquad (2).$$

As the working electrode is exposed to light, redox reactions occur between the P_{700}^{+} and F_B^{-} reaction centers and the electrochemical mediators at the electrode interface undergo the reactions described by equations 3 and 4:

$$P_{700}^{+} + R \rightarrow P_{700} + O \qquad (3)$$

$$F_B^{-} + O \rightarrow F_B + R \qquad (4)$$

where O and R symbolize the oxidized and reduced states of the electrochemical mediators, respectively.

The change in the surface concentration of the mediators as the reactions proceed drives the change in the current density. The current decays with time due to the depletion (oxidation or reduction depending on the orientation of interest) of the mediators near the surface of the electrode. The conversion of reduced species to oxidized species (or vice versa) creates a concentration gradient between the mediators at the surface and in the bulk, which causes diffusion of the two species in response to the gradient. When irradiation of the working electrode stops, the photogeneration of P_{700}^{+} and F_B^{-} also ceases, causing the photocurrent generation to stop.

Assuming the electron transfer events of PSI on the surface reversible, implying that PSI is present in two orientations for electron transfer, stromal side down with the F_B iron cluster near the surface or lumenal side down with the P_{700} reaction center near the surface, the reaction can be described simply by equation 5:

$$O + e^{-} \longleftrightarrow R \qquad (5)$$

Therefore the equation describing the net current production at a given time, t, is the sum of the cathodic and anodic currents (equation 6):

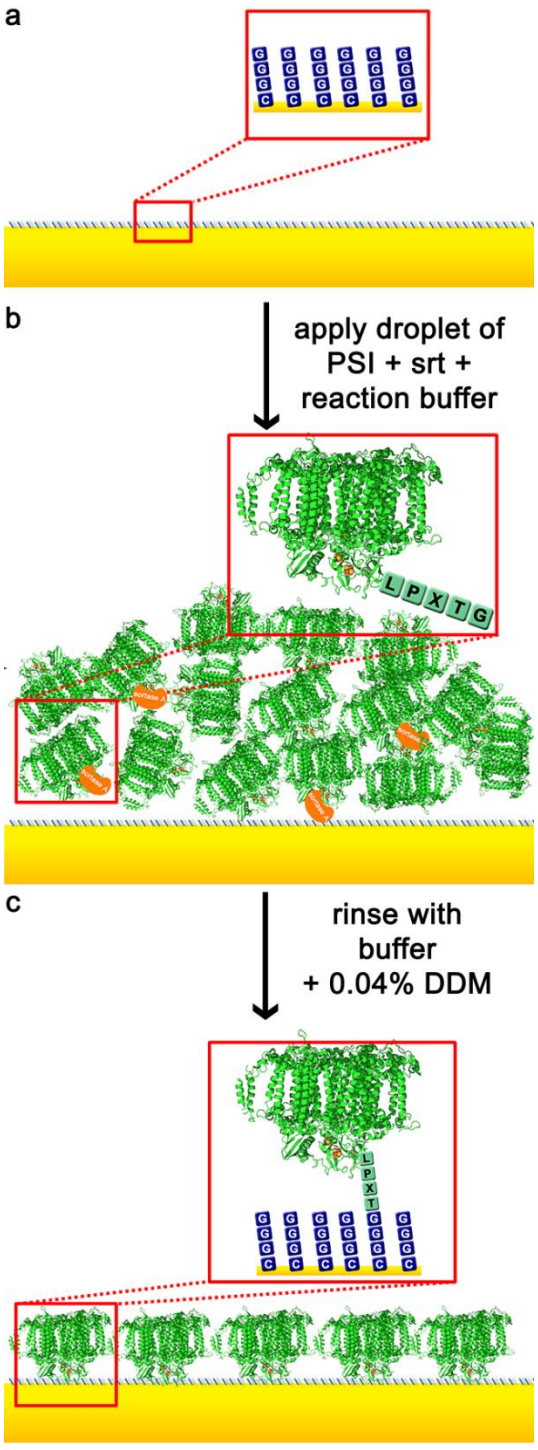

Figure 4.11. Sortase-mediated ligation technique for forming oriented PSI monolayers. Sortase linkage shown not drawn to scale.

$$i_{net}(t)=FA[k_{red}C_O(0,t)-k_{ox}C_R(0,t)] \quad (6)$$

where F is the Faraday constant, A is the area of the electrode, and k_{red} and k_{ox} are the heterogeneous rate coefficients for the reduction and oxidation reactions, respectively. When the cell is exposed to light, the photocatalytic response produced by PSI complexes immobilized to the electrode surface produces an increase in anodic current, which is accompanied by an increased rate of consumption of species R at the electrode surface for the stromal side down orientation. This process prompts the formation of a gradient in the concentration of R that occurs away from the electrode surface as time progresses and causes the current to decease as $t^{1/2}$ as described by Cottrell's equation (equation 8). Sustained irradiation results in an accumulation of the oxidized species near the electrode surface, which causes a cathodic response when the light is turned off as this excess is reduced by the electrode.

Photochronoamperometry is an electrochemical method variation of chronoamperometry, where a constant potential is applied to the working electrode and the resulting current density is measured as a function of time. This technique is most commonly used to verify the photocatalytic role of PSI in systems where it has been attached to conductive surface for current production. During a photochronoamperometric experiment, the working electrode surface is exposed to light in the presence of electron mediators. In the presence of components that participate in photo-induced redox reactions, a variation in the current density can be measured in response to irradiation. The experiments presented in this work were performed using a three-electrode cell (schematic shown in Figure 4.12) where the working electrode is a thin gold electrode modified with covalently attached PSI, a saturated calomel reference electrode, and a platinum wire counter electrode.

The current production for the system in this study was assumed to be completely diffusion-limited and was described by Cottrell's equation. This assumption is based on a planar electrode with an unstirred mediator solution with a general reaction described by $O + ne^- \rightarrow R$, where O is the oxidized species, ne^- is the number of electrons, and R is the resulting reduced species.

The calculation of the diffusion-limited current (i_d) and concentration profile of the oxidized species C_O, was done by solving the linear diffusion equation (7):

$$\frac{\delta C_O(x,t)}{\delta t} = D_O \frac{\delta^2 C_O(x,t)}{\delta x^2} \qquad (7)$$

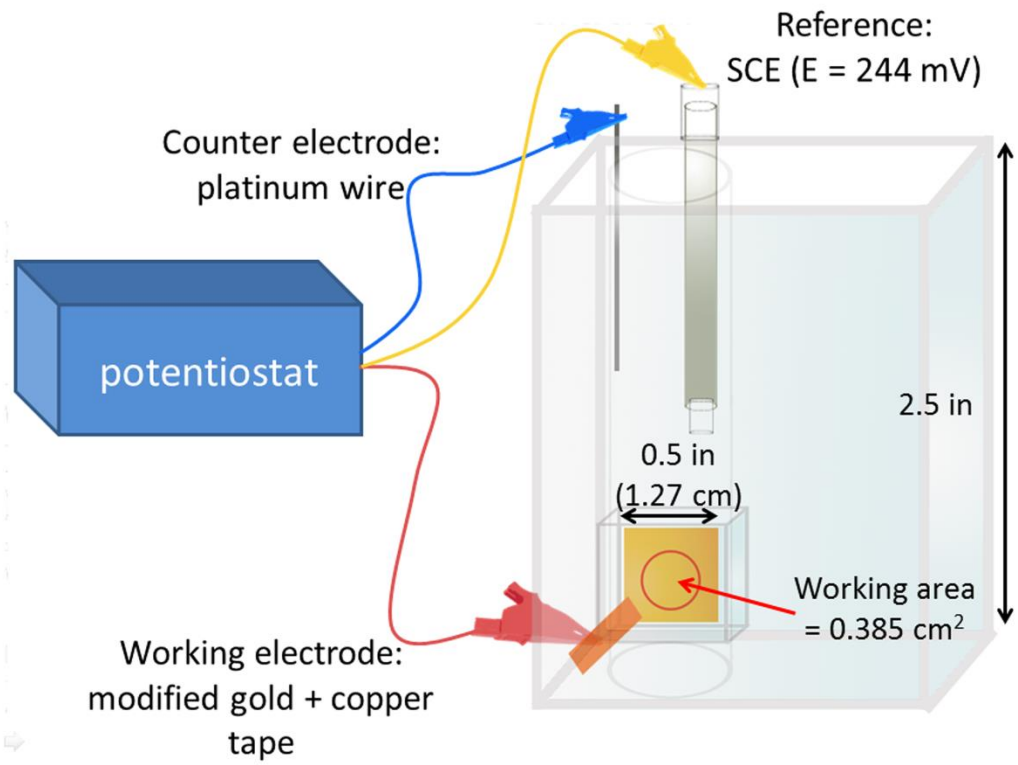

Figure 4.12. Three-electrode configuration of electrochemical cell with Pt-wire counter electrode, saturated calomel reference electrode, and gold substrate working electrode, with 1.27 cm by 1.27 cm working area.

with boundary conditions: $C_O(x,0)=C_O^*$ (initial condition), $\lim_{x\to\infty} C_O(x,t)=C_O^*$ (semi-infinite condition), and $C_O(0,t)=0$ for $t > 0$, where the initial condition assumes that the solution is homogenous before the experiment begins at $t = 0$, the semi-finite condition assumes that regions far from the electrode are unperturbed by the experiment and the concentration is equivalent to the bulk concentration, and the third condition asserts that the concentration of the oxidized species at the surface is equal to zero.

Applying Fick's second law for the diffusion of the heterogeneous reactant to the electrode surface and assuming the above boundary conditions, and the Cottrell equation is obtained via Laplace transform yielding equation 8:

$$i(t)=i_d(t)=\frac{nFAD_O^{1/2}C_O^*}{\pi^{1/2}t^{1/2}} \qquad (8)$$

where n is the number of electrons transferred, F is Faraday's constant, A is the effective working area, D is the diffusion coefficient, and C* is the bulk concentration of the redox couple. This equation predicts that depletion of the electroactive species near the surface will result in a current density decrease relationship of $t^{-1/2}$. While the photochronoamperometric experiment presented in this chapter are not completely diffusion-limited, due to the nature of PSI, the current density shows a similar time-decay profile due to the accumulation of concentration gradients at the electrode surface as the diffusing redox mediator reacts at the electrode/electrolyte interface. Additional details can be found in Chapter 3 of Electrochemical Methods by Bard and Faulkner [192].

Photochronoamperometry measurements were made using a BioLogic SP-200 potentiostat with a custom three-electrode cell configuration (provided by Kane Jennings and David Cliffel, Vanderbilt University). The gold substrate with PSI and suitable controls were used as the working electrode with a 0.385 cm^2 effective working area. A saturated calomel

electrode (+0.244 V vs. SHE) was used as the reference electrode and a platinum wire was used as the counter electrode. The electrochemical mediator solutions used for our experiments were 200 µM potassium ferro- or ferricyanide, in pH 7 PBS buffer, and 100 mM KCl. The electrode cell was illuminated with a Fiber-Lite DC regulated illuminator (Dolan-Jenner Industries) with an OSRAM 150 W quartz halogen lamp. The light was filtered through a 590-nm long-pass filter and provided 500 µE/m^2/s (10.5 mW/m^2) light intensity. The current density was calculated by taking the difference in the dark current and the current under illumination after 15 s. Amperometry measurements were made after measuring the open circuit potential (OCP) of the cell in the dark until a baseline value was reached (~3 minutes). All measurements were made under the OCP measured for each sample (~ -100 mV), such that the dark current would yield a value of approximately 0 nA/cm^2 in the dark.

Prior to illumination the dark current was allowed to equilibrate to a baseline value (~0 nA/cm^2) at the applied OCP for ~15 s, then the working area was illuminated for 10-20 s, and then the current was allowed to return to baseline for 20 s before repeating the light-dark cycle for three cycles, where the instantaneous response was measured and recorded by the EC-Lab® program provided with the electrochemistry workstation.

Cyclic voltammetry is a potential sweep method where a potential is applied to the working electrode and is varied with time while measuring the resulting current. The potential is varied from an initial potential, E_i, to a final potential, $E_{f,}$ and then returned to the initial potential E_i, hence the term "cyclic." If the system in question contains a redox couple whose formal potential is between E_i and E_f, a peak in the measured current will be observed. If $E_i < E_f$, this indicates the oxidation of the redox couple results in an anodic current and will be observed during the forward scan, and the reduction of the redox couple, measured as cathodic current,

will be observed during the reverse scan. Expressions for the potential dependence of the rates of a redox couple undergoing a single-electron transfer reactions of the form $O + e^- \rightarrow R$ at an electrode surface were developed by Butler and Volmer [192]. The expression for the potential dependence for the reduction of the redox couple is given by equation 9:

$$r_r = k^0 \exp\left[-\alpha f\left(E-E^{0'}\right)\right] C_O(0,t) \qquad (9)$$

and the expression for oxidation of the redox couple is given by equation 10:

$$r_o = k^0 \exp\left[(1-\alpha) f\left(E-E^{0'}\right)\right] C_R(0,t) \qquad (10)$$

where r_r and r_o are the rates of reduction and oxidation, respectively, α is the transfer coefficient, k^0 is the standard rate constant, f is defined as F/RT, where F is Faraday's constant, R is the gas constant, T is the absolute temperature, E is the applied potential, $E^{0'}$ is the formal potential of the redox couple, and $C_O(0,t)$ and $C_R(0,t)$ are the concentrations of the oxidized and the reduced form of the redox couple at the electrode surface, respectively. When the potential of the working electrode approaches the formal potential of the redox couple, the rate of electron transfer between the electrode and the redox couple will increase. This is due to the increasing thermodynamic driving force for the heterogeneous reaction. As the potential of the electrode goes past the formal potential of the redox couple, the reaction rate will continue to increase until the reaction becomes diffusion-limited, and a peak current occurs. Determining the boundary value solution to Fick's law, assuming a completely reversible redox couple yielded the expression for the peak current, i_p, for a cathodic potential sweep, equation 11:

$$i_p = 2.69\times10^5 n^{3/2} A D_O^{1/2} C_O^* v^{1/2} \qquad (11)$$

where n is the number of electrons transferred, A is the working area, D_O is the diffusion coefficient, C* is the bulk concentration of the redox couple, and v is the scan rate. Cyclic voltammetry can be used to back-calculate unknown variables in the system.

4.3 Results and Discussion

4.3.1 AFM

The AFM images collected over 25 μm^2 areas (Figure 4.13, top) allowed for approximate determination of the surface coverage of peptide and LPETG-PsaE PSI on the gold substrates. From the AFM images, the average height for the samples with different peptide concentrations and PSI was determined. The cleaned bare gold (Figure 4.13, top left) substrates yielded surface features with an average height of 1.4 nm. The AFM analysis of different peptide concentrations (100 nM – 500 mM) on gold showed that overall, addition of the peptide resulted in uniform distribution of the peptide yielding a consistent average height of the surface features of 2.6 nm. With the addition of LPETG-modified PSI, it was expected that the surface would yield an average feature height of approximately 13 nm, where the average height of features on bare gold is 1 nm, the LPETGGGC linkage contributes another ~2 nm, and the height of the protein, ~10 nm, which was previous observed with SANS [193]. The observed average height of the SML PSI surface was 10.2 nm. The shorter observed height compared to the theoretically expected height may be due to the flexibility of the peptide linkage or the size of the protein, which may mask the height contributed by the sortase linkage. In the range of 100 mM – 500 mM peptide, the resulting samples with SML mutant PSI appeared as in Figure 4.13 (right) and above 500 mM peptide yielded surfaces that appeared to have aggregated PSI due to the appearance of protein islands (Figure 4.13, bottom). With maximum heights of 700 nm, the features that appear in the bottom figures of Figure 4.13, suggest that multilayers of PSI are forming with increased peptide concentration possibly due to peptide stacking and are not appropriate for studying the behavior of a PSI monolayer.

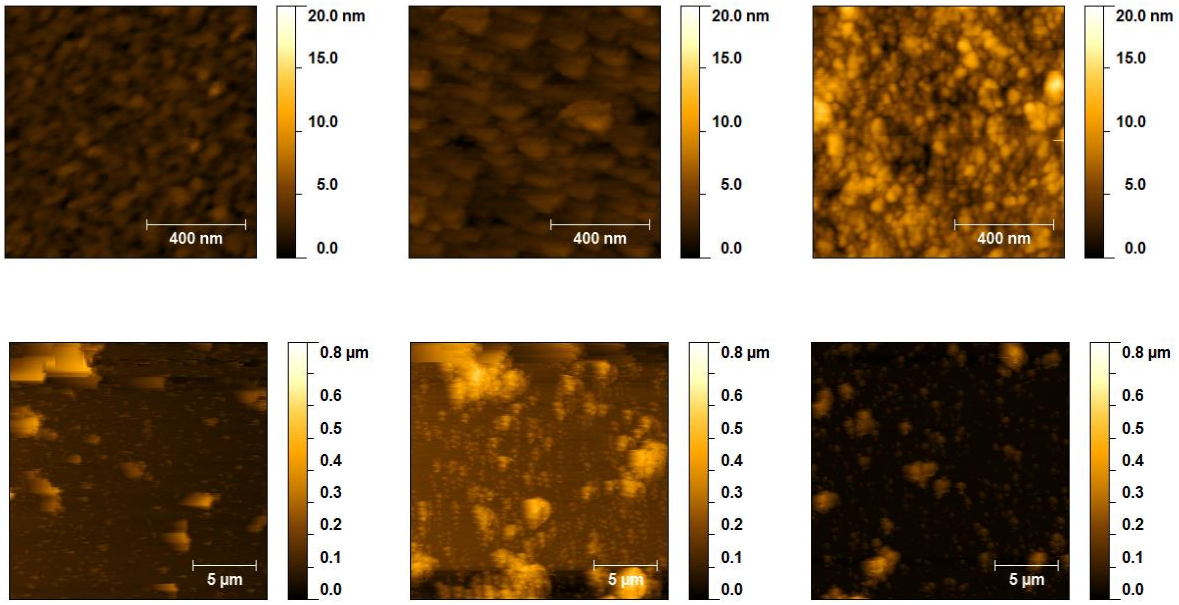

Figure 4.13. AFM images of bare gold substrate (top left), 100 µM GGG peptide on gold (top middle), LPETG-PSI on 100 µM GGG-peptide gold ligated via SML (top right), LPETG-PSI on 500 µM GGG-peptide on gold ligated via SML (bottom left), LPETG-PSI on 1 mM GGG-peptide on gold ligated via SML (bottom middle), and LPETG-PSI on 3 mM GGG-peptide on gold ligated via SML (bottom right).

4.3.2 Photochronoamperometry

In vivo, redox reactions across PSI are aided by diffusible mediators; cytochrome c_6 on the donor side to P_{700} and ferredoxin on the acceptor side from the iron sulfur cluster F_B. For *in vitro* applications, after PSI has been purified from the thylakoid membrane, such as deposition onto electrodes for electricity production, continuous electron transfer is maintained by either an electron acceptor or donor, depending on the orientation of PSI. In this work, potassium ferrocyanide ($K_4Fe(CN)_6$, E_m ~ 200 mV vs. SCE) was used as an electron donor to PSIs oriented with their P700 reaction sites adjacent to the bulk electron mediator solution to reduce P_{700+} back to P_{700}, referred to as the stromal side down orientation. The terminal electron acceptor was a gold electrode which oxidized F_B. $K_4Fe(CN)_6$ was selected as an electron donor for this work

because its electron donation is light-independent and compatibility of its potential to donate to oxidized P_{700}^{+}.

Determination of the orientation of PSI on the surface was done by performing photochronoamperometry measurements with PSI-gold samples in either 200 µM potassium ferri- (K_3) or ferro- (K_4) cyanide, with 100 mM KCl and pH 7 PBS. This particular redox pair was utilized for our electrochemical analysis because preliminary amperometry experiments with DCIP/DCIP-ascorbate yielded current densities on the order of ~60 nA/cm^2 (data not shown) and were deemed less compatible with our system. PSI behaves like a diode since electron flow in PSI is unidirectional. Therefore the direction of the electron flow/current can be probed by determining which species of the soluble mediator (potassium ferri- or ferro-cyanide) enables current flow. A cathodic current was designated as flow of electrons from the gold electrode through PSI to an electron accepting species in solution while an anodic current was designated as flow of electrons into the gold electrode from an electron donating species through PSI in solution. Under this designation, cathodic current was assumed to be the result of PSI with the P_{700} reaction site proximal (lumenal side down, Figure 4.14A) to the electrode while an anodic current was the result of the PSI oriented such that the F_B clusters were proximal (stromal side down, Figure 4.14B) to the gold surface due to the sortase ligation anchoring the PSI trimer on all three PsaE subunits. It was expected that a significant net current response would occur in the presence of ferrocyanide (reduced mediator/electron donor). In contrast, in the presence of ferricyanide (oxidized mediator/electron acceptor) it was expected that little to no current would be produced, since ferricyanide is unable to donate electrons to P_{700} in the assumed orientation.

A summary of current density produced by LPETG-PsaE and WT PSI SML control electrodes are summarized in Table 4.2. As expected, the controls of the bare gold surface

cleaned with piranha solution, with peptide alone, sortase enzyme alone, peptide and sortase, and mutant PSI produced no current or current that is below the detection limit of the potentiostat. The wild type PSI alone produced very little current (~7 nA/cm^2). Interestingly, in the case of modified PSI and wild type PSI electrodes prepared with sortase, produced current density in the range expected for PSI monolayers (< ~100 nA/cm^2) with unknown and undirected orientation.

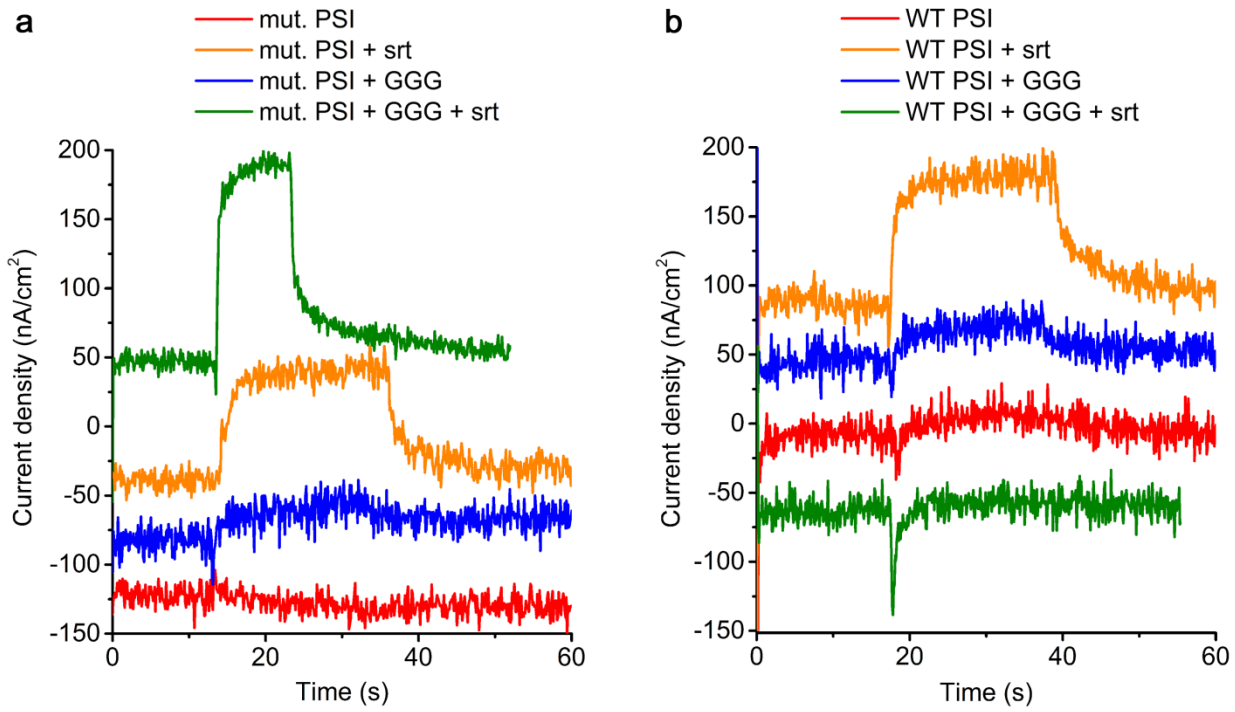

Figure 4.14. Sample photocurrents generated by mutant and wild-type PSI SML controls under OCP using $K_4Fe(CN)_6$ as an electron donor after one light cycle. (a) Mutant PSI SML controls. (b) WT PSI SML controls.

This is surprising because analysis of the PSI complex reveals no regions containing a sequence similar to the sortase recognition sequence where the enzyme could potentially cleave the protein nor is there a presence of the coupling reaction compliment. Therefore sortase may be exhibiting adhesive-like behavior in this system, potentially due to its cysteine active site, where sulfhydryl interactions may be occurring between the sortase and the gold surface. In addition, when PSI is

incubated with surfaces decorated with the tri-glycine peptide in the absence of sortase, a small amount of current is produced (~20 nA/cm^2). This suggests that the presence of peptide promotes non-specific binding of protein to the surface. However, under the SML conditions in presence of GGG peptide, sortase, and LPETG-PSI the current density is significantly enhanced over the other control cases. This indicates that the sortase coupling reaction has a significant influence on the orientation of the PSI on the surface and therefore the current density. With the oxidized redox species, $K_3Fe(CN)_6$ the control cases produced no current under illumination (data not shown).

From the conditions tested, enhanced electron transfer was observed in the presence of 200 µM $K_4Fe(CN)_6$, with 100 mM KCl and pH 7 PBS, LPETG-PSI ligated to the surfaces via SML, on gold incubated with 100 mM GGG-peptide. There was significantly higher current densities compared to $K_3Fe(CN)_6$ as the redox mediator (Figure 4.13), as expected, which shows that the use of SML aids in the control of orienting protein in a uniform manner. The photocurrents measured in the sortase-mediated ligation films with $K_3Fe(CN)_6$ as an electron acceptor yielded an average current density of 10.7 nA/cm^2 with 95% lower and upper bound confidence intervals of 3.8 nA/cm^2 and 17.6 nA/cm^2 respectively vs $K_4Fe(CN)_6$ as an electron donor for the presumed protein orientation (stromal side down) with a current density of 159.0 nA/cm^2 with 95% lower and upper bound confidence intervals of 120.7 nA/cm^2 and 197.2 nA/cm^2, respectively (Figure 4.15). The ratio of the averaged current density from each electron donor (14.9 $K_4Fe(CN)_6$:$K_3Fe(CN)_6$) allowed for the calculation of the percentage of PSI in the stromal side or lumenal side proximal to the surface orientation calculated by equation 12,

$$\frac{j_{K_4Fe(CN)_6}}{j_{K_3Fe(CN)_6}} = \text{ratio of current densities} = \frac{100 - x}{x} \quad (12)$$

where $j_{K_4Fe(CN)_6}$ is the current density produced using $K_4Fe(CN)_6$ as an electron donor and $j_{K_3Fe(CN)_6}$ is the current density produced using $K_3Fe(CN)_6$ as an electron acceptor and x is the unknown percentage of the lumenal side proximal orientation [194]. This calculation yielded a percent distribution of 94% stromal side proximal to the surface and 6% lumenal side proximal to the surface. This distribution shows that the majority of the PSI is oriented stromal side down by the sortase linkage.

Table 4.2. Summary of averaged current density with standard deviation produced by LPETG-PsaE and WT PSI SML control electrodes in the presence or absence of 100 µM GGG peptide and/or sortase using $K_4Fe(CN)_6$ as the electron donor during photochronoamperometry.*= below the detection limit

Description	**J (nA/cm^2) $K_4Fe(CN)_6$**
bare gold	0*
+GGG	0*
+srt	0*
+peptide +srt	0*
+LPETG-PSI	6.7 ± 5.2
+srt +LPETG-PSI	79.7 ± 2.2
+GGG +LPETG-PSI	33.7 ± 22.5
+GGG +srt +LPETG-PSI	202.9 ± 52.6
+WT PSI	11.3 ± 11.7
+srt +WT PSI	53.5 ± 15.2
+GGG +WT PSI	21.3 ± 3.6
+GGG +srt + WT PSI	73.4 ± 16.3

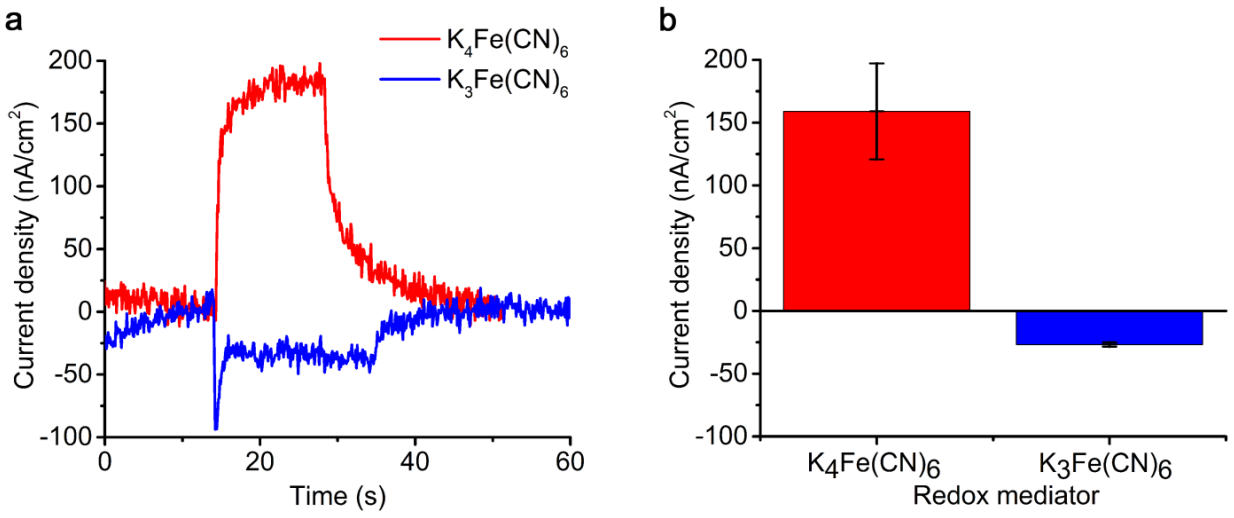

Figure 4.15. Sample raw and averaged current density data for mutant PSI on gold. (a) Raw photochronoamperometry data for photo-induced current production of PSI ligated by sortase to a 100 µM GGG peptide gold surface in the presence of $K_4Fe(CN)_6$ or $K_3Fe(CN)_6$. (b) Average current density produced by mutant PSI ligated to 100 µM GGG peptide gold substrates with sortase in the presence of $K_4Fe(CN)_6$ or $K_3Fe(CN)_6$ under illumination shown with 95% confidence intervals.

4.4 Conclusion

We have demonstrated enzymatic coupling of PSI to peptide-decorated gold using sortase-mediated ligation can be used to create uniformly oriented monolayers. The bioactivity of the ligated PSI was verified by photo-induced current production using photochronoamperometry. The photocurrents, which were generated from PSI particles with different orientations in the monolayer, can be effectively measured by the addition of different mediators, which allowed for the PSI orientation distribution on the gold electrode to be calculated. Using sortase mediated ligation in this work has shown to be helpful in controlling the orientation of PSI. Further studies in optimizing the sortase mediated ligation of PSI monolayers on gold are necessary and could give greater insight into controlling the morphology of the surfaces in order to enhance the current density in monolayers and in the future, multilayers of PSI. The results observed need to be further explored with LPETG-modified PSI

on its other subunits to gain more understanding into the relationship between protein orientation, distance from the surface, and observed current density of PSI monolayers.

5. CONCLUSION AND FUTURE DIRECTION

5.1 Conclusion

The results presented in this dissertation have demonstrated the versatility of photosystem I, a naturally abundant and highly functional photoactive protein complex for integration into systems for photobio-hydrogen and photoelectrochemical systems.

We investigated the effects of light intensity, platinum salt concentrations, and temperature during the platinization process for photo-dependent H_2 production and the subsequent hydrogen yield from platinized PSI particles. Fraction factorial design was used to screen a series of experiments to determine the effect of light quality (white vs. red) on the rate of H_2 production. The mean total yield using red light during platinization was marginally higher than the yield for white light. Application of RSM allowed us to determine the interaction between platinum salt concentration and temperature during platinization, and showed their significant influence on total H_2 yield. This study allowed us to identify the parameters and conditions required for this system. Optimal H_2 photo-production was observed at a light intensity of 240 $\mu E/m^2/s$, platinum salt concentration of 638 μM, and temperature of 31°C during the platinization process. Yielding 8.0 $\mu mol\ H_2$/mg chl a/h, the highest value achieved for this system.

The solution structure of detergent-associated PSI preparations was studied using SANS and produced results that were not observed previously. Analysis of the data with and without the scattering contribution of DDM suggested detergent exists primarily as a belt surrounding the transmembrane domains of the protein complex and does not interact with the stromal or lumenal surfaces of the trimer. In our initial analysis of the PSI-detergent system, we assumed a particle of arbitrary shape, rather than a time intensive trial and error and iterative approach to fine tune the proper model for our system. This study showed that the typical schematics for membrane

proteins reconstituted in surfactants/solution are often shown to be contained within a uniformly oriented detergent or lipid structure are oversimplified and the protein-detergent interactions are important to study to better understand the behavior of the protein in its native environment and how they will behave in *in vitro* applications.

We also demonstrated that photocurrent production from monolayers of PSI on conductive surfaces could be improved by controlling the orientation of the reaction centers so they were stromal side down (with F_B proximal to the electrode) and therefore enhance the quantity of useful electron transfer. We utilized the highly specific enzymatic coupling reaction performed by srt A to covalently link PSI to a peptide-decorated gold surface. Though several LPETG PSI mutants have been made, only the PsaE-LPETG has been identified to be completely free of wild type genomic DNA and therefore we can assume the trimeric PSI is expressed with 3 LPETG tags available for sortase coupling. With its highly exposed C-termini on the stromal hump, this mutant was likely to be oriented to the surface with the F_B iron sulfur cluster proximal to the electrode. We were able to confirm the bioactivity of the ligated PSI by photo-induced current production using photochronoamperometry and we improved the current density for PSI monolayer-gold systems, which typically produce <100 nA/cm^2 of current, to within the range of 150 – 200 nA/cm^2 of current. The use of sortase mediated ligation in this work has shown to be helpful in controlling the orientation of PSI.

5.2 Future Direction

While considerable progress has been made using PSI for both hydrogen and current producing systems, many obstacles still prevent these biologically-based technologies to be implemented for large-scale use or economical alternatives to conventional energy sources. For

the hydrogen applications, it still remains to be seen if the hydrogen produced can be successfully captured and in pure enough quality to be useful. Currently the biologically-based hydrogen systems using hydrogenase have very short lifetimes and are not stable due to their intolerance to oxygen, leading to unsustainable hydrogen evolution. The metal-catalyzed systems use rare and expensive metals, and though they can sustain hydrogen evolution for extended periods of time, they are likely to be uneconomical in the long run since they produce only modest amounts of hydrogen compared to current industrially used methods. In terms of the photocurrent producing systems, the power output and photo-conversion efficiency of these systems must be increased substantially in order for PSI-based energy conversion technologies to become competitive with current photovoltaic technologies. Figure 5.1 shows the progress to date of PSI-based systems for photovoltaic energy conversion with impressive advances in current density within the last 10 years, therefore one could expect for this progress to continue and eventually become a cheap and viable option for a niche community.

Another aspect of the present systems that must be improved in order to increase their efficiency is the ability of PSI to absorb light at useful wavelengths. Chlorophyll is able to absorb wavelengths in the red and blue regions of the visible spectrum, but has a relatively low absorbance in the yellow and green regions. This is a constraint of PSI-based devices that is detrimental for the purpose of harnessing solar energy, because the majority of solar photons have wavelengths in this region. This problem has been approached by a few groups who have shown pigments that absorb in the green region and emit in the red region can be used to increase the sensitivity of the antenna complexes of PSI to green photons [195] and proposals to integrate the light-harvesting complexes from a conglomerate of photosynthesizing species to better

capture useful wavelengths of light for increased energy converting efficiencies [196]. This enhancement could be carried over into the hydrogen producing systems as well.

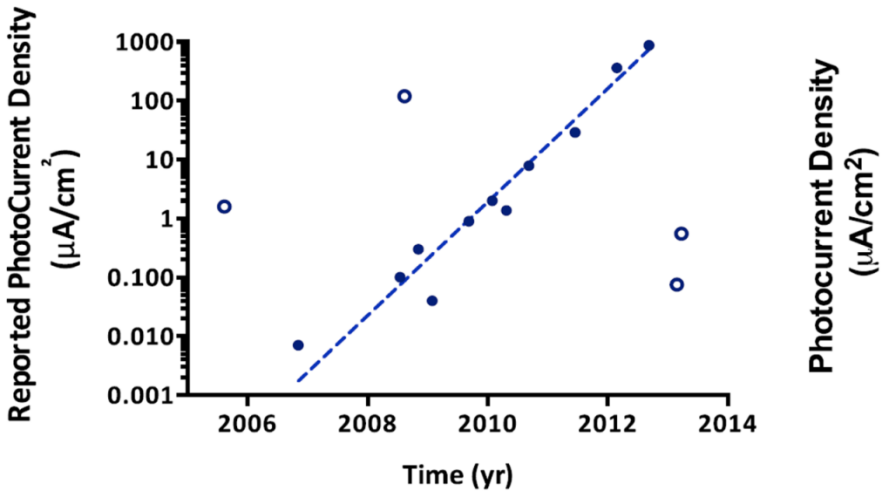

Figure 5.1 Progress of PSI-generated photocurrent to date, adapted from Nguyen and Bruce [62]. The plot shows the advancement in photocurrent density produced in studies between 2005 and 2013, where a 10 fold increase in rate ($\mu A/cm^2$) is seen per year. (Reprinted from Biochimica et Biolphysica Acta, Vol 1837/Issue 9, Khoa Nguyen and Barry Bruce, Growing green electricity: Progress and strategies for use of Photosystem I for sustainable photovoltaic energy conversion, Pages 1553–1566, 2014, with permission from Elsevier, License Number: 3510910960991. http://www.sciencedirect.com/science/article/pii/S000527281300234X)

Further studies in optimizing the sortase mediated ligation of PSI monolayers on gold are necessary and could give greater insight into controlling the morphology of the surfaces in order to enhance the current density in monolayers and in the future, multilayers of PSI. The results observed need to be further explored with LPETG-modified PSI on its other subunits to gain more understanding into the relationship between protein orientation, distance from the surface, and observed current density of PSI monolayers. However, with the vast improvement in current density production seen from multilayers of PSI, it would be better to attempt to use SML to stack PSIs in an oriented manner. The ability of sortase to pre-assemble PSI in monolayers to a

conductive surface as shown in Chapter 4 could be a preliminary step before adding molecular wires that could directly transfer electrons from the F_B iron sulfur cluster to the gold surface via thiol chemistry, which would likely enhance the current density significantly, because sortase orients the PSI ~95% uniformly. Furthermore, applying the sortase-pre-assembly method could also be applied to a PSI-hydrogenase system to enhance the electron transfer/hydrogen production already seen by Grimme and Lubner [33, 197] since pre-assembling a PSI-hydrogenase fusion would eliminate PSI-PSI or hydrogenase-hydrogenase homodimers, which decreases the efficient formation of PSI-hydrogenase fusions.

While great progress in the design and construction of PSI-based systems has been described in this work, the full potential of the highly efficient protein complex has yet to be realized. Improvements to the systems presented could be achieved by identifying more effective electrochemical mediators, enhancing the light absorbing capabilities of PSI, eliminating the diffusional limitations between PSI and a surface or other redox proteins like hydrogenase. These improvements should be embarked on to move toward PSI-based energy conversion systems that are competitive economically and in efficiency of energy conversion.

REFERENCES

1. U.S.Energy Information Administration, *International Energy Outlook 2013*. 2013: Washington, DC.
2. C. Le Quere, et al., *Trends in the sources and sinks of carbon dioxide.* Nature Geosci, 2009. **2**(12): p. 831-836.
3. International Energy Agency, *Solar Energy Perspectives*. 2011.
4. IPCC, *Climate Change 2013: The Physical Science Basis. Contribution of Working Group I to the Fifth Assessment Report of the Intergovernmental Panel on Climate Change*, T.F. Stocker, D. Qin, G.-K. Plattner, M. Tignor, S.K. Allen, J. Boschung, A. Nauels, Y. Xia, V. Bex and P.M. Midgley, Editor. 2013: New York, NY.
5. N. Nelson, *Plant Photosystem I The Most Efficient Nano-Photochemical Machine.* Journal of Nanoscience and Nanotechnology, 2009. **9**(3): p. 1709-1713.
6. A. Badura, et al., *Light-Driven Water Splitting for (Bio-)Hydrogen Production: Photosystem 2 as the Central Part of a Bioelectrochemical Device.* Photochemistry and Photobiology, 2006. **82**(5): p. 1385-1390.
7. H. Krassen, et al., *Photosynthetic Hydrogen Production by a Hybrid Complex of Photosystem I and [NiFe]-Hydrogenase.* ACS Nano, 2009. **3**(12): p. 4055-4061.
8. P.N. Ciesielski, Cliffel, D.E., and Jennings, G.K., *Kinetic Model of the Photocatalytic Effect of a Photosystem I Monolayer on a Planar Electrode Surface.* Journal of Physical Chemistry A, 2011. **115**(15): p. 3326-3334.
9. G.D. Scholes, et al., *Lessons from nature about solar light harvesting.* Nat Chem, 2011. **3**(10): p. 763-774.
10. I.J. Iwuchukwu, et al., *Optimization of photosynthetic hydrogen yield from platinized photosystem I complexes using response surface methodology.* International Journal of Hydrogen Energy, 2011. **36**(18): p. 11684-11692.
11. C.E. Lubner, et al., *Wiring Photosystem I for Direct Solar Hydrogen Production.* Biochemistry, 2009. **49**(3): p. 404-414.
12. P. Jordan, et al., *Three-dimensional structure of cyanobacterial photosystem I at 2.5 angstrom resolution.* Nature, 2001. **411**(6840): p. 909-917.
13. J.H. Golbeck, *Structure and Function of Photosystem I.* Annual Review of Plant Physiology and Plant Molecular Biology, 1992. **43**(1): p. 293-324.
14. A.L. Zilber and Malkin, R., *Organization and Topology of Photosystem I Subunits.* Plant Physiology, 1992. **99**(3): p. 901-911.
15. A.H. Robert C. Ford, *Investigation of the structure of trimeric and monomeric photosystem I reaction centre complexes.* EMBO Journal, 1988. **7**(8): p. 2287 - 2293.
16. I. Grotjohann and Fromme, P., Photosyn. Res., 2005. **2005**: p. 51.
17. D. Mukherjee, May, M., and Khomami, B., *Detergent-protein interactions in aqueous buffer suspensions of Photosystem I (PS I).* Journal of Colloid and Interface Science, 2011. **358**(2): p. 477-484.
18. J.H. Golbeck, *Photosystem I: The Light-Driven Plastocyanin:Ferredoxin Oxidoreductase*. 2006.
19. K. Brettel, *Electron transfer and arrangement of the redox cofactors in photosystem I.* Biochimica et Biophysica Acta, Bioenergetics, 1997. **1318**(3): p. 322-373.
20. K. Brettel and Leibl, W., *Electron transfer in photosystem I.* Biochimica et Biophysica Acta, Bioenergetics, 2001. **1507**(1–3): p. 100-114.

21. J.H. Golbeck, *Photosynthetic Electron Transfer: So Little Time, So Much to Do*, in *Energy Transduction in Membranes*, W.A. Cramer, Editor. 2003, American Biophysical Society.
22. P. Rice, Longden, I., and Bleasby, A., *EMBOSS: the European Molecular Biology Open Software Suite.* Trends in genetics : TIG, 2000. **16**(6): p. 276-277.
23. E. Greenbaum, Science, 1985. **230**: p. 1373.
24. J.W. Lee, Lee, I., and Greenbaum, E., *Platinization: a novel technique to anchor photosystem I reaction centres onto a metal surface at biological temperature and pH.* Biosensors and Bioelectronics, 1996. **11**(4): p. 375-387.
25. J.W. Lee, et al., Energy & Fuels, 1994. **8**: p. 770.
26. E. Greenbaum, *Interfacial photoreactions at the photosynthetic membrane interface: an upper limit for the number of platinum atoms required to form a hydrogen-evolving platinum metal catalyst.* The Journal of Physical Chemistry, 1988. **92**(16): p. 4571-4574.
27. J.W. Lee, et al., *Photosynthetic water splitting: in situ photoprecipitation of metallocatalysts for photoevolution of hydrogen and oxygen.* Energy & Fuels, 1994. **8**(3): p. 770-773.
28. J.W. Lee, Lee, I., and Greenbaum, E., *Imaging nanometer metallocatalysts formed by photosynthetic deposition of water-soluble transition-metal compounds.* The Journal of Physical Chemistry B, 2005. **109**(12): p. 5409-5413.
29. J.F. Millsaps, et al., *Nanoscale Photosynthesis: Photocatalytic Production of Hydrogen by Platinized Photosystem I Reaction Centers*¶. Photochemistry and Photobiology, 2001. **73**(6): p. 630-635.
30. B.R. Evans, et al., *Enhanced Photocatalytic Hydrogen Evolution by Covalent Attachment of Plastocyanin to Photosystem I.* Nano Letters, 2004. **4**(10): p. 1815-1819.
31. I.J. Iwuchukwu, et al., *Self-organized photosynthetic nanoparticle for cell-free hydrogen production.* Nat Nano, 2010. **5**(1): p. 73-79.
32. R.A. Grimme, et al., *Photosystem I/Molecular Wire/Metal Nanoparticle Bioconjugates for the Photocatalytic Production of H_2.* Journal of the American Chemical Society, 2008. **130**(20): p. 6308-6309.
33. R.A. Grimme, Lubner, C.E., and Golbeck, J.H., *Maximizing H_2 production in Photosystem I/dithiol molecular wire/platinum nanoparticle bioconjugates.* Dalton Transactions, 2009(45): p. 10106-10113.
34. P.M. Vignais and Billoud, B., *Occurrence, classification, and biological function of hydrogenases: an overview*. Chemical Reviews (Washington, DC, United States), 2007. **107**(10): p. 4206-4272.
35. J.C. Fontecilla-Camps, et al., *Structure/function relationships of [NiFe]-and [FeFe]-hydrogenases.* Chemical Reviews (Washington, DC, United States), 2007. **107**(10): p. 4273-4303.
36. J.C. Fontecilla-Camps, et al., *Structure–function relationships of anaerobic gas-processing metalloenzymes.* Nature, 2009. **460**(7257): p. 814-822.
37. W. Lubitz, et al., *Hydrogenases.* Chemical Reviews (Washington, DC, United States), 2014. **114**(8): p. 4081-4148.
38. J. Fritsch, Lenz, O., and Friedrich, B., *Structure, function and biosynthesis of O2-tolerant hydrogenases.* Nat Rev Micro, 2013. **11**(2): p. 106-114.
39. H. Mctavish, *Hydrogen evolution by direct electron transfer from photosystem I to hydrogenases.* Journal of Biochemistry (Tokyo, Japan), 1998. **123**(4): p. 644-649.

40. M. Ihara, et al., *Light-driven Hydrogen Production by a Hybrid Complex of a [NiFe]-Hydrogenase and the Cyanobacterial Photosystem I.* Photochemistry and Photobiology, 2006. **82**(3): p. 676-682.
41. M. Ihara, et al., *Photoinduced Hydrogen Production by Direct Electron Transfer from Photosystem I Cross-Linked with Cytochrome c3 to [NiFe]-Hydrogenase.* Photochemistry and Photobiology, 2006. **82**(6): p. 1677-1685.
42. T. Mehari, et al., *Modified Ligands to F_A and F_B in Photosystem II. Structural constraints for the formation of iron-sulfur clusters in free and rebound PsaC.* Journal of Biological Chemistry, 1995. **270**(47): p. 28108-28117.
43. Y.-S. Jung, et al., *Modified ligands to F_A and F_B in Photosystem I proposed chemical rescue of a [4Fe-4S] cluster with an external thiolate in alanine, glycine, and serine mutants of PsaC.* Journal of Biological Chemistry, 1996. **271**(49): p. 31135-31144.
44. M.L. Antonkine, et al., *Chemical rescue of a site-modified ligand to a [4Fe–4S] cluster in PsaC, a bacterial-like dicluster ferredoxin bound to Photosystem I.* Biochimica et Biophysica Acta (BBA)-Bioenergetics, 2007. **1767**(6): p. 712-724.
45. H. Krassen, et al., *Immobilization of the [FeFe]-hydrogenase CrHydA1 on a gold electrode: Design of a catalytic surface for the production of molecular hydrogen.* Journal of Biotechnology, 2009. **142**(1): p. 3-9.
46. C.E. Lubner, et al., *Solar hydrogen-producing bionanodevice outperforms natural photosynthesis.* Proceedings of the National Academy of Sciences, 2011. **108**(52): p. 20988-20991.
47. I. Lee, Lee, J.W., and Greenbaum, E., *Biomolecular Electronics: Vectorial Arrays of Photosynthetic Reaction Centers.* Physical Review Letters, 1997. **79**(17): p. 3294-3297.
48. B. Munge, et al., *Electron Transfer Reactions of Redox Cofactors in Spinach Photosystem I Reaction Center Protein in Lipid Films on Electrodes.* Journal of the American Chemical Society, 2003. **125**(41): p. 12457-12463.
49. R. Das, et al., *Integration of Photosynthetic Protein Molecular Complexes in Solid-State Electronic Devices.* Nano Letters, 2004. **4**(6): p. 1079-1083.
50. N. Terasaki, et al., *Fabrication of novel photosystem I–gold nanoparticle hybrids and their photocurrent enhancement.* Thin Solid Films, 2006. **499**(1): p. 153-156.
51. N. Terasaki, et al., *Plugging a Molecular Wire into Photosystem I: Reconstitution of the Photoelectric Conversion System on a Gold Electrode.* Angewandte Chemie International Edition, 2009. **48**(9): p. 1585-1587.
52. N. Terasaki, et al., *Bio-photosensor: Cyanobacterial photosystem I coupled with transistor via molecular wire.* Biochimica et Biophysica Acta (BBA) - Bioenergetics, 2007. **1767**(6): p. 653-659.
53. L. Frolov, et al., *Fabrication of a Photoelectronic Device by Direct Chemical Binding of the Photosynthetic Reaction Center Protein to Metal Surfaces.* Advanced Materials (Weinheim, Germany), 2005. **17**(20): p. 2434-2437.
54. L. Frolov, et al., *Fabrication of Oriented Multilayers of Photosystem I Proteins on Solid Surfaces by Auto-Metallization.* Advanced Materials (Weinheim, Germany), 2008. **20**(2): p. 263-266.
55. D. Gerster, et al., *Photocurrent of a single photosynthetic protein.* Nat Nano, 2012. **7**(10): p. 673-676.

56. M. Ciobanu, et al., *Electrochemistry and photoelectrochemistry of photosystem I adsorbed on hydroxyl-terminated monolayers.* Journal of Electroanalytical Chemistry, 2007. **599**(1): p. 72-78.
57. B.S. Ko, et al., *Effect of Surface Composition on the Adsorption of Photosystem I onto Alkanethiolate Self-Assembled Monolayers on Gold.* Langmuir, 2004. **20**(10): p. 4033-4038.
58. C.J. Faulkner, et al., *Rapid Assembly of Photosystem I Monolayers on Gold Electrodes.* Langmuir, 2008. **24**(16): p. 8409-8412.
59. D. Mukherjee, et al., *Controlling the Morphology of Photosystem I Assembly on Thiol-Activated Au Substrates.* Langmuir, 2010. **26**(20): p. 16048-16054.
60. D. Mukherjee, May, M., and Khomami, B., *Detergent–protein interactions in aqueous buffer suspensions of Photosystem I (PS I).* Journal of Colloid and Interface Science, 2011. **358**(2): p. 477-484.
61. A.K. Manocchi, et al., *Photocurrent Generation from Surface Assembled Photosystem I on Alkanethiol Modified Electrodes.* Langmuir, 2013.
62. K. Nguyen and Bruce, B.D., *Growing green electricity: Progress and strategies for use of Photosystem I for sustainable photovoltaic energy conversion.* Biochimica et Biophysica Acta (BBA) - Bioenergetics, 2014. **1837**(9): p. 1553-1566.
63. G. Leblanc, et al., *Enhanced Photocurrents of Photosystem I Films on p-Doped Silicon.* Advanced Materials (Weinheim, Germany), 2012. **24**(44): p. 5959-5962.
64. P.N. Ciesielski, et al., *Functionalized Nanoporous Gold Leaf Electrode Films for the Immobilization of Photosystem I.* ACS Nano, 2008. **2**(12): p. 2465-2472.
65. P.N. Ciesielski, et al., *Enhanced Photocurrent Production by Photosystem I Multilayer Assemblies.* Advanced Functional Materials, 2010. **20**(23): p. 4048-4054.
66. P.N. Ciesielski, et al., *Photosystem I – Based biohybrid photoelectrochemical cells.* Bioresource Technology, 2010. **101**(9): p. 3047-3053.
67. A. Mershin, et al., *Self-assembled photosystem-I biophotovoltaics on nanostructured TiO2 and ZnO.* Sci. Rep., 2012. **2**.
68. R.K. Le, et al., *Sortase-mediated Ligation of PsaE-modified Photosystem I from Synechocystis sp. PCC 6803 to a Conductive Surface for Enhanced Photocurrent Production on a Gold Electrode.* Langmuir (submitted), 2014.
69. W. Mampe, et al., *Neutron lifetime measured with stored ultracold neutrons.* Physical Review Letters, 1989. **63**(6): p. 593-596.
70. S. Arzumanov, et al., *Neutron life time value measured by storing ultracold neutrons with detection of inelastically scattered neutrons.* Physics Letters B, 2000. **483**(1–3): p. 15-22.
71. A.J. Berry and James, M., *Refinement of hydrogen positions in synthetic hydroxyl-clinohumite by powder neutron diffraction.* American Mineralogist, 2001. **86**(1-2): p. 181-184.
72. T. Gutberlet, Heinemann, U., and Steiner, M., *Protein crystallography with neutrons-status and perspectives.* Acta Crystallographica Section D: Biological Crystallography, 2001. **57**(2): p. 349-354.
73. J. Katsaras, et al., *Small-Angle Neutron Scattering and Biomolecules.* Physics in Canada, 2006.
74. B. Jacrot, *The study of biological structures by neutron scattering from solution.* Reports on progress in physics, 1976. **39**(10): p. 911.

75. J. Witz, *Contrast variation of the small-angle neutron scattering of globular particles: the influence of hydrogen exchange.* Acta Crystallographica Section A: Foundations of Crystallography, 1983. **39**(5): p. 706-711.
76. N. Kučerka, et al., *Bilayer thickness in unilamellar phosphatidylcholine vesicles: small-angle neutron scattering using contrast variation.* Physica B: Condensed Matter, 2004. **350**(1): p. E639-E642.
77. D.I. Svergun and Koch, M.H., *Small-angle scattering studies of biological macromolecules in solution.* Reports on progress in physics, 2003. **66**(10): p. 1735.
78. M. Agamalian, Wignall, G., and Triolo, R., *Optimization of a Bonse-Hart ultra-small-angle neutron scattering facility by elimination of the rocking-curve wings.* Journal of Applied Crystallography, 1997. **30**(3): p. 345-352.
79. C. Muzny, et al., *An ultra-small-angle neutron scattering study of the restructuring of sheared colloidal silica gels.* Journal of Physics: Condensed Matter, 1999. **11**(26): p. L295.
80. M. Bee, *Quasielastic Neutron Scattering: principles and applications in solid state chemistry, biology and material science.* Adam Hilger, Bristol, 1988.
81. A. Guinier and Fournet, G., *Small-Angle Scattering of X-Rays*. 1955.
82. D.A. Jacques and Trewhella, J., *Small-angle scattering for structural biology—Expanding the frontier while avoiding the pitfalls.* Protein Science, 2010. **19**(4): p. 642-657.
83. C. Neylon, *Small angle neutron and X-ray scattering in structural biology: recent examples from the literature.* European Biophysics Journal, 2008. **37**(5): p. 531-541.
84. S. Yang, et al., *A rapid coarse residue-based computational method for X-ray solution scattering characterization of protein folds and multiple conformational states of large protein complexes.* Biophysical Journal, 2009. **96**(11): p. 4449-4463.
85. D. Svergun, *Restoring low resolution structure of biological macromolecules from solution scattering using simulated annealing.* Biophysical Journal, 1999. **76**(6): p. 2879-2886.
86. D. Walther, Cohen, F.E., and Doniach, S., *Reconstruction of low-resolution three-dimensional density maps from one-dimensional small-angle X-ray solution scattering data for biomolecules.* Journal of Applied Crystallography, 2000. **33**(2): p. 350-363.
87. W.T. Heller, et al., *The solution structure of a cardiac troponin C-troponin I-troponin T complex shows a somewhat compact troponin C interacting with an extended troponin I-troponin T component.* Biochemistry, 2002. **41**(52): p. 15654-15663.
88. J.C. Smith, et al., *Structure and Dynamics of Biological Systems: Integration of Neutron Scattering with Computer Simulation*, in *Dynamics of Soft Matter*. 2012, Springer. p. 189-204.
89. H. O'neill, et al., *Small-angle X-ray scattering study of photosystem I - Detergent complexes: Implications for membrane protein crystallization.* Journal of Physical Chemistry B, 2007. **111**(16): p. 4211-4219.
90. P. Thiyagarajan and Tiede, D.M., *Detergent micelle structure and micelle-micelle interactions determined by small-angle neutron-scattering under solution conditions used for membrane-protein crystallization.* Journal of Physical Chemistry, 1994. **98**(40): p. 10343-10351.

91. R. Le, et al., *Determination of a Solution Structure of Photosystem I in n-dodecyl-B-D-maltoside Detergent Using Small-Angle Neutron Scattering and Molecular Dynamics Simulations.* Manuscript in preparation.
92. H. O'neill, et al., *Small-Angle X-ray Scattering Study of Photosystem I−Detergent Complexes: Implications for Membrane Protein Crystallization.* The Journal of Physical Chemistry B, 2007. **111**(16): p. 4211-4219.
93. P. Thiyagarajan and Tiede, D.M., *Detergent micelle structure and micelle-micelle interactions determined by small-angle neutron scattering under solution conditions used for membrane protein crystallization.* The Journal of Physical Chemistry, 1994. **98**(40): p. 10343-10351.
94. H. Hauser, *Short-chain phospholipids as detergents.* Biochimica et Biophysica Acta (BBA) - Biomembranes, 2000. **1508**(1–2): p. 164-181.
95. R.M. Garavito and Ferguson-Miller, S., *Detergents as Tools in Membrane Biochemistry.* Journal of Biological Chemistry, 2001. **276**(35): p. 32403-32406.
96. F. Müh and Zouni, A., *Micelle formation in the presence of photosystem I.* Biochimica et Biophysica Acta (BBA) - Biomembranes, 2008. **1778**(10): p. 2298-2307.
97. D.A. Levary, et al., *Protein-Protein Fusion Catalyzed by Sortase A.* PLoS One, 2011. **6**(4): p. e18342.
98. R. Parthasarathy, Subramanian, S., and Boder, E.T., *Sortase A as a Novel Molecular "Stapler" for Sequence-Specific Protein Conjugation.* Bioconjugate Chemistry, 2007. **18**(2): p. 469-476.
99. L.A. Marraffini, Dedent, A.C., and Schneewind, O., *Sortases and the Art of Anchoring Proteins to the Envelopes of Gram-Positive Bacteria.* Microbiology and Molecular Biology Reviews, 2006. **70**(1): p. 192-221.
100. S.K. Mazmanian, et al., *Staphylococcus aureus sortase, an enzyme that anchors surface proteins to the cell wall.* Science, 1999. **285**(5428): p. 760-763.
101. H. Ton-That, et al., *Purification and characterization of sortase, the transpeptidase that cleaves surface proteins of Staphylococcus aureus at the LPXTG motif.* Proceedings of the National Academy of Sciences, 1999. **96**(22): p. 12424-12429.
102. H. Ton-That, et al., *Anchoring of Surface Proteins to the Cell Wall of Staphylococcus aureus : sortase catalyzed in vitro transpeptidation reaction using LPXTG peptide and NH_2-Gly_3 substrates.* Journal of Biological Chemistry, 2000. **275**(13): p. 9876-9881.
103. S. Samantaray, et al., *Peptide-sugar ligation catalyzed by transpeptidase sortase: a facile approach to neoglycoconjugate synthesis.* Journal of the American Chemical Society, 2008. **130**(7): p. 2132-2133.
104. S. Pritz, et al., *Synthesis of Biologically Active Peptide Nucleic Acid−Peptide Conjugates by Sortase-Mediated Ligation.* The Journal of Organic Chemistry, 2007. **72**(10): p. 3909-3912.
105. T. Matsumoto, et al., *Site-specific tetrameric streptavidin-protein conjugation using sortase A.* Journal of Biotechnology, 2011. **152**(1): p. 37-42.
106. T. Tanaka, et al., *Site-specific protein modification on living cells catalyzed by sortase.* ChemBioChem, 2008. **9**(5): p. 802-807.
107. M.W.-L. Popp, Antos, J.M., and Ploegh, H.L., *Site-Specific Protein Labeling via Sortase-Mediated Transpeptidation*, in *Current Protocols in Protein Science*. 2001, John Wiley & Sons, Inc.

108. T. Sakamoto, et al., *Enzyme-Mediated Site-Specific Antibody− Protein Modification Using a ZZ Domain as a Linker.* Bioconjugate Chemistry, 2010. **21**(12): p. 2227-2233.
109. M.W.-L. Popp and Ploegh, H.L., *Making and Breaking Peptide Bonds: Protein Engineering Using Sortase.* Angewandte Chemie International Edition, 2011. **50**(22): p. 5024-5032.
110. L. Chan, et al., *Covalent attachment of proteins to solid supports and surfaces via Sortase-mediated ligation.* PLoS One, 2007. **2**(11): p. e1164.
111. F. Clow, Fraser, J., and Proft, T., *Immobilization of proteins to biacore sensor chips using Staphylococcus aureus sortase A.* Biotechnology Letters, 2008. **30**(9): p. 1603-1607.
112. S. Tsukiji and Nagamune, T., *Sortase-mediated ligation: a gift from Gram-positive bacteria to protein engineering.* Chembiochem, 2009. **10**(5): p. 787-98.
113. R.G. Kruger, et al., *Analysis of the substrate specificity of the Staphylococcus aureus sortase transpeptidase Srt A.* Biochemistry, 2004. **43**(6): p. 1541-1551.
114. X.Y. Huang, et al., *Kinetic mechanism of Staphylococcus aureus sortase Srt A.* Biochemistry, 2003. **42**(38): p. 11307-11315.
115. H. Balat and Kirtay, E., *Hydrogen from biomass - Present scenario and future prospects.* International Journal of Hydrogen Energy, 2010. **35**(14): p. 7416-7426.
116. M. Hultman, *Back to the future: The dream of a perpetuum mobile in the atomic society and the hydrogen economy.* Futures, 2009. **41**(4): p. 226-233.
117. S.M. Kotay and Das, D., *Biohydrogen as a renewable energy resource - Prospects and potentials.* International Journal of Hydrogen Energy, 2008. **33**(1): p. 258-263.
118. G. Nicoletti, *The hydrogen option for energy: A review of technical, environmental and economic aspects.* International Journal of Hydrogen Energy, 1995. **20**(10): p. 759-765.
119. J.F. Millsaps, et al., *Nanoscale photosynthesis: Photocatalytic production of hydrogen by platinized photosystem I reaction centers.* Photochemistry and Photobiology, 2001. **73**(6): p. 630-635.
120. I. Iwuchukwu, et al., *Self-organized Photosynthetic Nanoparticle for Cell-free Hydrogen Production.* Nature Nanotech., 2009. **5**(1): p. 73-79.
121. Z. Jamil, et al., *Optimization of phototrophic hydrogen production by Rhodopseudomonas palustris PBUM001 via statistical experimental design.* International Journal of Hydrogen Energy, 2009. **34**(17): p. 7502-7512.
122. C.-Y. Chen, et al., *Improved phototrophic H2 production with Rhodopseudomonas palustris WP3-5 using acetate and butyrate as dual carbon substrates.* Bioresource Technology, 2008. **99**(9): p. 3609-3616.
123. C.-Y. Chen, et al., *Enhancing phototrophic hydrogen production of Rhodopseudomonas palustris via statistical experimental design.* International Journal of Hydrogen Energy, 2007. **32**(8): p. 940-949.
124. Y. Mu, Wang, G., and Yu, H.Q., *Response surface methodological analysis on biohydrogen production by enriched anaerobic cultures.* Enzyme and Microbial Technology, 2006. **38**(7): p. 905-913.
125. P. Fromme and Witt, H.T., *Improved isolation and crystallization of photosystem I for structural analysis.* Biochimica et Biophysica Acta (BBA) - Bioenergetics, 1998. **1365**(1–2): p. 175-184.
126. D.D.O. Hall, Rao, K.K., and Biology, I.O., *Photosynthesis*. 1999: Cambridge University Press.

127. B. Andersson and Aro, E.M., *Proteolytic activities and proteases of plant chloroplasts.* Physiologia Plantarum, 1997. **100**(4): p. 780-793.
128. R.L. Burnap, *D1 protein processing and Mn cluster assembly in light of the emerging Photosystem II structure*. Physical Chemistry Chemical Physics, 2004. **6**(20): p. 4803-4809.
129. A. Melis, *Photosystem-II damage and repair cycle in chloroplasts: what modulates the rate of photodamage in vivo?* Trends in Plant Science, 1999. **4**(4): p. 130-135.
130. S. Takahashi, et al., *The Solar Action Spectrum of Photosystem II Damage.* Plant Physiology, 2010. **153**(3): p. 988-993.
131. D.C. Montgomery, *Design and Analysis of Experiments*. 5th ed. 2001, New York: Wiley. 680.
132. C.J. Nachtsheim, et al., *Applied linear regression models.* McGraw-Hill Irwin, 2004.
133. G. Leblanc, et al., *Photoreduction of Catalytic Platinum Particles Using Immobilized Multilayers of Photosystem I.* Langmuir, 2012. **28**(21): p. 7952-7956.
134. M. Ihara, et al., Photochemistry and Photobiology, 2006. **82**: p. 676.
135. L.M. Utschig, et al., *Photocatalytic Hydrogen Production from Noncovalent Biohybrid Photosystem I/Pt Nanoparticle Complexes.* The Journal of Physical Chemistry Letters, 2011. **2**(3): p. 236-241.
136. P. Kiley, et al., *Self-Assembling Peptide Detergents Stabilize Isolated Photosystem Ion a Dry Surface for an Extended Time.* PLoS Biology, 2005. **3**(7): p. e230.
137. W.T. Heller, *Small-angle neutron scattering and contrast variation: a powerful combination for studying biological structures.* Acta Crystallographica Section D-Biological Crystallography, 2010. **66**: p. 1213-1217.
138. D.I. Svergun and Koch, M.H.J., *Advances in structure analysis using small-angle scattering in solution.* Current Opinion in Structural Biology, 2002. **12**(5): p. 654-660.
139. S. Forster, Wenz, E., and Lindner, P., Physical Review Letters, 1996. **77**: p. 95.
140. G.A. Mcconnell, et al., Faraday Discussions, 1994: p. 121.
141. H. Bagger Jorgensen, Olsson, U., and Mortensen, K., Langmuir, 1997. **13**: p. 1413.
142. J. Gau-Racine, et al., Journal of Physical Chemistry B, 2007. **111**: p. 9900.
143. K.J. Mutch, et al., Langmuir, 2008. **24**: p. 3053.
144. U.S. Jeng, et al., Phys. B: Condens. Matter, 2006. **385−386**: p. 865.
145. S. Qian, et al., *The Internal Organization of Mycobacterial Partition Assembly: Does the DNA Wrap a Protein Core?* PLoS One, 2012. **7**(12): p. e52690.
146. E.P. Gogol and Engelman, D.M., *Neutron scattering shows that cytochrome b5 penetrates deeply into the lipid bilayer.* Biophysical Journal, 1984. **46**(4): p. 491-495.
147. G.S. Grest and Kremer, K., *Molecular dynamics simulation for polymers in the presence of a heat bath.* Physical Review A, 1986. **33**(5): p. 3628-3631.
148. K. Kremer and Grest, G.S., *Dynamics of entangled linear polymer melts: A molecular-dynamics simulation.* The Journal of Chemical Physics, 1990. **92**: p. 5057.
149. M. Tuckerman, et al., *Ab initio molecular dynamics simulation of the solvation and transport of hydronium and hydroxyl ions in water.* The Journal of Chemical Physics, 1995. **103**: p. 150.
150. A.K. Rappe and Goddard Iii, W.A., *Charge equilibration for molecular dynamics simulations.* The Journal of Physical Chemistry, 1991. **95**(8): p. 3358-3363.
151. D. Borgis and Hynes, J.T., *Molecular-dynamics simulation for a model nonadiabatic proton transfer reaction in solution.* The Journal of Chemical Physics, 1991. **94**: p. 3619.

152. M. Karplus and Petsko, G.A., *Molecular dynamics simulations in biology.* Nature, 1990. **347**(6294): p. 631-639.
153. M. Karplus and Mccammon, J.A., *Molecular dynamics simulations of biomolecules.* Nature Structural & Molecular Biology, 2002. **9**(9): p. 646-652.
154. M. Karplus and Kuriyan, J., *Molecular dynamics and protein function.* Proceedings of the National Academy of Sciences of the United States of America, 2005. **102**(19): p. 6679-6685.
155. J.A. Mccammon, Gelin, B.R., and Karplus, M., *Dynamics of folded proteins.* Nature, 1977. **267**(5612): p. 585-590.
156. A.D. Mackerell, et al., *All-Atom Empirical Potential for Molecular Modeling and Dynamics Studies of Proteins†.* The Journal of Physical Chemistry B, 1998. **102**(18): p. 3586-3616.
157. A.D. Mackerell, *Empirical force fields for biological macromolecules: Overview and issues.* Journal of Computational Chemistry, 2004. **25**(13): p. 1584-1604.
158. D.L. Beveridge and Dicapua, F.M., *Free Energy Via Molecular Simulation: Applications to Chemical and Biomolecular Systems.* Annual Review of Biophysics and Biophysical Chemistry, 1989. **18**(1): p. 431-492.
159. S.P. Scott, et al., *Challenges and Development of a Multi-Scale Computational Model for Photosystem I Decoupled Energy Conversion*, in *Applications of Molecular Modeling to Challenges in Clean Energy*. 2013, American Chemical Society. p. 177-202.
160. Y. Nakamura, et al., *Complete Genome Structure of the Thermophilic Cyanobacterium Thermosynechococcus elongatus BP-1*. DNA Research, 2002. **9**(4): p. 123-130.
161. D.O. Hall and Rao, K.K., *Photosynthesis*. 6 ed. 1999, New York: Cambridge University Press. 43.
162. G.W. Lynn, et al., *Bio-SANS—A dedicated facility for neutron structural biology at Oak Ridge National Laboratory.* Physica B: Condensed Matter, 2006. **385–386, Part 2**(0): p. 880-882.
163. P.A. Timmins, et al., *A physical characterization of some detergents of potential use for membrane protein crystallization.* FEBS Letters, 1988. **238**(2): p. 361-368.
164. P.V. Konarev, et al., *PRIMUS: a Windows PC-based system for small-angle scattering data analysis.* Journal of Applied Crystallography, 2003. **36**(5): p. 1277-1282.
165. S.P. Abel, et al., *Molecular Simulations of Dodecyl-β-maltoside Micelles in Water: Influence of the Headgroup Conformation and Force Field Parameters.* The Journal of Physical Chemistry B, 2010. **115**(3): p. 487-499.
166. M. Auer, Scarborough, G.A., and Kuhlbrandt, W., *Three-dimensional map of the plasma membrane H+-ATPase in the open conformation.* Nature, 1998. **392**(6678): p. 840-843.
167. Schrodinger, Llc, *The PyMOL Molecular Graphics System, Version 1.3r1*. 2010.
168. T. Vanaken, et al., *[3] Alkyl glycoside detergents: Synthesis and applications to the study of membrane proteins*, in *Methods in Enzymology*, B.F. Sidney Fleischer, Editor. 1986, Academic Press. p. 27-35.
169. L.-A. Barret, et al., *Influence of Hydrophobic Micelle Structure on Crystallization of the Photosynthetic RC-LH1-PufX Complex from Rhodobacter blasticus.* The Journal of Physical Chemistry B, 2013.
170. C. Dupuy, et al., *Anomeric Effects on the Structure of Micelles of Alkyl Maltosides in Water.* Langmuir, 1997. **13**(15): p. 3965-3967.

171. C. Tanford, *The hydrophobic effect: Formation of micelles and biological membranes*. Vol. 18. 1980. 687.
172. J. Lipfert, et al., *Size and Shape of Detergent Micelles Determined by Small-Angle X-ray Scattering.* The Journal of Physical Chemistry B, 2007. **111**(43): p. 12427-12438.
173. P. Strop and Brunger, A.T., *Refractive index-based determination of detergent concentration and its application to the study of membrane proteins.* Protein Science, 2005. **14**(8): p. 2207-2211.
174. X.G. Hong, Weng, Y.X., and Li, M., Biophysical Journal, 2004. **86**: p. 1082.
175. M.G. Santonicola, Lenhoff, A.M., and Kaler, E.W., Biophysical Journal, 2008. **94**: p. 3647.
176. R.M. Stroud and Agard, D.A., *Structure determination of asymmetric membrane profiles using an iterative Fourier method.* Biophysical Journal, 1979. **25**(3): p. 495-512.
177. M. Le Maire, Champeil, P., and Moller, J.V., Biochimica et Biophysica Acta, Biomembranes, 2000. **1508**: p. 86.
178. J.V. Moller and Lemaire, M., Journal of Biological Chemistry, 1993. **268**: p. 18659.
179. M. Roth, et al., *Detergent structure in crystals of a bacterial photosynthetic reaction centre.* Nature, 1989. **340**(6235): p. 659-662.
180. E. Pebaypeyroula, et al., Structure, 1995. **3**: p. 1051.
181. M. Ceccarelli and Marchi, M., Journal of Physical Chemistry B, 2003. **107**: p. 1423.
182. I. Lee, Lee, J.W., and Greenbaum, E., *Biomolecular electronics: Vectorial arrays of photosynthetic reaction centers.* Biophysical Journal, 1998. **74**(2): p. A16-A16.
183. M. Ciobanu, et al., *Electrochemistry and photoelectrochemistry of photosystem I adsorbed on hydroxyl-terminated monolayers.* Journal of Electroanalytical Chemistry, 2007. **599**(1): p. 72-78.
184. P.N. Ciesielski, Cliffel, D.E., and Jennings, G.K., *Kinetic Model of the Photocatalytic Effect of a Photosystem I Monolayer on a Planar Electrode Surface.* The Journal of Physical Chemistry A, 2011. **115**(15): p. 3326-3334.
185. N. Krauss, et al., *Three-dimensional structure of system I of photosynthesis at 6 Å resolution.* Nature, 1993. **361**(6410): p. 326-331.
186. J.J. Eaton-Rye, *The Construction of Gene Knockouts in the Cyanobacterium Synechocystis sp. PCC 6803* in *Photosynthesis Research Protocols*, R. Carpentier, Editor. 2004, Humana Press. p. 309-324.
187. X.N. Zang, et al., *Optimum conditions for transformation of Synechocystis sp PCC 6803.* Journal of Microbiology, 2007. **45**(3): p. 241-245.
188. I. Iwuchukwu, *Protein engineering for the Enhanced Photo-production of Hydrogen by Cyanobacterial Photosystem I*, in *Chemical and Biomolecular Engineering*. 2011, University of Tennessee: Knoxville.
189. T.M. Bricker, et al., *Isolation of a highly active Photosystem II preparation from Synechocystis 6803 using a histidine-tagged mutant of CP 47.* Biochimica et Biophysica Acta, Bioenergetics, 1998. **1409**(1): p. 50-57.
190. Y. Kashino, Koike, H., and Satoh, K., *An improved sodium dodecyl sulfate-polyacrylamide gel electrophoresis system for the analysis of membrane protein complexes.* Electrophoresis, 2001. **22**(6): p. 1004-1007.
191. H. Kubota, et al., *Purification and characterization of photosystem I complex from Synechocystis sp. PCC 6803 by expressing histidine-tagged subunits.* Biochimica et Biophysica Acta, Bioenergetics, 2010. **1797**(1): p. 98-105.

192. A.J. Bard and Faulkner, L.R., *Electrochemical Methods: Fundamentals and Applications*. 2000: Wiley.
193. R.K. Le, et al., *Analysis of the solution structure of Thermosynechococcus elongatus photosystem I in n-dodecyl-β-d-maltoside using small-angle neutron scattering and molecular dynamics simulation.* Archives of Biochemistry and Biophysics, 2014. **550–551**(0): p. 50-57.
194. X. Yan, et al., *Photosystem I in Langmuir–Blodgett and Langmuir–Schaefer Monolayers.* Langmuir, 2012. **28**(42): p. 15080-15086.
195. K. Gundlach, et al., *Filling the "green gap" of the major light-harvesting chlorophyll a/b complex by covalent attachment of Rhodamine Red.* Biochimica et Biophysica Acta (BBA) - Bioenergetics, 2009. **1787**(12): p. 1499-1504.
196. R.E. Blankenship, et al., *Comparing Photosynthetic and Photovoltaic Efficiencies and Recognizing the Potential for Improvement.* Science, 2011. **332**(6031): p. 805-809.
197. C.E. Lubner, et al., *Wiring photosystem I for electron transfer to a tethered redox dye.* Energy & Environmental Science, 2011. **4**(7): p. 2428-2434.

APPENDIX

APPENDIX I – HPLC Method for PSI Purification

```
        General Settings: Set Detectors Inline
        General Settings: Set Column Offline
        General Settings: UV Detector Wavelength = 280 nM and 430 nM
        General Settings: Flow Rate = 18.00 ml/min
        General Settings: Turn UV Detector Lamp On
        Pump On
0.00    min  Method Start
0.00    min  [01]  Equil Block
0.00    min        (A)  Purge with Equilibration Buffer
0.00    min             0.00 ml  Set Column Offline
0.00    min             0.00 ml  Set Solvent Blend  80.0% A:H2O 20.0% B:PSI buffer
0.00    min             0.00 ml  Set Flow Rate = 30.00 ml/min
0.00    min             0.00 ml  Reset Fraction Collector*
0.50    min             15.00 ml  Set Flow Rate = 18.00 ml/min
0.58    min             16.50 ml  Set Column 1 Inline
0.58    min
0.58    min        (B)  Eq column w/ Eq buffer
0.58    min             0.00 CV  Set Solvent Blend  80.0% A:H2O 20.0% B:PSI buffer
1.23    min             7.00 CV  Zero UV Detector*
1.23    min             7.00 CV  End Solvent Blend  80.0% A:H2O 20.0% B:PSI buffer
1.23    min
1.23    min  ----------------------------------------
1.23    min  [02]  Load Block
1.23    min        (A)  Step Segment
1.23    min             0.00 ml  Load through Pump  100% C
2.51    min             23.00 ml  Set Flow Rate = 10.00 ml/min*
2.51    min             23.00 ml  Load through Pump  100% C
2.51    min
2.51    min  ----------------------------------------
2.51    min  [03]  Wash Block
2.51    min        (A)  Wash sucrose out of column
2.51    min             0.00 CV  Set Solvent Blend  80.0% A:H2O 20.0% B:PSI buffer
3.17    min             4.00 CV  Set Flow Rate = 15.00 ml/min*
4.06    min             12.00 CV  End Solvent Blend  80.0% A:H2O 20.0% B:PSI buffer
4.06    min
```

```
 4.06   min  [04]  Elute Block
 4.06   min        (A)  Gradient segment
 4.06   min             0.00 CV  Start Gradient  80.0% A:H2O 20.0% B:PSI buffer
 4.72   min             6.00 CV  Start Fraction Collection Peak 1.00ml Thr 0.500 Slp  0.200*
 5.17   min             10.00 CV  End Gradient  70.0% A:H2O 20.0% B:PSI buffer 10.0% D:MgSO4
 5.17   min
 5.17   min        (B)  Step Segment
 5.17   min             0.00 CV  Set Solvent Blend  70.0% A:H2O 20.0% B:PSI buffer 10.0% D:MgSO4
 6.27   min             10.00 CV  End Solvent Blend  70.0% A:H2O 20.0% B:PSI buffer 10.0% D:MgSO4
 6.27   min
 6.27   min        (C)  Elution gradient
 6.27   min             0.00 CV  Start Gradient  70.0% A:H2O 20.0% B:PSI buffer 10.0% D:MgSO4
 7.60   min             12.00 CV  End Gradient  50.0% A:H2O 20.0% B:PSI buffer 30.0% D:MgSO4
 7.60   min
 7.60   min        (D)  Step Segment
 7.60   min             0.00 CV  Set Solvent Blend  20.0% A:H2O 20.0% B:PSI buffer 60.0% D:MgSO4
 8.16   min             5.00 CV  End Solvent Blend  20.0% A:H2O 20.0% B:PSI buffer 60.0% D:MgSO4
 8.16   min
 8.16   min  ----------------------------------------
 8.16   min  [05]  Clean Block
 8.16   min        (A)  Rinse Column with H2O
 8.16   min             0.00 CV  Set Solvent Blend  100% A:H2O
 8.49   min             3.00 CV  Stop Fraction Collection*
 8.50   min             3.10 CV  Reset Fraction Collector*
 8.71   min             5.00 CV  End Solvent Blend  100% A:H2O
 8.71   min
 8.71   min        (B)  Acid wash column
 8.71   min             0.00 CV  Set Solvent Blend  90.0% A:H2O 10.0% E:HCl
 9.27   min             5.00 CV  End Solvent Blend  90.0% A:H2O 10.0% E:HCl
 9.27   min
 9.27   min        (C)  Rinse out acid with H2O
 9.27   min             0.00 CV  Set Solvent Blend  100% A:H2O
10.04   min             7.00 CV  End Solvent Blend  100% A:H2O
10.04   min
10.04   min        (D)  Restore column pH
```

```
8.16    min     (A)  Rinse Column with H2O
8.16    min          0.00 CV  Set Solvent Blend  100% A:H2O
8.49    min          3.00 CV  Stop Fraction Collection*
8.50    min          3.10 CV  Reset Fraction Collector*
8.71    min          5.00 CV  End Solvent Blend  100% A:H2O
8.71    min
8.71    min     (B)  Acid wash column
8.71    min          0.00 CV  Set Solvent Blend  90.0% A:H2O 10.0% E:HCl
9.27    min          5.00 CV  End Solvent Blend  90.0% A:H2O 10.0% E:HCl
9.27    min
9.27    min     (C)  Rinse out acid with H2O
9.27    min          0.00 CV  Set Solvent Blend  100% A:H2O
10.04   min          7.00 CV  End Solvent Blend  100% A:H2O
10.04   min
10.04   min     (D)  Restore column pH
10.04   min          0.00 CV  Set Solvent Blend  60.0% A:H2O 40.0% B:PSI buffer
11.70   min          15.00 CV  End Solvent Blend  60.0% A:H2O 40.0% B:PSI buffer
11.70   min      Thresholds [  pH >  5.5, Delay 0.00 CV]
11.70   min  ----------
```

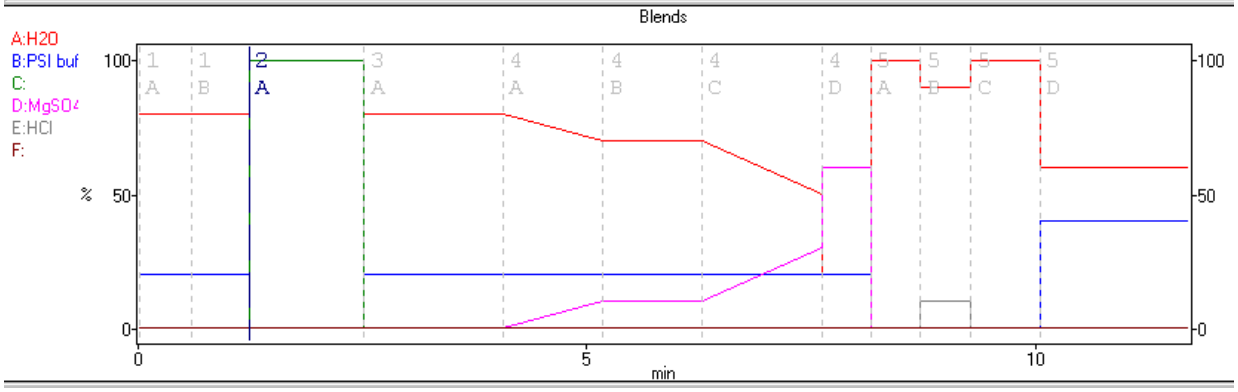

APPENDIX II – Raw Data for Hydrogen Evolution Screening Experiments

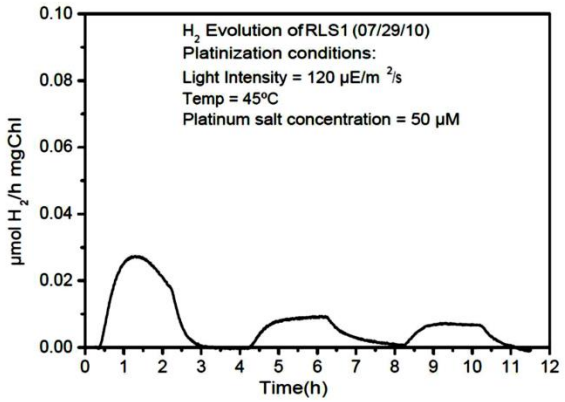

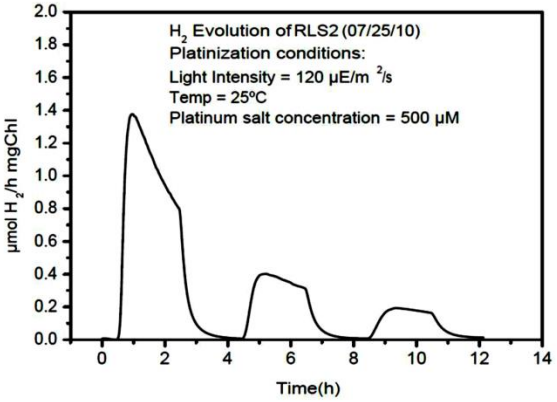

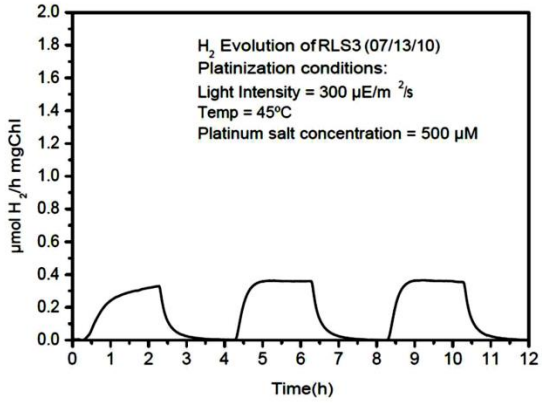

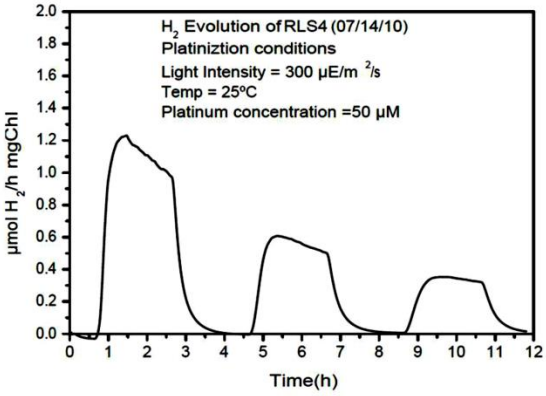

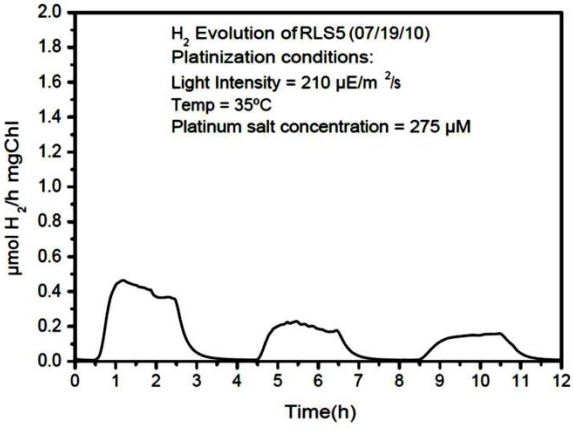

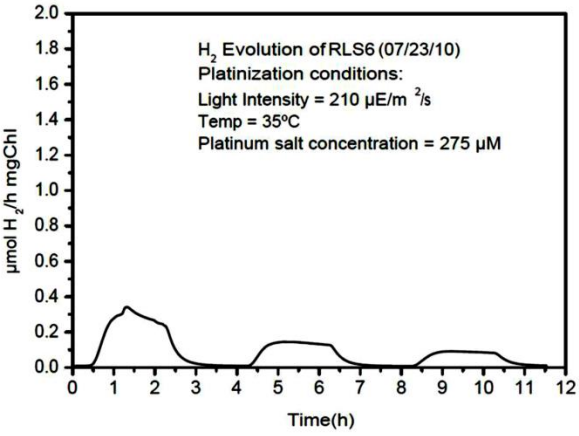

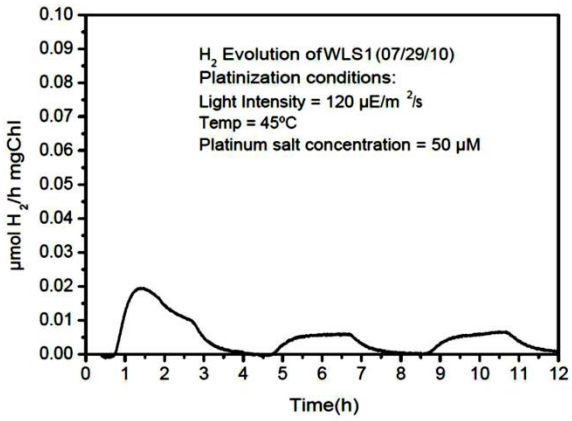
H2 Evolution of WLS1 (07/29/10)
Platinization conditions:
Light Intensity = 120 µE/m 2/s
Temp = 45ºC
Platinum salt concentration = 50 µM
µmol H2/h mgChl
Time(h)

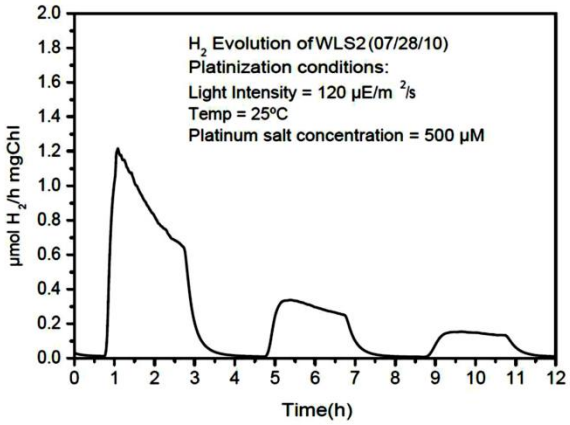
H2 Evolution of WLS2 (07/28/10)
Platinization conditions:
Light Intensity = 120 µE/m 2/s
Temp = 25ºC
Platinum salt concentration = 500 µM
µmol H2/h mgChl
Time(h)

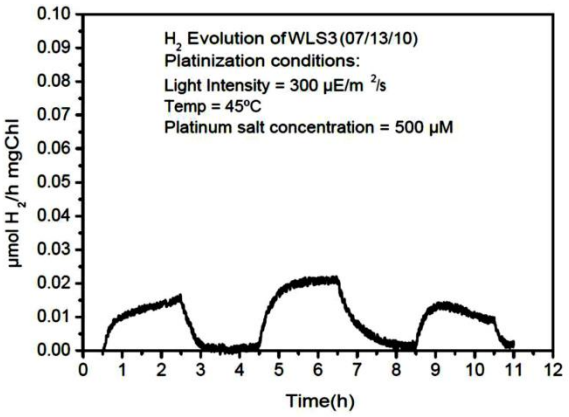
H2 Evolution of WLS3 (07/13/10)
Platinization conditions:
Light Intensity = 300 µE/m 2/s
Temp = 45ºC
Platinum salt concentration = 500 µM
µmol H2/h mgChl
Time(h)

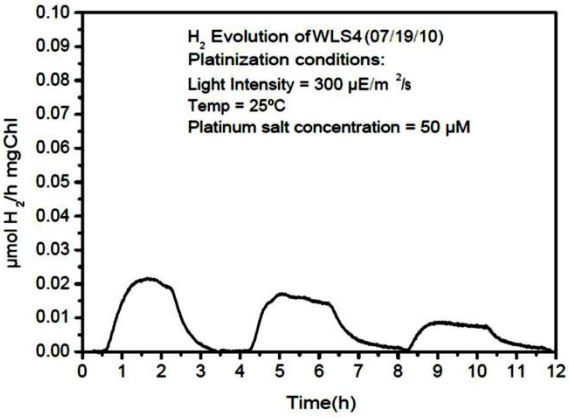
H2 Evolution of WLS4 (07/19/10)
Platinization conditions:
Light Intensity = 300 µE/m 2/s
Temp = 25ºC
Platinum salt concentration = 50 µM
µmol H2/h mgChl
Time(h)

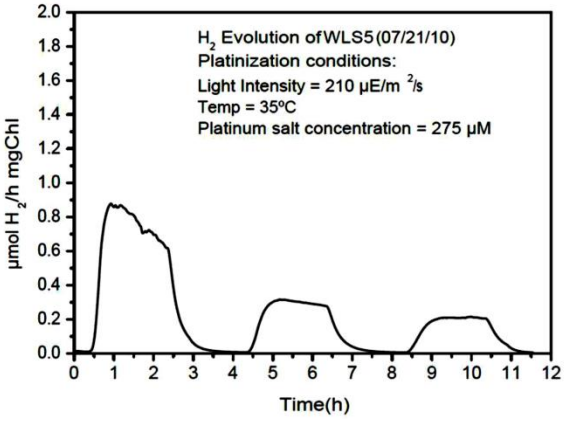
H2 Evolution of WLS5 (07/21/10)
Platinization conditions:
Light Intensity = 210 µE/m 2/s
Temp = 35ºC
Platinum salt concentration = 275 µM
µmol H2/h mgChl
Time(h)

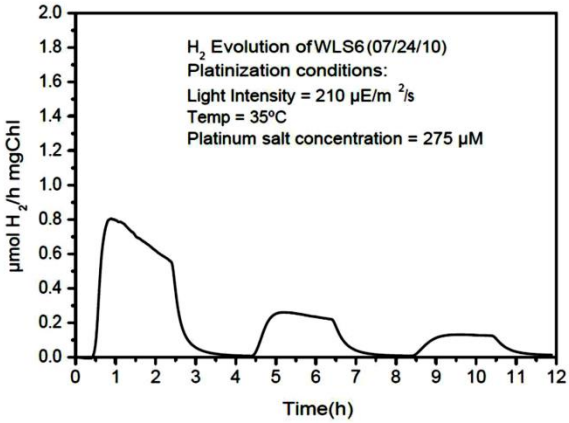
H2 Evolution of WLS6 (07/24/10)
Platinization conditions:
Light Intensity = 210 µE/m 2/s
Temp = 35ºC
Platinum salt concentration = 275 µM
µmol H2/h mgChl
Time(h)

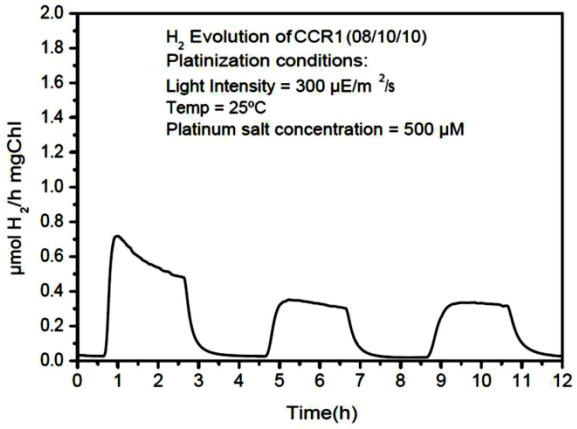
H2 Evolution of CCR1 (08/10/10)
Platinization conditions:
Light Intensity = 300 µE/m 2/s
Temp = 25ºC
Platinum salt concentration = 500 µM
µmol H2/h mgChl
Time(h)

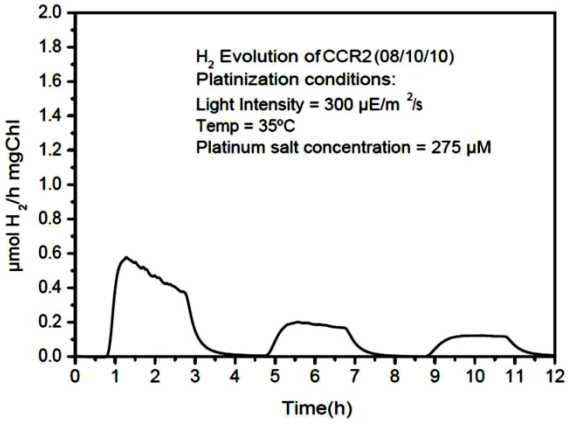
H2 Evolution of CCR2 (08/10/10)
Platinization conditions:
Light Intensity = 300 µE/m 2/s
Temp = 35ºC
Platinum salt concentration = 275 µM
µmol H2/h mgChl
Time(h)

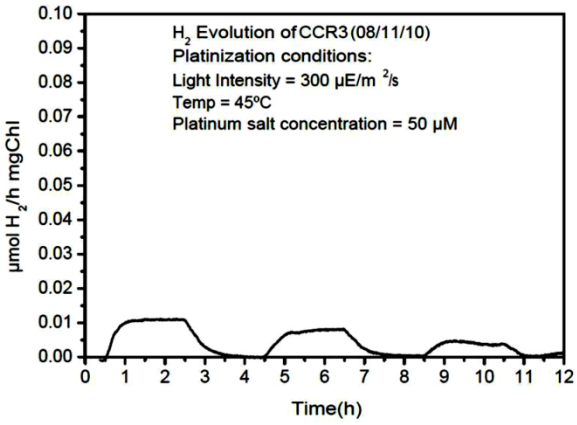
H2 Evolution of CCR3 (08/11/10)
Platinization conditions:
Light Intensity = 300 µE/m 2/s
Temp = 45ºC
Platinum salt concentration = 50 µM
µmol H2/h mgChl
Time(h)

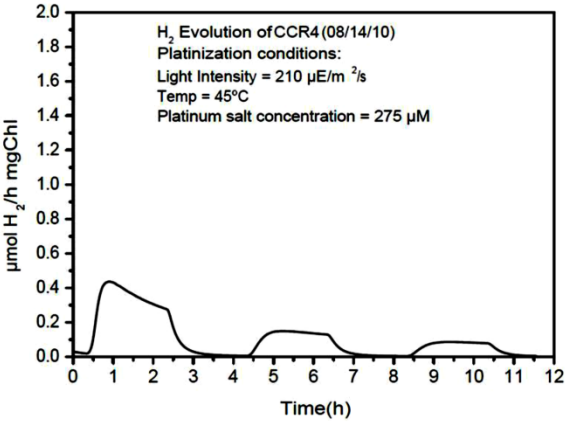
H2 Evolution of CCR4 (08/14/10)
Platinization conditions:
Light Intensity = 210 µE/m 2/s
Temp = 45ºC
Platinum salt concentration = 275 µM
µmol H2/h mgChl
Time(h)

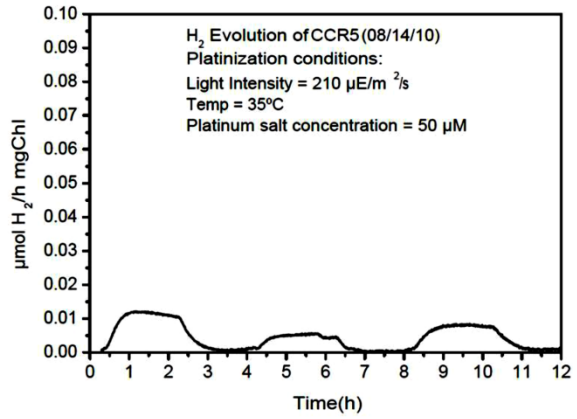
H2 Evolution of CCR5 (08/14/10)
Platinization conditions:
Light Intensity = 210 µE/m 2/s
Temp = 35ºC
Platinum salt concentration = 50 µM
µmol H2/h mgChl
Time(h)

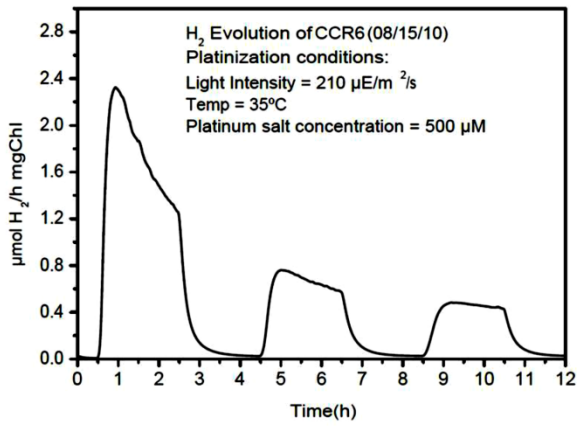
H2 Evolution of CCR6 (08/15/10)
Platinization conditions:
Light Intensity = 210 µE/m 2/s
Temp = 35ºC
Platinum salt concentration = 500 µM
µmol H2/h mgChl
Time(h)

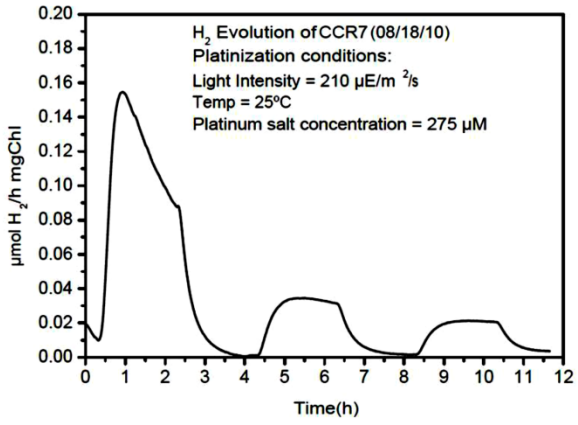
H2 Evolution of CCR7 (08/18/10)
Platinization conditions:
Light Intensity = 210 µE/m 2/s
Temp = 25ºC
Platinum salt concentration = 275 µM
µmol H2/h mgChl
Time(h)

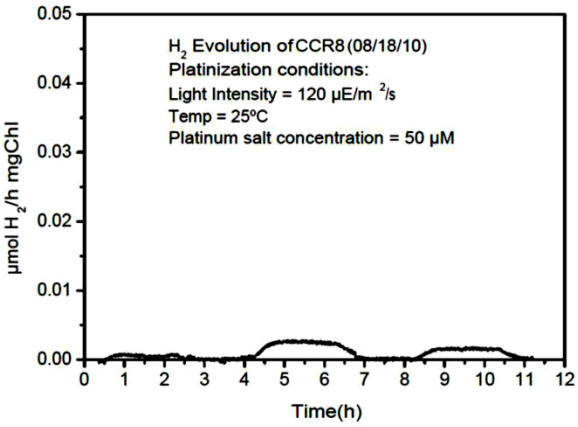
H2 Evolution of CCR8 (08/18/10)
Platinization conditions:
Light Intensity = 120 µE/m 2/s
Temp = 25ºC
Platinum salt concentration = 50 µM
µmol H2/h mgChl
Time(h)

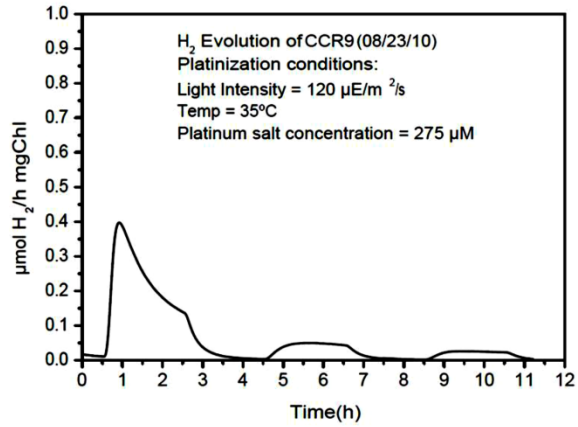
H2 Evolution of CCR9 (08/23/10)
Platinization conditions:
Light Intensity = 120 µE/m 2/s
Temp = 35ºC
Platinum salt concentration = 275 µM
µmol H2/h mgChl
Time(h)

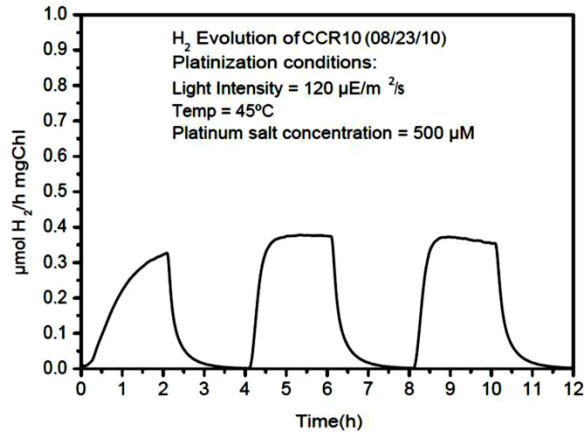
H2 Evolution of CCR10 (08/23/10)
Platinization conditions:
Light Intensity = 120 µE/m 2/s
Temp = 45ºC
Platinum salt concentration = 500 µM
µmol H2/h mgChl
Time(h)

APPENDIX III – Primer Sequences for LPETG-PSI *Synechocystis* 6803 Mutants

Sequence description	GC Content (%)	Melting Temp. (°C)*	5' → 3' sequence
PsaA upstream forward, AatII	66.7	62.9	AAGACGTCATGGGGAACTTGGAACTCGGCCCC
PsaA upstream reverse, LPETGGH$_6$, SphI	61.5	66.7	AAGCATGCCTAGTGGTGGTGGTGGTGGTGGCCGCCCG TCTCAGGAAGGCCAATGGAAAGACTGCGGGCGAGGA
PsaA downstream forward, SpeI	66.7	63.8	TTCTGCAGATGCCAGGGGGACTGGCTGAGGTT
PsaA downstream reverse, SalI	66.7	64.3	AAGTCGACCTATGGCCAGCAGTGTCGGGATCC
PsaB upstream forward, SacII	61.9	60.5	AACCATGGATGCGGCACCTGCCAAGTATCTGG
PsaB upstream reverse, LPETGGH$_6$, SacII	57.1	60.9	AACCGCGGCTAGTGGTGGTGGTGGTGGTGGCCCGTCT CAGGAAGACCGAACTTACCGGCTGTGGA
PsaB downstream forward, SpeI	57.1	59.4	TTCTGCAGATGTTAAGCTTGTCCCCTGCCCTC
PsaB downstream reverse, SalI	61.9	60.4	AAGTCGACCTAGGAAACCGATGGGGTGGAAGG
PsaD upstream forward, SphI	61.9	60.7	AAGCATGCATGCGCTCCGCCATCTCGTTGAAG
PsaD upstream reverse, LPETGGH$_6$, SphI	61.9	59.3	AACCATGGCTAGTGGTGGTGGTGGTGGTGGCCCGTCT CAGGAAGGACCTCGTAGGGGGCTTTACC
PsaD downstream forward, SpeI	57.1	59.6	AACTGCAGATGCTGGCTCTACTTGCTTGCGGA
PsaD downstream reverse, SalI	61.9	59.2	AAGTCGACCTACAGCCTGAGGGAACGGTAGAG
PsaE upstream forward, ApaI	56.7	55.6	AAAGGGCCCCAGTTCATCGATGGTGAAGGG
PsaE upstream reverse, LPETGGH$_6$, AatII	58.8	63.8	AAGACGTCCTAGTGGTGGTGGTGGTGGTGGCCCGTCT CAGGAAGTTTTGCCGCCGCTTGCACCAATTC
PsaE downstream forward, SacI	48.5	58.1	AAAGAGCTCCAGAAGTTGAAACAGTATGCCGGG
PsaE downstream reverse, NsiI	43.3	58.3	AAAATGCATAAACTAGTGCCTCCAGCCTCA
PsaI upstream forward, SphI	61.9	62.4	CTGCATGCATGGCCCCTAGCAACCGAAGGCTT
PsaI upstream reverse, LPETGGH$_6$, SacII	50.0	59.2	AACCGCGGCTAGTGGTGGTGGTGGTGGTGGCCGCCCG TCTCAGGAAGACCTTCGCCTTCACTCTCAATGTG
PsaI upstream forward, SphI	61.9	62.4	CTGCATGCATGGCCCCTAGCAACCGAAGGCTT
PsaI upstream reverse, LPETGGH$_6$, SacII	50.0	59.2	AACCGCGGCTAGTGGTGGTGGTGGTGGTGGCCGCCCG TCTCAGGAAGACCTTCGCCTTCACTCTCAATGTG
PsaI downstream forward, SpeI	66.7	61.9	AACTGCAGATGGGGTGGGTCAGGATTCCTCCG
PsaI downstream reverse, SalI	61.9	61.3	TTGTCGACCTAAATGGAGGGGGTCTGGGTGAC

Sequence description	GC Content (%)	Melting Temp. (°C)*	5’ → 3’ sequence
PsaL upstream forward, SphI	52.4	56.1	AAGCATGCATGGCCAGGCTCGACAATATTGAC
PsaL upstream reverse, LPETGGH6, SacII	44.4	57.5	AACCGCGGCTAGTGGTGGTGGTGGTGGTGGCCGCCCG TCTCAGGAAGGTTAAATAGACCCCGGAAAATCCCATC
PsaL downstream forward, SpeI	71.4	65.5	GGCTGCAGATGCCGTTGCCACGACGGCCTGAG
PsaL downstream reverse, SalI	66.7	65.3	TTGTCGACCTAAATTGCTCCCGCACGGGGGTG
PsaM upstream forward, SphI	57.1	59.4	TTGCATGCATGCCCTCTGGTTGGGAACCACTT
PsaM upstream reverse, LPETGGH$_6$, SacII	46.2	57.7	AACCGCGGCTAGTGGTGGTGGTGGTGGTGGCCGCCCG TCTCAGGAAGCTTATAAAGTTCCGTGGAGAGACGGA
PsaM downstream forward, SpeI	57.1	60.0	CCCTGCAGATGACCAACGTCGGCCGTGTAATC
PsaM downstream reverse, SalI	57.1	60.9	TTGTCGACCTATTGTGGCGGCTTTTCCCTGTG

*The melting temperature applies to the target sequence gene and excludes modifying bases such as restriction sites or the LPETGGH6 sequence.

VITA

Rosemary Khuu Le was born in Binghamton, New York on December 22, 1986 to Ly and Ut Le. She graduated from William G. Enloe High School in 2005 and entered North Carolina State University. She received a Bachelor of Science degree in Chemical and Biomolecular Engineering with a minor in Biotechnology in May 2009. In August 2009 she joined the University of Tennessee as an NSF IGERT fellow in the Sustainable Technology through Advanced Interdisciplinary Research (STAIR) Program to pursue her PhD in Chemical and Biomolecular Engineering.